Three-Dimensional Imaging of Single Atoms in an Optical Lattice via Helical Point-Spread-Function Engineering

Tangi Legrand

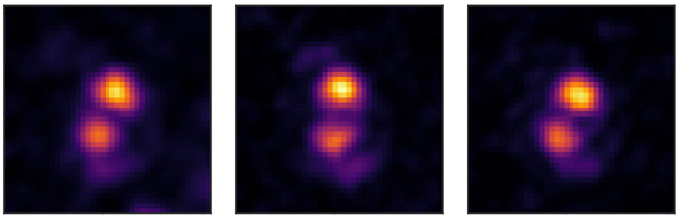

Masterarbeit in Physik
angefertigt im Institut für Angewandte Physik

vorgelegt der
Mathematisch-Naturwissenschaftlichen Fakultät
der
Rheinischen Friedrich-Wilhelms-Universität
Bonn

Dezember 2022

I hereby declare that this thesis was formulated by myself and that no sources or tools other than those cited were used.

Bonn, ...
Date Signature

1. Gutachter: Prof. Dr. Dieter Meschede
2. Gutachter: Prof. Dr. Sebastian Hofferberth

Contents

“Accurate and minute measurement seems to the non-scientific imagination, a less lofty and dignified work than looking for something new. But nearly all the grandest discoveries of science have been but the rewards of accurate measurement and patient long-continued labour in the minute sifting of numerical results.”

William Thomson, Baron Kelvin[1]

CHAPTER 1

Introduction

Breakthroughs such as the discovery of the laser, laser cooling, particle trapping, and the development of methods for manipulating and detecting the state of single quanta enable impressive control of complex quantum systems. Applications are prominent in quantum communication and cryptography [2–4], quantum metrology and sensing [5–8], as well as quantum information and simulation [9–13]. One promising architecture for the latter are ultracold neutral atoms trapped in optical lattices [13, 14].

Our group has built a two-dimensional discrete quantum simulator (DQSIM) where an ensemble of caesium atoms are trapped and cooled at discrete positions of a three-dimensional optical lattice [15]. Two long-lived hyperfine ground states form an effective qubit. The particularity of our experiment is the usage of two independent lattices of orthogonal polarization, each coupling to one of the qubit states [16]. A relative shift of the two lattices allows two-dimensional state-dependent transport, such that quantum mechanical interference effects of multiple indistinguishable atoms can be studied or exploited for other measurements. For instance, the atoms prepared in the apparatus were used as sensitive samples for magnetic fields and differential light shifts [17]. With Ramsey imaging, the *in situ* reconstruction of optical potentials is achieved [18]. The direct measurement of the Wigner function of the cold atoms was proposed [19], as well as simulations of topological insulators [20, 21], direct measurements of the exchange phase in a two atom interferometer [22], and boson sampling with cold atoms [23].

Imaging is at the heart of most experiments with cold atoms, including ours, because it provides access to desired observables [14, 24–27]. Established methods include absorption imaging [28–35], fluorescence imaging [18, 36–49], and dispersive coupling to a cavity [50–58]. Our DQSIM machine uses fluorescence microscopy with a state-of-the-art objective of high numerical aperture NA = 0.92 providing an optical resolution at the level of an Abbe radius of 463 nm. Being smaller than the horizontal lattice constant of 612 nm, this enables single-site resolved imaging and addressing of individual atoms in the lattice [59], making it a so-called quantum gas microscope [24].

Usually, imaging involves integration along the observation axis resulting in information loss. While this is irrelevant for experiments in one- or two-dimensional geometries, in the three-dimensional case special techniques are needed to circumvent the loss of information and to resolve the position of atoms in all three dimensions. One possible approach is tomography, in which multiple images are acquired with the microscope set at different focal planes each time [46, 60, 61]. However, the need for multiple images represents an experimental restriction which is undesirable, for example due to finite coherence times. Although not suitable for imaging optical lattices, an approach involves letting three-dimensional

---

[1] In an address to the British Association for the Advancement of Science in his role as its president [1], p. 91.

ensembles of atoms fall through a thin light sheet while capturing images in a pulsed fashion [62]. Another imaging method resolving three dimensions, but so far realized only for noble gases relies on metastable atoms, falling onto a microchannel plate detector once the trapping potential is switched off. The atoms are spatially resolved by detecting the free electrons generated at the detector surface by the quenching of the internal state and concomitant release of energy. The measured arrival times provide information about the vertical position [63, 64]. Ion microscopes for cold atoms work on the same principle, except that the atoms are ionized before being accelerated onto the detector [65–67]. This method exceeds the diffraction-limited resolution limit of optical systems and exhibits a much higher depth of field (DOF). However, the axial resolution is still in the range of 1 µm [67] and the micro-channel plates have a limited detection efficiency in the range of 40 to 86 % [24, 68]. This is significantly less than well over 99 % achievable with fluorescence imaging due to the large number of photons detected [24]. Light field microscopy using microlens arrays has also been used [69], but has a limited spatial resolution. The recently realized method to image cold atoms entirely without a microscope objective, but using a multimode fiber, also enables the capture of all three dimensions, as the measured field can be reconstructed for several planes from a single measurement [70].

In this thesis, I present a novel technique enabling three-dimensional localization of single atoms in an optical lattice up to sub-micrometer precision over an enhanced DOF from a single experimental image. It consists of changing the microscope's response to a point source, the so-called point spread function (PSF), such that it has an azimuthally structured shape, performing a rigid rotation along the observation axis, the angle of which provides information about the axial position. This is done by imposing on the collected fluorescence light a phase modulation built up from a superposition of Laguerre-Gauss (LG) modes in the pupil plane by a spatial light modulator (SLM). I demonstrate this method using the DQSIM quantum gas microscope with an engineered double-helix-shaped PSF. As I show, this enables axial resolution at the level of the vertical lattice separation of 532 nm even at lower numerical apertures while preserving the lateral resolution, overcoming the limitations of retrieving the axial position through the defocus alone.

Axially rotating intensity distributions were first described in 1996 [71] and were later proposed for depth estimation [72]. Thereafter, such PSFs have been employed for three-dimensional localization of single molecules beyond the diffraction limit in the field of microscopy of biological structures [73–75]. It has since become an active field of research with a variety of advancements [76–83].

In the DQSIM apparatus the information about the axial position of the atoms is important, for instance, when measuring multi-particle interference using state-dependent transport. In fact, it must be insured that all atoms lie in the same vertical plane. The novel three-dimensional quantum gas microscope allows one to identify and thus post-select atoms in a desired plane. This complements the spectroscopic method of preparing single planes from a lattice of which many planes were originally filled, as presented in Reference [84]. Three-dimensional imaging however also entails the ability to bring quantum simulations into three-dimensional geometries.

Following this introduction in Chapter 1, I present the experimental setup of the DQSIM experiment in Chapter 2. I particularly address the aspects necessary for the understanding of the subsequent measurements, as well as my contributions to the setup. Chapter 3 is about my contributions to a deep horizontal lattice. In Chapter 4, I present the three-dimensional imaging of single atoms. I describe the technique of preparing atoms in a single plane, the concept of PSF, and the resolution limit. I then discuss existing methods of three-dimensional imaging, in particular the rotating PSFs. Finally, I present the experimental realization and the measurements performed. Chapter 5 draws a conclusion and gives an outlook to this thesis.

CHAPTER 2

Experimental apparatus and techniques

Several unique properties make neutral atoms in optical lattices a promising platform for quantum simulations [10–13]. Laser cooling techniques and optical pumping allow to establish a well-defined initial state. Hyperfine states, for instance, can be conveniently coupled by microwave radiation, or by Raman transitions. The final states of individual atoms pinned in an optical lattice are made accessible by recording their fluorescence. High-resolution imaging systems make it possible to detect many atoms in close proximity at once. Yet, the atoms do not interact unless they are made to do so.

Building on a conceptually analogous experiment in one dimension [16, 85, 86], the two-dimensional discrete quantum simulator (DQSIM) was developed to combine the powerful tool of state-dependent transport with the extended possibilities of richer geometry. For example, the exchange phase of two indistinguishable atoms may be measured without the atoms ever having to come close to each other, ensuring that the contribution of the exchange to their interaction energy is negligible [22]. Control over the internal state and the position of atoms in two dimensions will also enable the study of topology and artificial gauge fields with two-dimensional discrete quantum walks [20, 21] and the direct measurement of the Wigner function [19]. The additional dimension allows a significant scaling of the atoms available for experimentation.

The expansion to two dimensions brings new challenges that led to the development of improved experimental components, such as a NA = 0.92 objective for high-resolution single-site detection [59] and a vacuum glass cell with ultra-low birefringence to reduce decoherence [87]. Many details of the experimental apparatus have been presented in the related dissertations, namely references [15, 17, 84].

In this chapter, I will briefly summarize the main experimental components and experimental techniques used. I begin by presenting a typical experimental sequence in Section 2.1. The imaging system and the optical lattice are described in more detail in Sections 2.2 and 2.3, respectively.

2.1 Overview and typical experimental sequence

The DQSIM experiments are stochastic in nature and are performed in repeated runs of an experimental sequence consisting of state preparation, manipulation of states, and subsequent detection. In this section, I provide an overview of the experimental setup and a typical experimental sequence.

Shielding atoms from their environment. Experimentation with cold atoms requires good isolation from the environment so that they can be well controlled. For this purpose, only a thin background gas

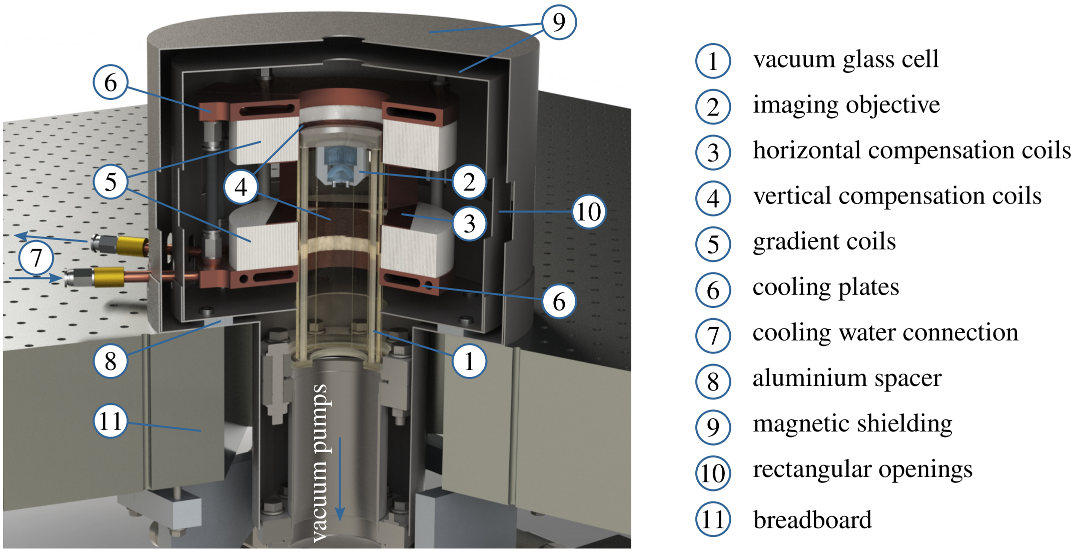

Figure 2.1: Cutaway drawing of the experimental setup's central part. Taken and modified from Reference [15].

of atoms is prepared in a vacuum system. Figure 2.1 shows a cutaway drawing of the main part of the experimental setup, namely the vacuum cell with the objective enclosed therein, surrounded by several magnetic coils within a magnetic shielding. In this thesis, vertical always refers to the direction towards the lens, whereas horizontal refers to the dimensions orthogonal to it.

The vacuum cell consists of a uniform prism with dodecagon base allowing a high degree of optical access. As (e.g. stress-induced) birefringence leads to distortions in the polarization of laser beams passing through the glass cell causing uncontrolled vectorial light shifts, special effort was put in reducing it as much as possible [87].

Pre-cooling and trapping in a MOT. The ^{137}Cs atoms in the background gas initially at room temperature must be trapped and cooled in order to gain control over their internal electronic and external vibrational states. A magneto-optical trap (MOT), first demonstrated in 1985 [88], is used as a first step. It consists of simultaneous cooling and trapping along all three directions by a combination of an optical molasses and a magnetic quadrupole field. The optical molasses is a pair of counter-propagation beams for each direction which is red-detuned to the cooling transition, which is chosen to be the $|F = 4\rangle \longrightarrow |F' = 5\rangle$ transition of the caesium D2 line. The level scheme is shown in Figure 2.2 a). The scattering rate of photons is highest on resonance and decreases for larger detunings. For atoms moving towards a red-detuned laser, the light will be Doppler shifted closer to resonance, leading to a higher scattering rate. As the momenta of the spontaneously re-emitted photons average to zero, this results in a radiation pressure in the direction of the beam. The six beams from all directions lead to a viscous force effectively cooling the atoms. For an effective two-level system, the achievable temperature limit is limited by the randomness of spontaneous emission to the Doppler temperature $T_\mathrm{D} = \hbar\Gamma/2k_\mathrm{B}$ [89], which amounts to $125\,\mu\mathrm{K}$ for the linewidth of the caesium D2 transition $\Gamma = 2\pi \times 5.2\,\mathrm{MHz}$. However, when accounting the degeneracy of the atomic states lifted by the AC Stark effect, is can be found that even lower temperatures up to the recoil temperature can be reached [90].

Off-resonant scattering events lead to atoms decaying into the $|F = 3\rangle$ dark state. To close the cooling

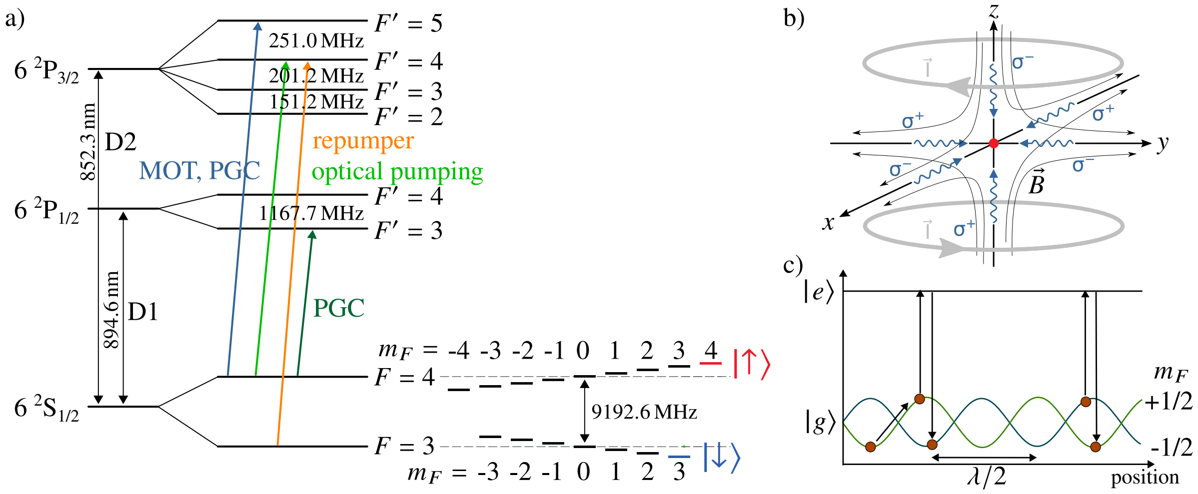

Figure 2.2: a) The caesium level scheme showing the transitions for cooling and optical pumping. The Zeeman sub-levels of the ground state are shown with lifted degeneracy from a magnetic field. The energy spacings are not to scale. b) MOT configuration showing the anti-Helmholtz coils, the magnetic field lines and the $\sigma^{\pm}$-polarized (red-detuned) beams. Taken and modified from Reference [15]. c) Sisyphus cooling principle on a transition between a $J = \frac{1}{2}$ ground state $|g\rangle$ and a $J = \frac{3}{2}$ excited state $|e\rangle$.

cycle, a repumper beam tuned to the $|F = 3\rangle \longrightarrow |F' = 4\rangle$ transition is therefore overlapped on the MOT beams.

A position dependent force is needed to confine the atoms in a small region and prevent diffusion. A MOT in a $J' = J + 1$ configuration realizes this by an orthogonal circular polarization of each pair of MOT beams and a quadrupole magnetic field. Figure 2.2 b) shows the configuration schematically. The spatial linear inhomogeneity of the magnetic field creates a proportional differential Zeeman shift whose sign is depending on the sign of the difference of angular momentum quantum number ΔM_J. This leads to atoms being more likely to scatter with the red detuned beam of σ^+ or σ^- polarization, depending on their relative side of the magnetic field center, thus resulting in a restoring force acting towards the center.

The MOT is created about 1 mm below the surface of the objective lens and subsequently transported to the objective's working distance of 150 µm by changing the center of the quadrupole field using compensation coils (cf. Figure 2.1).

Further cooling in the optical lattice. The atoms are transferred into the three-dimensional optical lattice by turning on the lattice beams and turning off the MOT. Light-assisted collisions between pairs of atoms lead to single-atom occupancy [91]. Being confined within single lattice sites, their motional state is given by the respective lattice site's vibrational level.

Polarization gradient cooling (PGC), or Sisyphus cooling, is employed for further sub-Doppler cooling and imaging [90]. Horizontally, we use PGC on the D2 line (together with a repumper), while vertically the D1 line is used in order to be able to collect the D2 fluorescence light for imaging while blocking the D1 light by filters in front of the camera. We use beam pairs overlapped with the lattice beams which have orthogonal linear polarization (lin⊥lin configuration) in each direction resulting in the polarization varying between linear and circular every half wavelength. This causes spatially periodic light shifts in Zeeman sublevels of the ground state. A schematic is shown in Figure 2.2 c). Atoms moving through the potential landscape will be optically pumped into the Zeeman sublevel with lowest energy. As the optical pumping takes some time, atoms will more likely be further ‘uphill’ when being optically pumped, thus repeated pumping cycles dissipate the kinetic energy previously converted into potential energy. Intensity and detuning of the PGC beams are optimized for optimal cooling by maximizing the atom’s survival between consecutive images. For imaging, the PGC beams are optimized to yield a higher scattering rate in order to collect more fluorescence photons.

State preparation. Sideband cooling techniques mediated by microwave photons for the horizontal direction and by Raman transitions for the vertical can be employed to prepare about 95 % [17] or 90 % [84] of the atoms in the motional ground state along the different directions, respectively. This enables the indistinguishability of the atoms required to probe quantum statistics and enhances coherence times. However, these techniques were not used for the purposes of this thesis.

To prepare atoms in a certain internal state, a σ^+ polarized beam resonant to the $|F = 4\rangle \longrightarrow |F' = 4\rangle$ transition is used to optical pump the atoms into the outermost m_F level of the ground state $|\uparrow\rangle := |F = 4, m_F = 4\rangle$, cf. Figure 2.2 a). The degeneracy is lifted by a magnetic field defining the quantization axis.

Coherent manipulation. Resonant microwaves couple $|\uparrow\rangle$ to the $|\downarrow\rangle := |F = 3, m_F = 3\rangle$ at $\approx 9.2\,\mathrm{GHz}$. Together, $|\uparrow\rangle$ and $|\downarrow\rangle$ form an effective two-level system, or qubit, on which coherent manipulations can be performed. For example, a $\pi/2$-pulse can create a coherent superposition $(|\uparrow\rangle + |\downarrow\rangle)/\sqrt{2}$. It was proposed to utilize a spatial light modulator (SLM) to shine a site-resolved Raman beam through the objective, adding to the global operations by microwaves the possibility to perform site-resolved operations [20], thereby considerably extending the experimental toolbox.

The state-dependent lattice allows to perform position or momentum shift operations on each qubit state separately. During the coherent manipulations, the intensity of the optical lattice potential is adiabatically lowered to reduce the off-resonant scattering rate of lattice photons and thus maintain long coherence times. The physical observables under investigation are mapped onto the qubit.

State detection. A projection on the qubit basis state $|\downarrow\rangle$ is performed by illuminating the atoms with cooling beams tuned to resonance, heating out all atoms in $|F = 4\rangle$. Subsequently, atoms remaining in the $|F = 3\rangle$ state, or specifically $|\downarrow\rangle$, can be detected by fluorescence imaging.

2.1.1 Laser system

The light for the horizontal PGC and the MOT is provided by a titanium-sapphire laser[1] and both the repumper and the vertical cooling light each come from interference-filter-stabilized external cavity diode lasers[2]. The lasers are actively frequency-stabilized using polarization spectroscopy setups. Acusto-optic modulators (AOMs) in double-pass configurations allow for modulation of frequency and intensity, the setting of which must be optimized for optimal cooling. I performed the realignment of all cooling and imaging beams and the readjustment of cooling parameters. For the latter, I iteratively scanned (coupled) intensities and frequencies of each beam and optimized survival between two fluorescence images in a small central region.

---

[1] Matisse CR from Sirah Lasertechnik, pumped by a Millennia 20eV from Spectra Physics.

[2] Build in our group based on a design reported by [92] and characterized by [93].

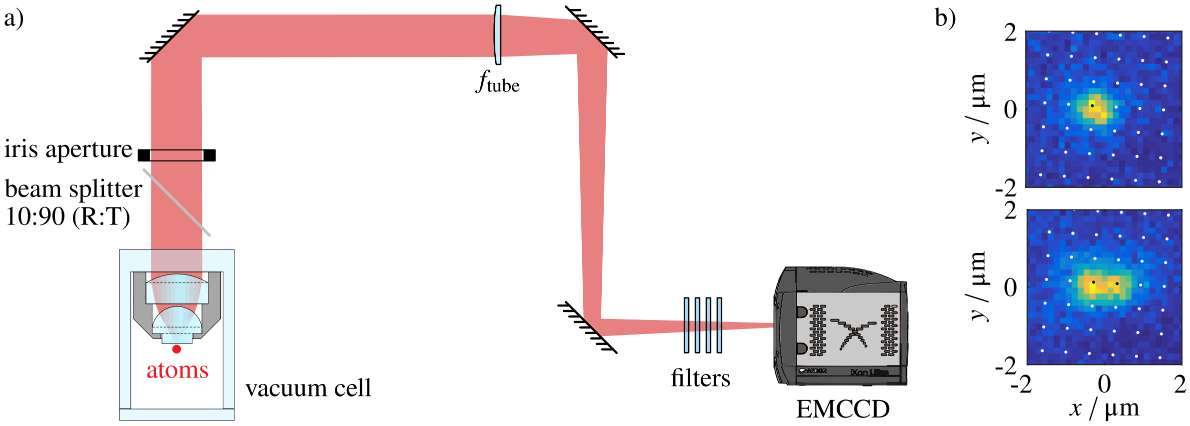

Figure 2.3: a) Schematic of the imaging setup. The fluorescence light of the atoms is collimated by the high-numerical aperture (NA) objective at the working distance of 150 µm into a beam of 22 mm diameter. It then passes a beam splitter (for the vertical MOT and PGC beams) with 90 % transmission for the imaging wavelength of $\lambda_{\mathrm{D2}} = 852\,\mathrm{nm}$. A motorized iris aperture allows to reduce the NA. The light is then focussed down onto the electron-multiplying charge-coupled device (EMCCD) camera by the tube lens. Filters in front of the camera block residual light from the vertical cooling (at $\lambda_{\mathrm{D1}} = 895\,\mathrm{nm}$), the vertical lattice (at $\lambda_v = 1\,064\,\mathrm{nm}$) and stray light. A tube system (not shown in the figure) further reduces stray light. The optics (but not the camera) are mounted on a vertical breadboard located above the vacuum cell. b) Example image of an isolated single atom and of two atoms in adjacent lattice sites. Taken and modified from Reference [15].

2.2 Imaging system

An essential part of any experimental sequence is the detection of the number and position of atoms in the optical lattice. The imaging system used for this purpose is shown schematically in Figure 2.3 a). The in-vacuo objective lens collects and collimates the light from the fluorescing atoms. The maximal half-angle $\alpha_{\max}$ of rays passing the lens defines the NA

$$\mathrm{NA} = n \sin(\alpha_{\max}) \tag{2.1}$$

with the refractive index n of the medium in which the lens is working, which is $n = 1$ for our case of vacuum. With the high NA of 0.92 [59], the DQSIM microscope has an optical resolution of $r_{\mathrm{Abbe}} = \lambda_{\mathrm{D2}}/(2\,\mathrm{NA}) = 460\,\mathrm{nm}$ (Abbe criterion) and a depth of field (DOF) of $\lambda_{\mathrm{D2}}/(2\,\mathrm{NA}^2) = \pm 250\,\mathrm{nm}$. Example images of single atoms are shown in Figure 2.3 b). The field of view (FOV) (area within which the microscope is diffraction limited) expands over ±38 µm [59] or equivalently, a total of about 120 lattice sites. The magnification of the system $M = f_{\text{tube}}/f_{\text{obj}}$ is defined by the effective focal lengths of the objective $f_{\text{obj}} = 11.96\,\mathrm{mm}$ [59] and the tube lens f_{tube}. Depending on the NA, which can be variably adjusted by a motorized iris[3], the magnification is set by the choice of the tube lens so that the field of view covers the chip of the EMCCD[4] as fully as possible. This way an Abbe radius r_A is covered by as many pixels as possible, but at least by the minimum number given by the Nyquist-Shannon condition $r_A > 2\Delta_{\mathrm{s}}$ [39], where $\Delta_{\mathrm{s}} = \Delta_{\mathrm{px}}/M$ is the sampling spacing in the object plane and $\Delta_{\mathrm{px}} = 16\,\mu\mathrm{m}$ is the pixel size of the EMCCD camera. The imaging system was designed with a tube lens $f_{\text{tube}} = 1\,250\,\mathrm{mm}$ for

---

[3] IBM 65 from OWIS GmbH.

[4] iXon Ultra 897 from Andor Technology Ltd.

NA = 0.92, but as atoms were still loaded into several vertical planes, the DOF was meanwhile increased by reducing the NA to ≈ 0.35, while also reducing the magnification by choosing $f_{\mathrm{tube}} = 500\,\mathrm{mm}$ in order to image a wider field of view [18].

The changes I made to the imaging system in view of three-dimensional localization of atoms in the lattice are described in Section 4.5.2 of Chapter 4.

2.3 State-dependent optical lattice

The interaction of atoms with light far from resonance can be used to create conservative potentials in which the atoms can be trapped. Besides optical tweezers or tweezer arrays consisting of tightly focussed laser beams [60], an important realization in the field of quantum simulations are optical lattices formed by interference of counter-propagating laser beams [13, 14, 94]. Optical lattices allow to trap arrays of atoms at distances smaller than the wavelength.

Using two orthogonal polarizations, the lattice in the DQSIM experiment is designed to have two state-dependent components which can be arbitrarily moved with respect to each other along the two horizontal directions. This enables state-dependent transport of atoms, an experimental tool which allows for instance to perform discrete-time quantum walks [20] and multi-particle entanglement [22].

2.3.1 Optical dipole potentials

A semi-classical description based on the Lorentz model applied to a two-level atom gives an intuition on the potential created by a suitably off-resonant laser beam. As shown for example in Reference [95], a light field at a large detuning $\Delta = \omega - \omega_0$ at which saturation can be neglected causes a dipole potential

$$U_{\mathrm{dip}}(\boldsymbol{x}) = \frac{3\pi c^2}{2\omega_0^3}\frac{\Gamma}{\Delta}I(\boldsymbol{x}) \tag{2.2}$$

and a scattering rate

$$\Gamma_{\mathrm{sc}}(\boldsymbol{x}) = \frac{3\pi c^2}{2\hbar\omega_0^3}\left(\frac{\Gamma}{\Delta}\right)^2 I(\boldsymbol{x})\,, \tag{2.3}$$

where ω_0 denotes the atom's resonance, Γ the decay rate and $I(\boldsymbol{x})$ the field intensity. Both U_{dip} and Γ_{sc} are proportional to the intensity. Thus, atoms are attracted towards high intensities for red detunings $\Delta < 0$ and towards low intensities for blue detunings $\Delta > 0$. Furthermore, it follows from Equations 2.2 and 2.3

$$\hbar\Gamma_{\mathrm{sc}} = \frac{\Gamma}{\Delta}U_{\mathrm{dip}}\,. \tag{2.4}$$

High coherence times require a low rate of incoherent scattering of dipole trap photons. Therefore, for a certain potential depth, large detunings and high intensities are used. A residual photon scattering due to the absorptive part of the dipole interaction is however inevitable.

For a complete quantum mechanical description of the two-level system with ground state $|g\rangle$ and excited state $|e\rangle$, a Hamiltonian describing the atom, the (quantized) field and their interaction has to be considered. The interaction part $\mathcal{H}_{\mathrm{I}} = -\hat{\mu}\boldsymbol{E}$ with the dipole operator $\hat{\mu} = -e\boldsymbol{x}$ yields for second-order

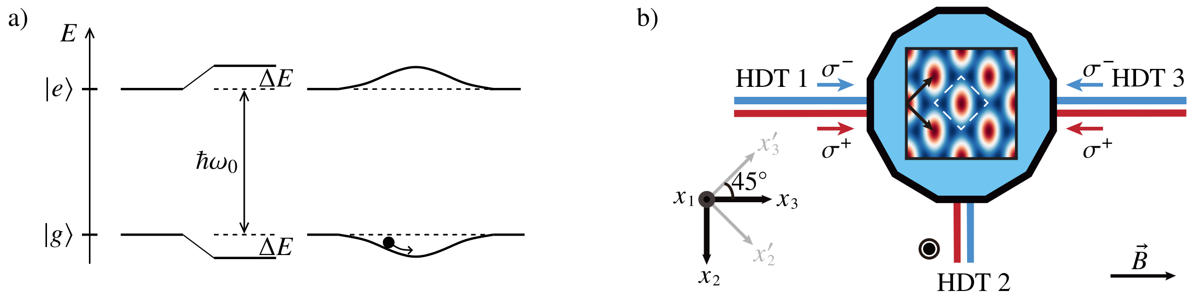

Figure 2.4: a) AC Stark shifts in a two-level system with red-detuned perturbance. On the right side, the resulting potential for a local intensity maximum is schematized. Modified taken from Reference [95]. b) Configuration of the beams and trapping potential of the horizontal optical lattice. Taken and modified from Reference [84].

time-independent perturbation theory shifts of the energy eigenstates by

$$\Delta E = \pm\frac{|\langle e|\mu|g\rangle|^2}{\Delta}|E|^2 = \pm\frac{3\pi c^2}{2\omega_0^3}\frac{\Gamma}{\Delta}I \tag{2.5}$$

compared to the 'bare' eigenstates without the interaction. For the ground state, this AC stark shift exactly corresponds to the dipole potential of Equation 2.2. The excited state shows the exact opposite shift. As shown schematically in Figure 2.4 a), this allows to produce potential wells through spatially inhomogeneous fields for the ground state.

Real atoms have of course a considerably richer level structure. The coupling strength between all sub-levels (which also depend on the laser polarization) has to be taken into account. This leads to the potential depth to be in general depending on the particular atomic state, a fact that will become important in the following Section.

2.3.2 Lattice configuration

We trap atoms in anti-nodes of a bi-chromatic three-dimensional optical lattice. Vertically, i.e. along the optical axis of the imaging objective, the atoms are confined within a standing wave formed by a beam at $\lambda_v = 1\,064\,\mathrm{nm}$ focussed to a waist of $w = 50\,\mu\mathrm{m}$ at the objective lens at which it is retro-reflected.[5] The corresponding vertical lattice spacing thus amount to $\lambda_v/2 = 532\,\mathrm{nm}$. I will refer to it as the vertical dipole trap (VDT).

The horizontal dipole trap (HDT) is a square lattice created by the interference of two counter-propagating beams (HDT 1 and 3) along the quantization axis and a third orthogonal beam (HDT 2).[6] Both HDT 1 and 3 are polarization synthesized, i.e., both intensity and phase of the orthogonal polarizations σ^+ and σ^- are independently controlled by a pair of AOMs [96]. I explain it in Section 2.3.3 HDT 2 is linearly polarized along the vertical. Figure 2.4 b) shows the configuration. The

---

[5] The laser light is provided by a Mephisto MOPA from Coherent Inc. with a maximal output power of 25 W.

[6] The laser light is provided by a titanium-sapphire laser Matisse CS with reference cavity from Sirah Lasertechnik, pumped by a Millennia 20eV from Spectra Physics.

electric field of the horizontal optical lattice is thus described by the superposition

$$\boldsymbol{E}(\boldsymbol{x},t) = \sum_{i=1}^{3} \boldsymbol{E_i}(\boldsymbol{x},t) \tag{2.6}$$

of the three horizontal beams of equal amplitude E_0, wavenumber $k = 2\pi/\lambda_h$, and frequency ω, given by

$$\boldsymbol{E_1}(\boldsymbol{x},t) = \frac{1}{\sqrt{2}}\left(\mathrm{e}^{-\mathrm{i}\phi_1}\hat{\boldsymbol{e}}_{\sigma^+} + \mathrm{e}^{-\mathrm{i}\phi_2}\hat{\boldsymbol{e}}_{\sigma^-}\right) E_0\, \mathcal{E}_1(\boldsymbol{x})\, \mathrm{e}^{\mathrm{i}\boldsymbol{k_1 x}-\mathrm{i}\omega t}\,, \qquad \text{with} \quad \boldsymbol{k_1} = k\hat{\boldsymbol{e}}_{\boldsymbol{3}}\,, \quad \text{and} \tag{2.7}$$

$$\boldsymbol{E_2}(\boldsymbol{x},t) = \frac{1}{\sqrt{2}}\left(\hat{\boldsymbol{e}}_{\sigma^+} + \hat{\boldsymbol{e}}_{\sigma^-}\right) E_0\, \mathcal{E}_2(\boldsymbol{x})\, \mathrm{e}^{\mathrm{i}\boldsymbol{k_2 x}-\mathrm{i}\omega t}\,, \qquad \text{with} \quad \boldsymbol{k_2} = -k\hat{\boldsymbol{e}}_{\boldsymbol{2}}\,, \quad \text{and} \tag{2.8}$$

$$\boldsymbol{E_3}(\boldsymbol{x},t) = \frac{1}{\sqrt{2}}\left(\mathrm{e}^{-\mathrm{i}\theta_1}\hat{\boldsymbol{e}}_{\sigma^+} + \mathrm{e}^{-\mathrm{i}\theta_2}\hat{\boldsymbol{e}}_{\sigma^-}\right) E_0\, \mathcal{E}_3(\boldsymbol{x})\, \mathrm{e}^{\mathrm{i}\boldsymbol{k_3 x}-\mathrm{i}\omega t}\,, \qquad \text{with} \quad \boldsymbol{k_3} = -k\hat{\boldsymbol{e}}_{\boldsymbol{3}}\,. \tag{2.9}$$

The respective polarizations with respect to the quantization axis (along $\hat{\boldsymbol{e}}_{\boldsymbol{3}}$) can be expressed by the unit vectors

$$\hat{\boldsymbol{e}}_{\sigma^+} = \frac{1}{\sqrt{2}}\left(\hat{\boldsymbol{e}}_{\boldsymbol{1}} - \mathrm{i}\hat{\boldsymbol{e}}_{\boldsymbol{2}}\right)\,, \quad \hat{\boldsymbol{e}}_{\sigma^-} = \frac{1}{\sqrt{2}}\left(\hat{\boldsymbol{e}}_{\boldsymbol{1}} + \mathrm{i}\hat{\boldsymbol{e}}_{\boldsymbol{2}}\right)\,, \quad \text{and} \quad \hat{\boldsymbol{e}}_{\pi} = \hat{\boldsymbol{e}}_{\boldsymbol{3}} \tag{2.10}$$

in terms of the Cartesian standard basis $\hat{\boldsymbol{e}}_{\boldsymbol{i}}$. The factors $\mathcal{E}_i(\boldsymbol{x})$ describe the spatial amplitude and phase deformations resulting from the diffraction-limited nature of the respective beams. In a small central region of the lattice we can assume $\mathcal{E}_i(\boldsymbol{x}) \approx 1$, i.e. the plane wave approximation. The total intensity can be decomposed into the contributions of different polarizations $q \in \{\sigma^+, \sigma^-, \pi\}$

$$I(\boldsymbol{x}) = \sum_q I_q(\boldsymbol{x}) \equiv \frac{c\varepsilon_0}{2} \sum_q \left|\boldsymbol{E}(\boldsymbol{x},t)\hat{\boldsymbol{e}}_{\boldsymbol{q}}\right|^2\,, \tag{2.11}$$

which using the intensity of each beam $I_0 = \frac{c\varepsilon_0}{2}E_0^2$ gives

$$I_{\sigma^+} = I_0\left(\frac{3}{2} + \cos\left(k(x_2+x_3) - \phi_1\right) + \cos\left(k(x_2-x_3) - \theta_1\right) + \cos\left(2kx_3 + \theta_1 - \phi_1\right)\right)\,, \tag{2.12}$$

$$I_{\sigma^-} = I_0\left(\frac{3}{2} + \cos\left(k(x_2+x_3) - \phi_2\right) + \cos\left(k(x_2-x_3) - \theta_2\right) + \cos\left(2kx_3 + \theta_2 - \phi_2\right)\right)\,, \quad \text{and} \tag{2.13}$$

$$I_\pi = 0\,. \tag{2.14}$$

Choosing a wavelength between the D1 and the D2 line makes the dipole force sensitive to the qubit states $|{\uparrow}\rangle = |F=4, m_F=4\rangle$ and $|{\downarrow}\rangle = |F=3, m_F=3\rangle$ as well as the polarization. This can be exploited to make the dipole potential of the $|{\uparrow}\rangle$ state insensitive to σ^- polarized light. In fact, it can be shown that the dipole potentials for the qubit states at $\lambda_h = 866\,\mathrm{nm}$ can be expressed by

$$\begin{pmatrix} U_\uparrow \\ U_\downarrow \end{pmatrix} = c_0 \begin{pmatrix} 1 & 0 & 1/2 \\ 1/8 & 7/8 & 1/2 \end{pmatrix} \begin{pmatrix} I_{\sigma^+} \\ I_{\sigma^-} \\ I_\pi \end{pmatrix}\,, \quad \text{with} \quad c_0 = -k_\mathrm{B} \times 2.717\,\mathrm{pK/(W/m^2)}\,. \tag{2.15}$$

The derivation is shown for example in Reference [97]. From Equations 2.12, 2.13, 2.14 and 2.15 it becomes apparent that by controlling both phase ($\phi_{1,2}$, $\theta_{1,2}$) and intensity of both circular polarizations,

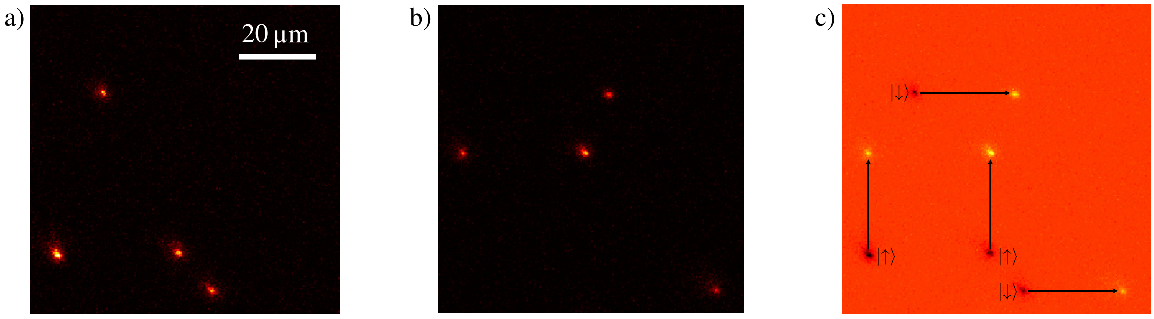

Figure 2.5: State-dependent transport along orthogonal directions. Taken and modified from Reference [17]. a) Initial position of atoms in the lattice. Atoms are initially prepared in $|\uparrow\rangle$. After a certain waiting time, the population becomes a mixture of $|\uparrow\rangle$ and $|\downarrow\rangle$. b) Image taken after state-dependent transport over 40 lattice sites upwards for $|\uparrow\rangle$ and to the right for $|\downarrow\rangle$. c) Difference image between b) and a).

the lattice potential of both qubit states can independently be moved along both horizontal directions, thus allowing state-dependent transport. Each qubit state experiences a square lattice with a lattice constant $\lambda_h/\sqrt{2} = 612\,\mathrm{nm}$ and an elliptical trapping potential with tighter confinement along HDT 1/3, as shown in Figure 2.4. By setting all phases to zero and using the same intensity $I_{\sigma^+} = I_{\sigma^-}$, the same lattice potential is prepared for both qubit states.

A detailed description of the state-dependent optical lattice can be found in References [15, 20]. The two-dimensional state-dependent transport was recently demonstrated as reported in Reference [17] and shown in Figure 2.5.

2.3.3 Polarization synthesizer

The polarization synthesizer allowing independent control of the lattice potentials of both qubits is based on digital intensity and phase control using a pair of AOMs modulating two orthogonal polarizations. The setup is shown exemplarily for the HDT 1 arm of the lattice in Figure 2.6. An identical setup exists for HDT 3. The light is split into two linear polarizations by a polarizing beam splitter. AOMs in single-pass configuration modulate the phase and intensity. The first diffraction order is send through Wollaston prism to further clean the polarizations and is then recombined by another Wollaston prim. The beam is then mode-cleaned by a polarization-maintaining optical fiber. Pickup-plates split some light for intensity and phase feedback, which is split into orthogonal polarizations using Wollaston prisms and detected by amplified photodetectors. A pair of two waveplates allows to match the prism's polarization axes, thus minimizing feedback crosstalk between the polarizations. Finally, a quarter-wave plate converts the linear polarizations into circular. As the quantization axis is parallel to the beam, these correspond to σ^+ and σ^- polarizations. HDT 1 and HDT 3 both have a reference beam of equal optical length picked up shortly after the laser output to allow phase feedback. The feedback control is realized by arbitrary waveform generators and a digitizer[7] with an integrated field programmable gate array (FPGA)[8] on which PID-control is programmed.

The polarization synthesizer achieves a crosstalk extinction ratio of less than 10^{-5} [17], which I was

---

[7] M3300A6 from Keysight.

[8] Kintex-7K410T, Xilinx, Inc.

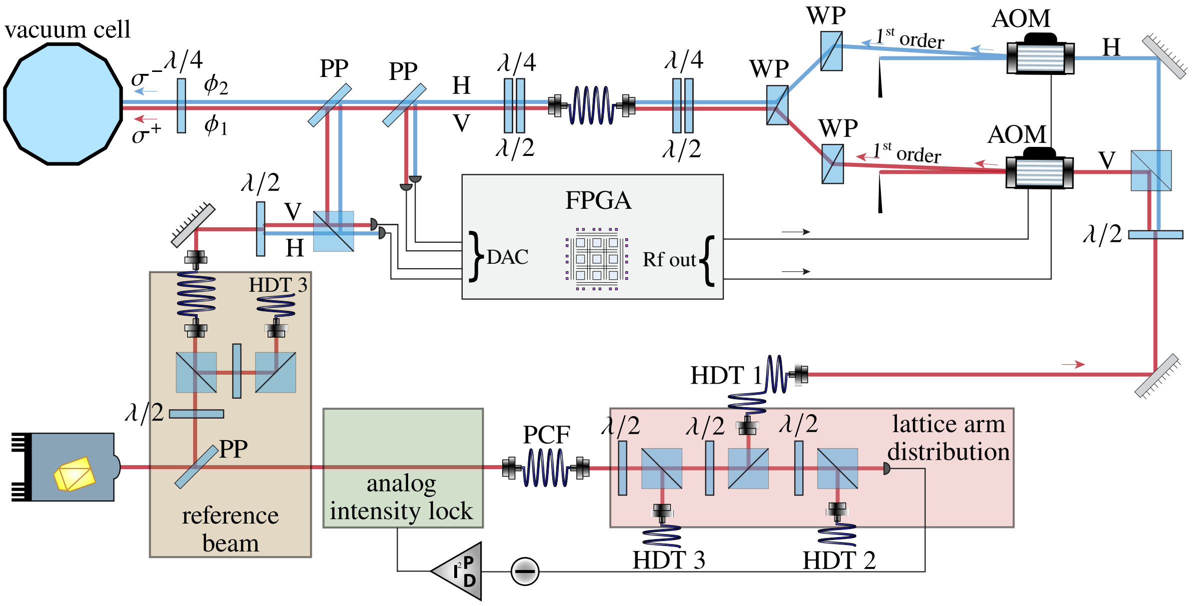

Figure 2.6: Schematic of the polarization synthesizer for HDT 1. Parts were taken from Reference [84].

able to regain by readjustment after a longer shutdown of the experiment. As changing Rf powers[9] at the AOMs cause pointing instabilities, an additional analog intensity lock precedes, allowing a higher dynamic range and to run the AOMs at nearly constant Rf power. In order to augment the power usage of the titanium sapphire laser for a deeper horizontal lattice, I changed the analog feedback as I report in Section 3.2. My changes also include the replacement of the previous setup distributing the light for each lattice arm into conventional polarization maintaining fibers[10] leading from the laser table to the experiment table (cf. References [17, 84]) by a single large mode area photonic crystal fiber (PCF) fiber and subsequent distribution into the lattice arms. Besides the thereby higher possible lattice intensities, it has the practical advantage of recoupling into only a single fiber which is regularly necessary due to pointing instabilities of the laser. Furthermore, this allowed me to move the photodetector giving the intensity feedback on the other side of the fiber, thus including intensity changes due to coupling efficiency changes into the feedback loop.

---

[9] In a typical experimental sequence, the lattice is lowered during the coherent experimentation.

[10] P3-780PM-FC-10, Thorlabs Inc.

CHAPTER 3

Atom hopping suppression via deep lattice potentials

Optical dipole traps have potential depths limited by the trapping light intensity. Typical trap depths are below 1 mK [95]. Therefore, laser cooling techniques such as the optical molasses and polarization gradient cooling (PGC) are employed to cool the atoms before loading them into the dipole trap (see Section 2.1). In experiments simulating condensed matter Hamiltonians, finite tunneling probabilities of atoms between lattice sites are part of the desired simulated system, for instance, electrons in a crystal lattice [25]. In state-dependent transport experiments, however, uncontrolled hopping of atoms to other lattice sites is undesirable. Therefore, sufficiently deep lattice potentials are employed bringing the tunneling probabilities close to zero.

However, in our two-dimensional discrete quantum simulator (DQSIM), hopping could not be suppressed to a satisfying level during imaging with PGC beams in the past [17, 84]. In this chapter, I present my contributions to the apparatus allowing a twofold increase in horizontal dipole trap (HDT) depth promising a higher suppression of hopping. This is not only a prerequisite for planned measurements relying on deterministic transport and imaging, but also for the demonstration of three-dimensional imaging which I present in Chapter 4. For this purpose, I have improved the power handling of the analog intensity feedback as I describe in Section 3.2. Moreover, Section 3.3 presents the characterization of a polarization-maintaining photonic crystal fiber (PCF) replacing conventional fibers, as its large mode area allows significantly higher damage thresholds and lower stimulated Brillouin scattering. I designed and built a fiber coupler to launch the beam with high coupling efficiency into the PCF. Finally, as I present in Section 3.4, I measured and compensated the ellipticity and the astigmatism of the beam originating from the laser resonator geometry allowing high fiber coupling efficiencies.

3.1 Optical lattice depths and hopping

For the simplified model of a cubic lattice of infinite extent, the hopping probability of an atom in the vibrational ground state to a neighboring site gets below 1 % at a potential depth of $U/E_\mathrm{r} \geq 20$[1] [25], which assuming an average recoil energy of the D1 and D2 line of $E_\mathrm{r} = k_\mathrm{B} \times 189\,\mathrm{nK}$ [98] corresponds to $U \geq k_\mathrm{B} \times 3.8\,\mu\mathrm{K}$ for our optical lattice. During the coherent experimentation, the lattice is adiabatically

---

[1] The hopping matrix elements of the single-particle Bloch eigenstates are computed on p. 897 of Reference [25].

lowered to a depth of 50 µK for minimal scattering with lattice photons.[2] Following the simple model calculation, it can be concluded that the lattice potential is deep enough to suppress hopping of motional ground state atoms to a large extent. In fact, sideband cooling techniques allow temperatures of ≈ 1 µK at which more than 90 % of the atoms are in the motional ground state [17, 84] (cf. Section 2.1).

However, during imaging, a higher thermal equilibrium of the PGC at ≈ 6 µK [17] is inevitable, as the imaging relies on the scattered photons of the PGC beams. At this temperature, atoms also occupy higher vibrational states which have larger tunneling probabilities. During imaging, the coherent evolution of the qubit state becomes irrelevant allowing to use higher optical lattice intensities for deeper trapping potentials. Being ultimately limited by available laser power, horizontal trap depths of 750 µK were previously reached during the imaging, while vertically, a depth of 280 µK is used. The horizontal and vertical hopping of atoms could however not be sufficiently eliminated [17, 84].

The frequency and intensity of the PGC beams are chosen to maximize the survival in a small central region of the vertical dipole trap (VDT). However, the spatially inhomogeneous light shifts induced by the VDT reducing to 50 % at a distance of 30 µm from the center make it challenging to optimize the parameters over the entire field of view (FOV) simultaneously [84]. Since significantly more power is available from the VDT laser, the VDT beam waist could be increased while maintaining the intensity, allowing more homogeneous conditions. The intensity of the HDT is limited by the titanium-sapphire laser power. Increasing the potential depth promises a reduction of the hopping rate.[3] For this purpose, the entire setup was assessed for a more efficient use of available power.

In the previous setup [17, 84], the bottleneck in the HDT optical power was the laser damage threshold (LDT) of the intensity-steering electro-optic modulator (EOM)[4] of 2.8 W,[5] a limited fiber coupling efficiency due to astigmatism and ellipticity of the beam's transverse mode and the damage threshold and limit of stimulated Brillouin scattering of the three fibers guiding the light between the optical tables. Overall, only 8 % of the 6.7 W laser power was arriving at the vacuum cell. This includes also the losses arising in the polarization synthesizer (cf. Section 2.3.3), for instance due to maximal acusto-optic modulator (AOM) diffraction efficiencies of ≈ 90 %, losses at optical surfaces and finite fiber coupling efficiencies.

3.2 An AOM intensity control

The combination of a polarizer and an EOM is a common intensity modulator. Consisting of a crystal on which a controllable electric field is applied, the linear electro-optic effect modulates the birefringence of the crystal [99]. A linear polarization incident at 45° with respect to the slow or fast axis is thereby rotated depending on the electric field. The subsequent polarizer turns the polarization modulation into

---

[2] In this section, I calculated the HDT potential depths by the Equations 2.12, 2.13, 2.14 and 2.15 with a peak intensity of $I_0 = 2P/(\pi w_h w_v)$ in each lattice arm, where P is the optical power per arm, $w_h = 75\,\mu\text{m}$ and $w_v = 25\,\mu\text{m}$ are the horizontal and vertical beam waists of the elliptical HDT beams.

[3] It should be noted that the scattering rate of the (far off-resonant) lattice photons also increases proportionally with intensity (see Equation 2.3), resulting in additional heating. Very high lattice beam intensities can thus lead to shorter lifetimes in the deep lattice.

[4] Conoptics Inc. M350-105 with high voltage amplifier model 302RM and Glan-Laser polarizer. The EOM M350-105 was used to replace an EOM LM0202-IR from Gsänger Optoelektronik GmbH with 5 W LDT, whose crystal was damaged presumably due to a change in pointing caused by a temperature excursion of the laboratory.

[5] The manufacturer specifies a LDT of 5 W mm^{-2}. Assuming the beam of total power P to be Gaussian and using the measured waist of $w = 0.6$ mm, the LDT in optical power can be computed from the relation for the on-axis intensity $I = 2P/(\pi w^2)$.

an intensity modulation. In order to increase the dynamic range of the digital intensity locks for the optical lattices which have to be ramped up and down between coherent experimentation and imaging (cf. Section 2.1), an EOM has been employed to steer the intensity within an additional analog feedback loop. In addition, the higher achievable feedback bandwidth of 580 kHz [100] compared to the digital control achieving 230 kHz [101] allows a higher intensity noise suppression which is important as intensity noise contributes to decoherence [102].

AOMs on the other hand diffract incident light based on the acusto-optic effect [99]. An acoustic wave at radio frequency is sent through a crystal creating a sinusoidal grating of the refractive index. In the Bragg regime, the diffraction is mostly into the first order. By controlling the amplitude of the acoustic wave, the diffraction efficiency can be tuned, thus allowing intensity modulation. EOMs typically have higher LDTs as larger apertures are available. As the transmission efficiency of EOMs is only limited by the optical surface qualities, they can reach $\geq 98\,\%$ with anti-reflective (AR) coated surfaces, while the transmission efficiencies of AOMs suffer in addition from limited diffraction efficiencies, allowing up to 90 % into the first order. For high powers, EOMs are therefore typically chosen. However, for the available devices, the AOM's LDT of $250\,\mathrm{W/mm^2}$ is significantly larger than the EOM[6] with $5\,\mathrm{W/mm^2}$. Despite the smaller aperture of the AOM, the full power of the laser can be used. AOMs are also more resource-efficient as the crystals are easier to manufacture and no high-voltage drivers are needed. Furthermore, the AOM at hand allows modulation up to 20 MHz[7] compared to the modulation bandwidth of the EOM limited by the high-voltage driver to 200 kHz. Therefore, I decided to replace the EOM with an AOM.

The AOM is operated in a so-called double-pass cat-eye configuration as shown in the highlighted area of Figure 3.1, because it has higher beam-pointing stability than a single-pass configuration. The technique is reported in the References [103, 104]. After the AOM, the beam passes through a lens and is retroreflected by a mirror. The distances between AOM center, lens of focal length $f = 75\,\mathrm{mm}$ and mirror are chosen to be f each, such that diffraction angle drifts, for instance due to thermalisation processes in the AOM crystal do not affect the beam pointing, as the beam is retro-reflected onto itself independent of the angle (therefore *cat-eye*). Due to the finite sound speed, smaller beam sizes allow shorter reaction times. However, they also reduce the diffraction efficiency. As the feedback bandwidth is not limited by the AOM but rather the analog controller[8], I chose a larger beam size for the highest diffraction efficiency. The manufacturer specifies a maximal diffraction efficiency of 85 %[9] for a beam width of $w = 250\,\mu\mathrm{m}$. At the position of the AOM, the width of the ellipticity- and astigmatism-compensated beam amounts to $800\,\mu\mathrm{m}$ (cf. Section 3.4). Therefore, a 3:1 telescope[10] brings the beam to a width of around $270\,\mu\mathrm{m}$. A quarter-wave plate between AOM and cat-eye lens allows to turn the linear polarization of the beam by 90°. After passing the AOM in the other direction, the beam is deviated by a polarizing beam splitter. In order to reach high transmissions, I chose to stabilize the 0th order at the cost of a lower extinction ratio. I achieved 91.6 % maximal transmission which corresponds to the losses at the optical surfaces and 1:900 extinction. The light in the 1st order[11] is reflected away using a knife-edge mirror in front of the retro-reflecting mirror and sent towards the setup of the optical polarization gradient (see Reference [84]).

---

[6] AOMO 3080-122 from Gooch & Housego PLC, driven by a RF driver built by and generously made available by the Hofferberth Group.

[7] As the analog PI^{2}D-Servo has a bandwidth of 10 MHz, this can not fully be used.

[8] D2-125 Laser Servo from Vescent with 10 MHz bandwidth.

[9] At the wavelength 830 nm.

[10] A telescope with $f_1 = 150\,\mathrm{mm}$ and $f_2 = -50\,\mathrm{mm}$ separated by $f_1 + f_2$ is chosen.

[11] The maximal diffraction efficiency reached into the 1st order is 85 % when the HDT intensity is steered to extinction.

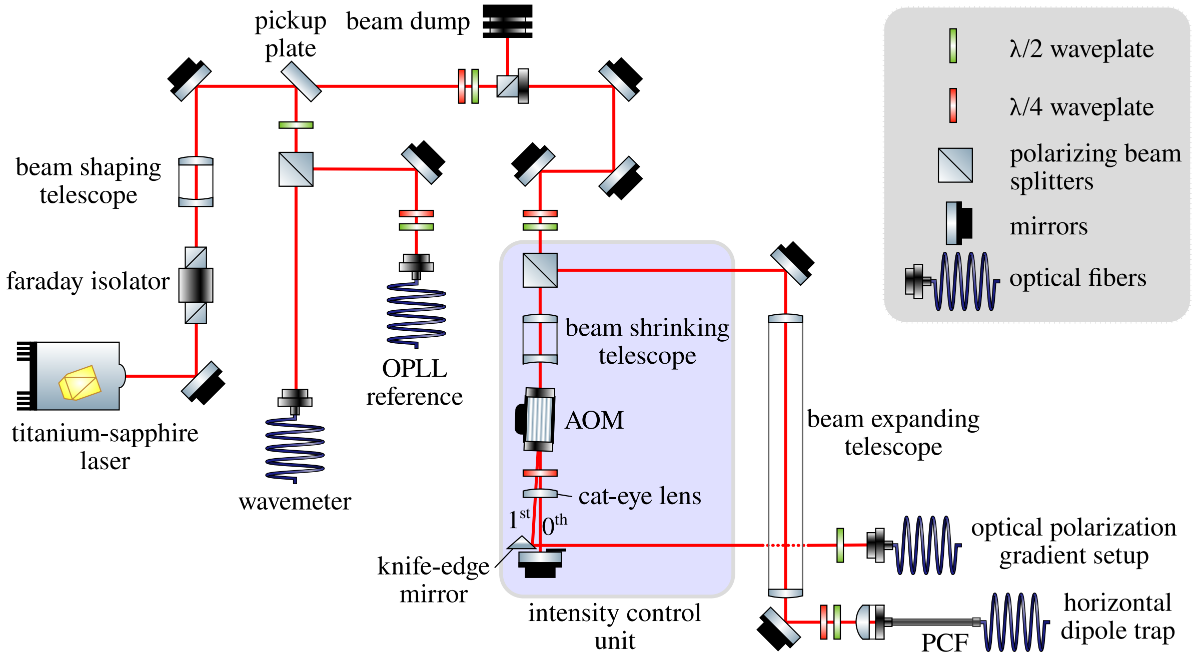

Figure 3.1: Schematic of the HDT optical setup for beam distribution and intensity control.

The analog intensity lock is built using a Servo[12] and an amplified photodetector[13]. The photodetector is placed after the fiber leading to the experiment table, improving the passive stability of the setup and making it insensitive to pointing instability e.g. of the laser. This is made possible by using only one fiber leading from the laser table to the experiment table and placing the setup distributing the beam into the three HDT arms on the experiment table (cf. Figure 2.6). The step-response and the relative intensity noise power spectrum were measured to quantify the quality of the lock. A feedback bandwidth of 350 kHz and a relative intensity noise comparable to the stability achieved with the previously used EOM [100] was reached.

With this setup, I was able to improve the maximum optical power incident on the fiber from 2.7 W to 4.2 W, i.e., by about 55 %. While this is a significant improvement, this also necessitates the use of a large mode area PCF which can support this high optical power.

3.3 A large mode area photonic crystal fiber

The delivery of laser light to the atoms on another optical table at the diffraction limit requires polarization-maintaining guidance of the fundamental Gaussian mode. Optical fibers predestined for this purpose (and commonly used) are single-mode step-index fibers with birefringence which retains linear polarization when coupled into the fast or slow axis (therefore *polarization-maintaining*). In the previous setup, the beam divided into the three HDT arms was launched into such 10 m long fibers.[14] However, at high optical powers, fibers suffer from stimulated Brillouin scatting causing back-reflections

---

[12] D2-125 Laser Servo from Vescent.

[13] PDA10A-EC Si amplified photodetector from Thorlabs Inc.

[14] P3-780PM-FC-10, Thorlabs Inc.

of a considerable part of the light. This effect is described, for example, in Reference [105]. For the fibers in use, measurements have shown that incident optical powers of the order of 1 W could be used at maximum [106]. Brillouin scattering is a non-linear effect in which photons are inelastically scattered by acoustic phonons in the medium. At low intensities, such spontaneous events contribute to negligible backscattering. There is however a threshold at which this non-linearity can lead to a stimulated Brillouin scattering causing the back-reflection of most of the light. The threshold linearly increases with the fiber length. As the local intensity is proportional to the effective mode area of the fiber, larger mode areas can be used to guide higher optical powers.

Increasing the core size of regular step-index fibers does not allow for larger mode areas in single-mode operation. However, the design flexibility given by PCF allows for large mode areas. PCFs have solid or hollow cores and a periodic arrangement of air-filled holes spaced at the length-scale of the wavelength and running through the entire fiber. I used a solid-core endlessly single-mode PCF[15] with a mode field diameter of 12.4 µm compared to the 5.3 µm of the conventional fiber. This corresponds to a 5.5-fold mode area and concomitant increase in stimulated Brillouin scattering threshold. The PCF is made of pure silica with a hexagonally symmetric lattice of microscopic air-filled holes creating a cladding of lower effective refractive index allowing light to be guided through the core. Two stress rods create a linear birefringence that results in two different polarization modes and allows polarization to be maintained. At the end facets, the holes are collapsed.

Return loss. A high cleavage angle of 12° minimizes Fresnel back-reflections. However, the fiber has no AR coating, which leads to a sub-optimal impedance matching causing ≈ 4 % reflection losses at each surface. In the experiment, the HDT 1 and 3 beams are counter-propagation in the same transverse mode. A considerable amount of light is therefore returning back towards the laser after passing through the vacuum cell (cf. Figure 2.6). If this back-propagating light is reflected back into the polarization synthesizer towards the vacuum cell, detrimental interference patterns could occur. Therefore, a high suppression of back-reflection into the same transverse mode, has to be achieved for any utilized fiber. The so-called return loss of the previously used step-index fibers specified by the manufacturer is sufficiently high with 60 dB. However, the company splicing and cleaving the PCF[16] does not characterize the return loss. I therefore measured the return loss. For this purpose, I used a setup as shown in Figure 3.2. A beam splitter allows to separate the back-reflected light of a fiber under test towards a power meter. A mode filtering fiber ensures that only light in the same transverse mode is measured.[17] Taking into account the measured coupling efficiencies and the beam splitter reflectivities, the return loss can be calculated from the measured optical power. I measured the return loss of the PCF and a self-built fiber coupler to be (48 ± 3) dB.[18] This coincides with the measured (47 ± 3) dB for a conventional fiber without AR coating and a commercial fiber coupler[19], while (62 ± 4) dB confirmed the manufacturer's specification for a AR-coated fiber. When using custom-built commercial fiber couplers[20] for the PCF, I reached only (41.5 ± 1.2) dB. I conclude that the PCF has a sufficiently high return loss, especially

---

[15] LMA-PM-15 from NKT Photonics A/S.

[16] Centre Technologique Optique et Lasers ALPhANOV.

[17] The setup is aligned by replacing the beam dump with a mirror and maximizing the coupling efficiencies.

[18] The reported measurement uncertainties were estimated from temporal fluctuations of the measured power, which I attribute to imperfect polarization maintenance of the fibers.

[19] Schäffter+Kirchhoff 60FC-4-M12-33.

[20] Centre Technologique Optique et Lasers ALPhANOV.

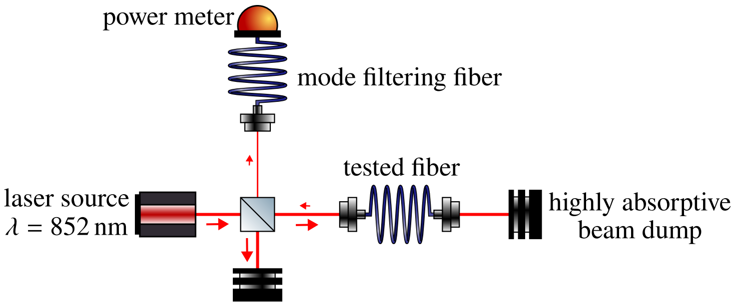

Figure 3.2: Return loss measurement setup. A laser beam passing a non-polarizing 50:50 beam splitter is coupled into a fiber under test and is subsequently blocked by a highly absorptive beam dump. Only light back-reflected at refractive index interfaces within the tested fiber (or fiber couplers) is coupled into a fiber assuring only light in the same transverse mode is measured. A power meter measures the power from which the return loss can be computed.

when using the self-built fiber coupler. It could be improved by an additional AR coating.

Custom fiber coupler. I have designed and built a fiber coupler for the PCF fiber ensuring a high return loss, but especially also allowing high coupling efficiencies. A high fiber coupling efficiency is not only needed to achieve deep dipole potentials, but also to prevent damage to the fiber ferrules due to excessive heat generation and to ensure intensity stability. The coupler must focus the beam onto the fiber end facet while matching the mode field diameter. It must furthermore have a high mechanical stability while having the necessary degrees of freedom to optimize the fiber coupling.[21] I chose a design based on a cage mount allowing to precisely adjust the axial position of the coupler lens with respect to the fiber end facet.[22] The required angular degrees of freedom are achieved by two mirrors ahead of the coupler. A lens of suitable focal length and sufficient optical quality to avoid aberrations leading to lower coupling efficiency has to be chosen. By measuring the beam profile of a collimated beam coupled out of a coupler with a specific lens, a lens is found that matches the beam width at the desired coupler position.

As can be seen in Figure 3.1, a beam expanding telescope was additionally used to match the beam width of the chosen coupler lens.[23] At high powers ≥ 4 W a coupling efficiency of 71 % could be achieved in the setup shown in Figure 3.1 after compensation of the beam ellipticity and astigmatism. Despite the hexagonal cladding geometry, the PCF fiber mode has a high overlap with the mode of conventional fibers, as coupling efficiencies of 89 % are achieved therebetween.[24] The coupling efficiency of the laser beam into a (short) conventional fiber without AR coating was achieved with up to 84.7 % at the same position. I therefore expect that improvements of the PCF coupling are possible. Moreover, the usage of AR coated PCFs would yield about 7 % higher efficiencies.

---

[21] The available commercial couplers have a strong coupling of the angular degrees of freedom with the axial lens position, which makes coupling with them rather unwieldy.

[22] The fiber ferrule with SMA connector is screwed on a custom made aluminium cage plate on which a hollow cylinder with SMA thread at 6° corresponding to the measured output angle allows an immediate correct coarse alignment (as with common commercial mounts) as well as a centering in the cage system.

[23] The lens is a AC254-030-B from Thorlabs. If a more suitable lens is available, the telescope is of course not necessary and should be avoided.

[24] This measurement was done at ≈ 100 mW with an AR coated conventional fiber. The commercial fiber couplers did not yield better coupling efficiencies.

3.4 Astigmatic-elliptical beam shaping

In this section, I report on improving the single mode fiber coupling efficiency for the titanium-sapphire ring laser used for the optical lattice by astigmatic-elliptical beam shaping using a cylindrical telescope. To this end, I measured the transverse mode profile of the laser beam exiting the ring resonator and modelled it as an astigmatic-elliptical Gaussian beam. I then design a suitable setup for the cylindrical telescope by simulating Gaussian beam propagation and finally test it experimentally. The fiber coupling efficiency into a single mode step-index fiber could be increased from 78 % to 86 % in this way.

3.4.1 Matching the laser transverse mode to the fiber mode

In order to have high fiber coupling efficiencies into single mode fibers, the coupled optical field should have highest possible mode overlap with the guided mode at the fiber's input end [107]. Owing to the simplicity of Gaussian mode profiles and the usually good agreement, it is common to approximate the fiber mode using Gaussian functions [108].

Lasers in single-mode operation often approach Gaussian beam shape given by the optical resonator transverse mode [109]. Gaussian beams are the fundamental mode solution of the paraxial Helmholtz equation (cf. Appendix A.1 and Section 4.4.1). For a given beam size, they represent the beam which can be most tightly focussed and have the smallest divergence. Inhomogeneous optical media, for example by thermal lensing in the gain medium, can cause deviations [110]. In fact, any deformations of the wavefront lead to a reduction of the beam quality, for instance, due to aberrations of optical elements. Gaussian beams have a transverse intensity profile

$$I(r,z) = I_0 \left(\frac{w_0}{w(z)}\right)^2 \exp\left(\frac{-2r^2}{w^2(z)}\right) \tag{3.1}$$

with a beam radius

$$w(z) = w_0\sqrt{1+\left(\frac{z}{z_\mathrm{R}}\right)^2}\,, \tag{3.2}$$

where

$$z_\mathrm{R} = \frac{\pi w_0^2}{\lambda} \tag{3.3}$$

is the Rayleigh range [109]. Figure 3.3 shows the instantaneous intensity of a Gaussian beam. The phase profile at the waist $z = 0$ is flat, however, diffraction causes a curved wavefront upon propagation. The curvature is largest at the Rayleigh distance z_R.

A beam is coupled into the fiber by a collimator lens, which for a Gaussian beam transforms into another Gaussian beam of different waist and focus position, as we will see. For a high coupling efficiency, the laser beam should be a Gaussian beam with a waist w_0 and waist position which coincide with the fiber mode width and input end position. Correspondingly, a low beam quality factor, ellipticity, astigmatism, or simply a differing waist or waist position can significantly reduce the coupling efficiency. The latter can easily be matched by carefully choosing the fiber collimator lens and/or the use of a (de)magnifying telescope.

Figure 3.4 schematically shows the ring cavity of the titanium-sapphire laser used. As the two curved cavity mirrors reflect the beam at an angle different from zero with respect to the normal direction, the

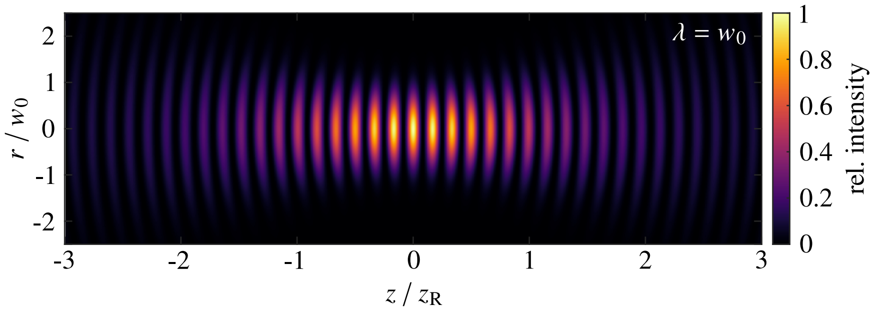

Figure 3.3: Instantaneous intensity of a Gaussian beam with $\lambda = w_0$. The full expression of transverse mode is given by the fundamental Laguerre-Gauss (LG) mode Equation 4.6 in Section 4.4.1.

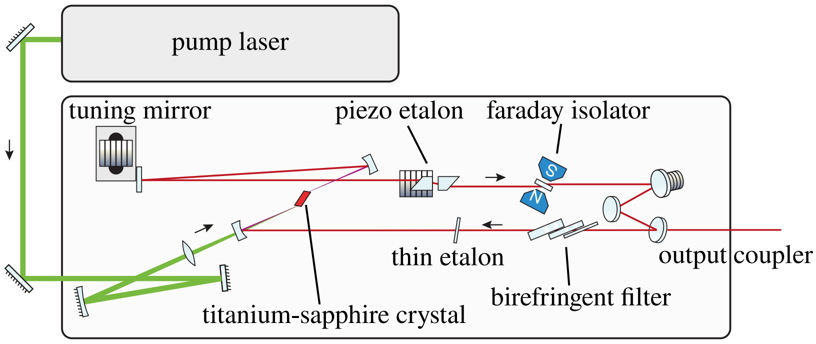

Figure 3.4: Titanium-sapphire laser system. A pump laser (diode pumped solid state laser) pumps the titanium-doped sapphire crystal. The crystal is enclosed by a ring resonator consisting of four flat mirrors and two concave mirrors focussing the resonator mode in the crystal. Etalons and a birefringent filter tune the longitudinal mode. A Faraday isolator introduces a directionality in the ring resonator. The finite transmission of one mirror allows the light to couple out of the resonator. Schematic created by Dr. Andrea Alberti.

focus of the resonator mode will differ in the horizontal and vertical direction, i.e. the mode will have some astigmatism. The output field of the laser is coupled out through a flat mirror, thus the laser beam retains the astigmatism. The circularity of the mirrors is effectively elliptical when viewed at a certain angle, so the output mode of the laser beam also has a certain asymmetry of horizontal and vertical waist size, i.e., it is elliptical. The Gaussian beam model can be easily extended to include ellipticity and astigmatism by using distinct values of each parameter for the horizontal and vertical axis and distinct definitions of the $z = 0$ point [111].

Common techniques to circularize beams, widely used e.g. for diode lasers which output highly elliptical beams, are anamorphic prism pairs [112], spatial filtering and cylindrical telescopes [113], whereby only the latter offers full control over the beam's astigmatism. We will therefore first characterize the astigmatism and ellipticity of the laser beam to then compensate it with a cylindrical telescope.

3.4.2 Measurement and modelling of the laser mode

The output beam of the laser is characterized by recording transverse intensity profiles at different distances, ideally covering both the near and far field. An example measurement is shown in Figure 3.5 a). In our case, the waist lies outside the laser. As the laser mode depends on the laser output power due

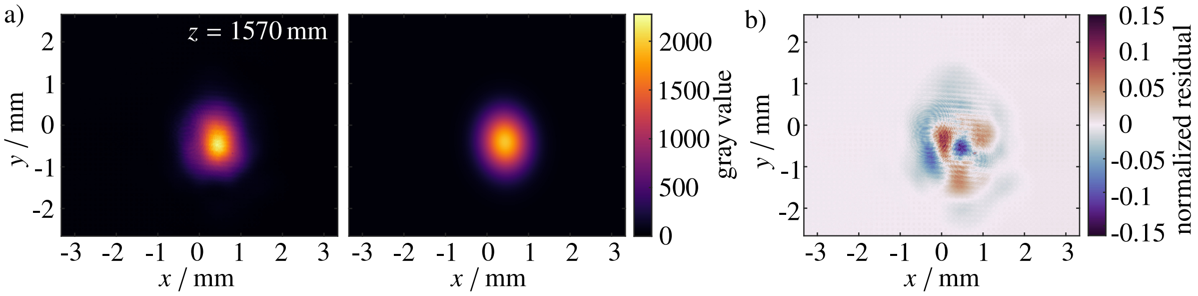

Figure 3.5: a) Example of a recorded intensity profile with corresponding two-dimensional Gaussian fit. b) The normalized residual corresponding to the difference of the fitted and measured profile, divided by the maximum of the fitted profile.

to thermal lensing, the measurement must be performed at the power used later. Our goal is to have the highest possible power available on the other side of the fiber, we therefore set the pump laser at its maximal 25 W, yielding 6.7 W output power of the titanium-sapphire laser at $\lambda_h = 866\,\mathrm{nm}$. The camera used to record the beam profile[25] can only be placed after a Glan-Laser calcite polarizer which allows to significantly attenuate the beam. In our setup, this is preceded by an optical isolator and a pickup plate (cf. Figure 3.1).

In order to predict possible fiber coupling efficiencies and find based on this model suitable focal lengths and lens positions for a cylindrical telescope, the measured transverse intensities are modelled as an astigmatic-elliptical Gaussian beam. For this purpose, I fit a two-dimensional elliptical Gaussian function with symmetry axes rotated by some angle with respect to the camera axes. Figure 3.5 a) shows an example least squares minimization fit. The angle degree of freedom is not expected to be needed, as in our setup, the axes of the camera chip are expected to match the axes of the astigmatism, being the horizontal and vertical with respect to the optical table (or the ring cavity). Yet we still measure an angle 6°, which in a second iteration is set as a fixed fit parameter. I attribute this angle to a corresponding tilt of the camera sensor with respect to the optical table.

The residuals shown in Figure 3.5 b) reveal a reasonably good description of the data by the chosen model. The existing deviations show a non-perfect beam quality, which, as mentioned, are caused by thermally induced optical inhomogeneities in the laser crystal and by aberrations of the preceding optical elements. The almost horizontal stripe pattern visible in the example image originates from a corresponding modulation of the infrared sensitivity of the camera chip due to etalon interference effects between optical surfaces on the chip. Because of its homogeneity across the image area and its small period relative to the beam width, it is not affecting the fit. The same applies to the two diffraction rings visible on close inspection, presumably caused by dust grains.

The beam profile is measured this way at different distances, taking the end facet of the optical isolator as position reference. To determine the parameters of our astigmatic-elliptical Gaussian beam model, I then fit the beam radii w obtained from each intensity profile measurement in both transverse axes independently as

$$w(z) = w_0\sqrt{1 + \left(\frac{z - z_0}{z_\mathrm{R}}\right)^2} \tag{3.4}$$

---

[25] DC1545M complementary metal-oxide-semiconductor (CMOS) camera from Thorlabs.

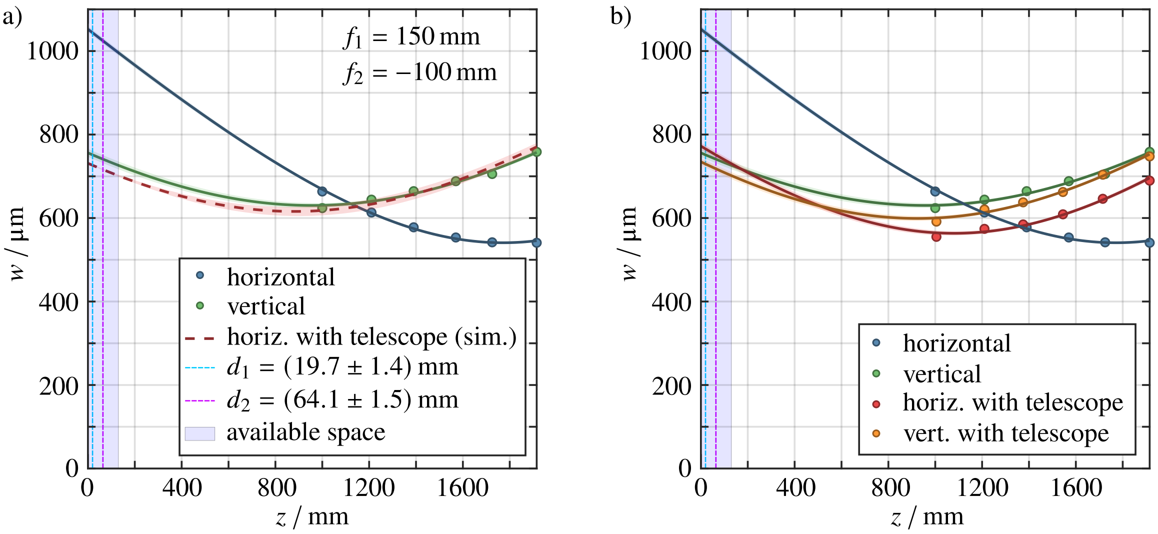

Figure 3.6: Beam radius as a function of distance with astigmatic-elliptical Gaussian beam fits. The 1σ-confidence interval of the fits are shown as shaded surfaces. a) The transformation of a cylindrical telescope of lenses with focal lengths f_1 and f_2 at positions d_1 and d_2 (shown as vertical dashed lines) acting on the horizontal axis is computed using the Gaussian beam model. A fit of the vertical axis data to the transformed horizontal axis gives the telescope's parameters and is shown in red. b) Measured beam radii with and without the cylindrical telescope.

with the corresponding waist position z_0. The fit result is shown in Figure 3.6 a). We get the waists $w_{0,h} = (541 \pm 2)\,\mu\mathrm{m}$ and $w_{0,v} = (630 \pm 5)\,\mu\mathrm{m}$ and their positions $z_{0,h} = (1\,771 \pm 11)\,\mathrm{mm}$ and $z_{0,v} = (955 \pm 26)\,\mathrm{mm}$. The astigmatism, i.e. the distance of the waist positions of each axis, amounts to (816 ± 29) mm. This is not negligible compared to the mean Rayleigh range $z_\mathrm{R} = 1.24\,\mathrm{m}$. The ellipticity is the ratio of the divergences, which equals the inverse ratio of the waists and amounts to 1.165 ± 0.011.

3.4.3 Finding a suitable cylindrical telescope

Cylindrical lenses act on one axis only. Therefore, a telescope of cylindrical lenses can circularize an elliptical beam by enlarging or reducing one axis. By fine adjustment of the relative lens position, the focus of the axis subject to the cylindrical lenses can be shifted, allowing the astigmatism of the beam to be corrected.

In order to describe the effect of the lenses on a Gaussian beam in a simple way, I introduce a common parameterization, which is well described in Reference [109]. A Gaussian beam of certain wavelength is fully described by two real numbers, for instance the Rayleigh length z_R and the waist position z_0. Accordingly, the Gaussian beam can be described by a single complex number, the so-called complex beam parameter

$$q = z - z_0 + \mathrm{i} z_\mathrm{R}\,. \tag{3.5}$$

A convenient way to mathematically describe the actions of optical elements on Gaussian beams within the paraxial approximation is ray transfer matrix analysis. A (thin) lens of focal length f is described by a matrix

$$\begin{bmatrix} A & B \\ C & D \end{bmatrix} = \begin{bmatrix} 1 & 0 \\ -1/f & 1 \end{bmatrix} \tag{3.6}$$

and acts on the complex beam parameter as

$$q' = \frac{Aq + B}{Cq + D}\,. \tag{3.7}$$

A free-space propagation by the distance d can readily be described by

$$\begin{bmatrix} A & B \\ C & D \end{bmatrix} = \begin{bmatrix} 1 & d \\ 0 & 1 \end{bmatrix} \tag{3.8}$$

transforming a the complex beam parameter q into

$$q' = \frac{Aq + B}{Cq + D} = q + d\,. \tag{3.9}$$

In principle, it is possible to select any of the two axes for the cylindrical telescope. It is however more practical to let it act on the horizontal axis, as centering of the cylindrical lenses with respect to the beam will require adjustments along the table surface instead of height adjustments. The compensation of astigmatism and ellipticity is perfect, if we make the beam widths in each axes equal for all positions z. To find focal lengths and lens positions that come closest to this, I fitted the data points of the vertical axis to the horizontal Gaussian beam as transformed by the telescope while taking the focal lengths and lens positions as fit parameters. The transformation of the horizontal Gaussian beam is computed by applying the transformation of the first lens by Equations 3.6 and 3.7 on the q-parameter at the position d_1 of this lens of focal length f_1. Equation 3.9 with $d = d_2 - d_1$ is then used to calculate the q-parameter immediately before the second lens of focal length f_2 and at position d_2. Subsequently, the transformation of the second lens is calculated. The resulting waist and waist position of the transformed horizontal axis are extracted according to Equation 3.5 from the imaginary and real parts of the resulting q, respectively. We obtain a model for the transformed horizontal axis as a function of lens focal lengths f_1 and f_2 and positions d_1 and d_2 using Equation 3.4 with the transformed waist w_0 and waist position z_0.

The fit of the horizontal component of the transformed Gaussian beam to the data of the vertical axis is shown in Figure 3.6 a). As can be seen, parameters for which the transformed horizontal axis (in red) comes very close to the vertical axis (in green) can be found.

In practise, the lens positions have restrictions given by the setup. In our case, the beam shaping telescope should be placed as early as possible, so that the laser beam passing through the following optics is already rectified. A range of 150 mm between the optical isolator and a mirror is available (cf. Figure 3.1), shown as a blue area in Figure 3.6. Corresponding bounds are given to the fit parameters. Initially, all four parameters f_1, f_2, d_1 and d_2 can be left as free fit parameters to get a sense of the required ratio f_2/f_1, the magnification of the telescope along the horizontal axis. It is useful to fix one of the focal lengths, in order to have less degrees of freedom for the fit. Since lenses are generally only available with certain focal lengths, a suitable and available combination is selected in a further step. The fit is repeated with correspondingly fixed focal lengths. In our case, a good combination is $f_1 = 150\,\mathrm{mm}$ and $f_2 = -100\,\mathrm{mm}$. The lens positions are computed to be $d_1 = (19.7 \pm 1.4)\,\mathrm{mm}$ and $d_2 = (64.1 \pm 1.5)\,\mathrm{mm}$. With these parameters, a suitable telescope can now be built.

3.4.4 Experimental realization of the cylindrical telescope

After centering the cylindrical lenses mounted in a cage system with respect to the beam, their relative distance is fine adjusted by minimizing the astigmatism. To this end, a regular lens of focal length f is placed into the beam behind the telescope close to the vertical focus position. This creates a smaller focus at a distance f for the vertical axis. A beam profiling camera on a rail is used to investigate the beam. The regular lens converts both axes to a Gaussian beam of smaller Rayleigh range, which makes the adjustment more practical because the camera does not have to be moved as far. The position of the vertical focus is most precisely found by determining two positions symmetrically around the focus at which the vertical waist is equal. The focus position will be exactly in between. By tuning the telescope's relative lens distance, the horizontal focal position is overlapped with the vertical focus, using the same technique to determine the focal position. Smallest possible changes in the relative lens distance have visible effects on the astigmatism. The adjustment criteria is thus very sensitive, and is not limiting the adjustment precision. Rather, precision is limited by the mechanical adjustability of the cage system.

Both the simulation and the experimental setup show a low sensitivity to changes of the absolute position of the telescope in the order of magnitude of the precision of using a measuring tape. Therefore, it does not need to be fine adjusted. This is to be expected since the beam does not change significantly on this scale, which is much smaller than the Rayleigh length.

The corrected laser mode is remeasured as described in Section 3.4.2. The result along with Gaussian beam fits is shown in Figure 3.6 b). The uncorrected beam is shown as a comparison. It can be seen that the telescope transforms the horizontal axis such that it matches the vertical axis quite well, however not as good as expected from the simulation (cf. Figure 3.6 a)). This can be explained by the finite precision of the telescope alignment, as well as the deviations of the laser mode from an ideal Gaussian beam. It is worth noting that the vertical axis has also changed marginally, contrary to expectations. This indicates slight changes in the laser mode over time, which could be due to changes in the thermal equilibrium within the laser crystal. The measurements were taken at an interval of 24 h. Nevertheless, it can be concluded that the astigmatism and the ellipticity could be significantly reduced to (155 ± 29) mm and 1.063 ± 0.013, respectively. This corresponds to a reduction of the astigmatism by 81 % and of the ellipticity 62 %. Thereby, an improvement of the coupling efficiency into a fiber is expected.

A suitable cylindrical telescope could also be found purely experimentally, without the need to measure and model the laser mode. The prerequisite is the availability of sufficient cylindrical lenses of different focal lengths. One can start with a pair of cylindrical lenses and place them apart by about $f_1 + f_2$, to then minimize the astigmatism as earlier described. The astigmatism will be corrected, however the ellipticity will have been changed, but *a priori* not such that the beam is circular. This can be iterated with a varying ratio f_2/f_1 which changes the ellipticity, until a telescope is found that can both compensate astigmatism and ellipticity. The ellipticity can easily be measured by a beam profiling camera placed in the far field. If the telescope is positioned at one of the waist positions, the required focal length ratio is equal to the measured ellipticity, making this a particularly convenient configuration.

3.4.5 Fiber coupling and collimation

The efforts of astigmatism and ellipticity compensation allow higher fiber coupling efficiencies. In order to create a high overlap of the mode impinging on the fiber with the guided mode, a focus with matching waist has to be created at the fiber's input. This is the purpose of a fiber collimator consisting of a lens which is precisely positioned with respect to the fiber end.

The focal length of the fiber coupler lens has to be chosen to match the beam width and the fiber mode width. The lens can be translated to adjust the position of the beam waist to the input facet of the fiber. The ideal collimator depends on the position within the beam, since the beam width itself is position dependent. I used a fiber coupler[26] giving a collimated beam with a waist of 691 µm and placed it at $z = 1\,700\,\mathrm{mm}$. As can be seen from Figure 3.6 b), this matches the average beam width of the vertical and horizontal axis at this position. The collimated beam waist of the fiber coupler was measured by taking a near field image as in Figure 3.5 of a collimated beam coupled out using this collimator. A Gaussian fit then gives the specific value.

The light is coupled into a conventional polarization-maintaining single mode fiber.[27] I achieved a maximal fiber coupling efficiency of 86.3 % at an alignment optical power of 100 mW. Compared to the efficiency of 78 % without the cylindrical telescope this is an enhancement of available optical power behind the fiber of 10 %. Increasing the optical power to 5 W at the fiber input slightly reduces the fiber coupling efficiency to 84.7 %.

3.5 Summary and conclusion

I conclude that the presented method of measuring and modelling the laser mode is well suited to correct astigmatism and ellipticity of a laser beam. The fiber coupling efficiency into a conventional fiber could be significantly increased using a cylindrical beam shaping telescope. I furthermore improved the optical power handling of the analog intensity control by replacing an EOM by an AOM. To minimize losses of optical power, I used a configuration using the 0^{th} diffraction order where the 1^{st} order is ‘recycled’ for the optical polarization gradient setup. The comparable feedback bandwidth and intensity noise suppression to the previous setup demonstrates an equivalent suitability. A PCF was employed to overcome the stimulated Brillouin scattering limit of conventional fibers. I measured the return loss of the PCF being comparable to conventional fibers using a self-built fiber coupler allowing high coupling efficiencies. A further improvement of the 71 % PCF coupling efficiency is expected with more careful alignment. Utilizing AR coated fiber facets is expected to give around 7 % more light. Overall, up to 3 W could be guided to the HDT setup on the experiment table. This allows twofold horizontal lattice beam intensities corresponding to an increase of the possible trap depth up to 1.5 mK. I expect a considerably reduced hopping rate along horizontal directions during the imaging. Generally, higher available optical powers could also be utilized to create larger dipole traps, thereby reducing gradients of light shifts allowing optimal imaging parameters over larger areas of the FOV.

---

[26] 60FC-4-M12-33 fiber collimator from Schäfter+Kirchhoff.

[27] A 1 m long uncoated PM780-HP from Thorlabs.

CHAPTER 4

Three-dimensional imaging of single atoms by point-spread-function engineering

In this chapter I present a novel extension of a so-called quantum gas microscope, giving the possibility to extract the three-dimensional positions of individual atoms trapped in a three-dimensional optical lattice from two-dimensional images. To this end, the point spread function (PSF) of the microscope is phase-engineered into a double-helix point spread function (DH-PSF) using a spatial light modulator (SLM) in the pupil plane. Thereby, a single atom is imaged as two separate peaks whose relative angle depends on the axial position of the atom. The depth information for each atom can then be obtained from the measured angles.

The near unity single atom detection efficiency of dense ensembles through quantum gas microscopes revolutionized detection and control of lattice quantum gases, i.e. indistinguishable atoms arranged in optical lattices [27, 47, 48]. The individual atoms are detected optically by observing fluorescence photons through a microscope. Objective lenses with high numerical aperture (NA) are used to achieve the required resolution in the order of the wavelength. This experimental platform allows the realization of many-body systems in which fundamental effects can be studied in a fully controlled way with good access to observables. Our two-dimensional discrete quantum simulator (DQSIM) described in Chapter 2 can be used, for example, to perform two-dimensional discrete-time quantum walks [20] or interference experiments of multiple indistinguishable particles [22]. Previous quantum gas microscopes do not have direct optical access to the axial position of individual atoms beyond the defocus. As we will see, the axial resolution in such systems is limited. However, it is of interest to have not only transverse but also axial single-site resolution available.

For instance, axial single-site resolution allows post-selection of single vertical lattice planes. This is useful because common methods for plane preparation involve a trade-off between survival in the target plane and fidelity of selection. I will discuss this in Section 4.1 using our experiment as an example.

High axial resolution over a large depth of field (DOF), as enabled by the DH-PSF, also opens up the extension of quantum simulation into three dimensions. This is already of interest because of the thereby scaling number of available qubits [46]. After an introduction of the PSF and the resolution limit in Section 4.2, I present in Section 4.3 existing methods of three-dimensional imaging with special attention to imaging single cold atoms. However, these techniques are of equally great interest beyond physics. In particular, the rotating PSF emerges from the research field of super-resolved fluorescence microscopy of biological systems. It has been an active research topic since the demonstration of three-dimensional super-resolution of single molecules in 2009 [74]. For quantum gas microscopes like ours, modifying the PSF into a rotating PSF will prove to be a well-suited approach. I therefore describe this concept in detail in Section 4.4.

Finally, I present the experimental realization and the evaluation of DH-PSF measurements in Sections 4.5 and 4.6 respectively. These confirm the extension of single-site resolution of individual atoms to the axial dimension. Section 4.7 draws a conclusion and discusses possible improvements.

4.1 Preparing atoms in a plane

To measure the interference of multiple particles, the ensemble of atoms must be confined to a single vertical layer of the optical lattice. The state-dependent transport of our experiment operates in the two horizontal dimensions. The optical lattice is first probabilistically loaded from the magneto-optical trap (MOT) as described in Section 2.1. A release-retrap technique can help to compress the atoms along the vertical as much as possible, so that a higher fill factor in a thin section of the lattice can be achieved [114]. Vertical microwave spectroscopy finally allows to precisely control in which vertical planes atoms remain and allows the creation of a single vertical plane. The preparation of an atomic ensemble in a single plane of an optical lattice is a common challenge of experiments exploring two-dimensional systems [37, 38, 47, 48, 84, 115–118]. Commonly used is a vertical position-dependent Zeeman shift induced by a magnetic field gradient. This then allows thin volumes around the isosurfaces of the magnetic field to be addressed spectroscopically.

In our experiment, instead of the Zeeman shift, an AC Stark shift is generated by a gradient of polarization. Due to the analogy, this can be considered as an optically generated artificial magnetic field. This is described in detail in Reference [84]. The polarization gradient is obtained by the interference of two beams of orthogonal circular polarization at 866 nm entering the atomic cloud at a relative angle to each other. Along the direction spanned by the angle, which coincides with the vertical axis of the optical lattice, the polarization ellipticity of the light field is sinusoidally modulated just as in the analogous polarization gradient cooling (PGC) configuration [90]. The modulation of the polarization leads to a modulated differential light shift between $|\uparrow\rangle$ and $|\downarrow\rangle$. The theoretical spatial profile is shown in Figure 4.1. As can be seen, the isosurface of vanishing light shifts is perfectly flat. The horizontal capture range of the central vertical planes is larger than the horizontal extent of the atomic cloud. If all atoms are prepared in the $|\uparrow\rangle$ state of the effective two-level system (cf. Section 2.1), the atoms in the target plane can be transferred to the $|\downarrow\rangle$ state by applying a microwave radiation π-pulse. The spatially modulated resonance condition allows to addresses only the target plane, provided that the spectroscopic resolution is large enough. Subsequently, the atoms remaining in $|\uparrow\rangle$ of the undesired planes are resonantly heated out of the dipole trap.

Gaining information about the vertical position of atoms directly from fluorescence images is a valuable tool in this context. On the one hand, it relaxes the requirements on the strength and stability of the gradient used for spectroscopic resolution of adjacent planes. Even if atoms are not located in the target plane with high fidelity after plane selection, these atoms can always be assigned to a vertical plane in a post-selection based on the acquired images. In fact, the vertical selection demonstrated in Reference [84] was limited to a spatial width of $\sigma_z = (2.0 \pm 0.2)\,\mathrm{d}z_{\mathrm{vert}}$, where $\mathrm{d}z_{\mathrm{vert}} = 532\,\mathrm{nm}$ is the vertical lattice spacing. By modifying the microwave pulse shape and using a higher optical power of the polarization gradient, a resolution of a single vertical plane can be expected. Yet, about 2 % of the atoms are still expected to remain in the undesired planes [84]. These could be deterministically sorted out by

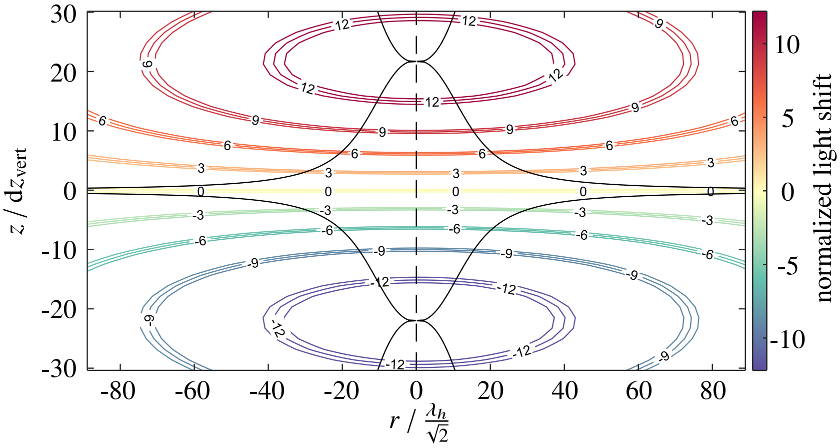

Figure 4.1: Differential light shift between $|\uparrow\rangle$ and $|\downarrow\rangle$ normalized to the light shift between adjacent planes at the center. The vertical position z and horizontal position $r = \sqrt{x^2 + y^2}$ are given in units of the vertical and horizontal lattice constants $\mathrm{d}z_{\mathrm{vert}} = 532\,\mathrm{nm}$ and $\lambda_h/\sqrt{2} = 612\,\mathrm{nm}$ respectively. Isolines of the color-coded light shift corresponding to certain vertical lattice planes given by the numbers on the lines are shown. Each isoline is enclosed by two lines corresponding to $\pm 0.2\,\mathrm{d}z_{\mathrm{vert}}$ of the lattice plane in question. The black lines indicate the horizontal capture range, which is defined as the position where the light shift has changed by 20 % of the light shift at the center. The dashed black line indicates the center position of the vertical dipole trap. Taken and modified from Reference [84].

the optically resolved vertical localization. Moreover, there is generally a trade-off between the fidelity of single plane selection and the survival in the target plane. Reducing the demands of the preparation fidelity can be compensated for by the available post-selection of planes, enabling higher survival of the target plane. On the other hand, the optical resolution of the vertical position is also an ideal tool for more precise adjustment of any vertical plane selection technique. In our case, for instance, a vertical drift of the polarization gradient could be detected and thereby corrected.

4.2 Point spread function and the resolution limit

An imaging system is described by its PSF, which determines what the image produced by the system looks like. In particular, the PSF determines the information that can be obtained from an image of the object. It is therefore useful to know the PSF exactly or even to be able to change it. As we shall later see, three-dimensional images can be reconstructed using certain PSFs. Therefore, in this section I introduce the concept of PSF, as well as its relation to the resolution limit.

4.2.1 Point spread function

The PSF of an imaging system is the image of an ideal point source. The concept is discussed in detail in Reference [119], which I also refer to for what follows. Figure 4.2 show exemplarily the PSF of our microscope at NA = 0.92. If the PSF is invariant with respect to the position of the point source, the image i of an object can be obtained by convolving the actual object o with the PSF

$$i = o * \mathrm{PSF}\,. \tag{4.1}$$

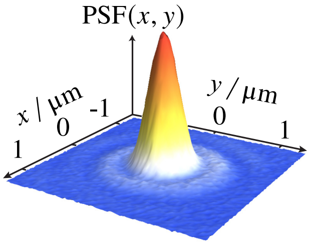

Figure 4.2: Measured PSF of our microscope at NA = 0.92 given in object space coordinates. Taken and modified from Reference [59].

Here, the PSF, as well as the image and object are in general functions of the three-dimensional space coordinates $\boldsymbol{x}$. For a system that maps from an object plane to an image plane, these are often thought as functions of the plane coordinates (x, y) only. The PSF fully describes the response of an imaging system. Note that we can use the same coordinates in object and image space by ignoring magnification and image inversion for the sake of simplicity.

One further abstraction of the optical system turns out to be very helpful in order not to have to consider each optical element separately to explain the shape of a system's PSF. In general, an optical system can contain several different apertures, but these can be summarized by a single effective aperture, the aperture stop, which most severely restricts the bundle of rays passing through the system. Let us then define the entrance pupil as the image of the aperture stop as seen from an axial point in object space through the optical elements in front of the aperture stop. Accordingly, the exit pupil is the image of the aperture stop as seen from the image plane. It is then sufficient to describe the propagation from the entrance pupil to the exit pupil by geometrical optics, and to consider the diffraction-causing finite aperture only at the exit pupil. Similar for the conjugate object and image planes, the conjugate entrance and exit pupils[1] can also be expressed using same coordinates, which is why they are often referred to as the pupil for short. The pupil is described by the pupil function $P(u, v)$, which describes the transmission in the pupil plane. In an aberration-free system, the amplitude PSF is then the Fraunhofer diffraction pattern of the pupil, which can be described by a Fourier transform (see Appendix A.2). By forming the magnitude square, the intensity PSF is obtained. This remarkably simple relationship is the fundamental rationale of Fourier optics. A circular aperture yields, for example, the well-known Airy disk as PSF, which is very close to the PSF of Figure 4.2.

4.2.2 The fundamental resolution limit

The three-dimensional (or when restricted to a plane object and image space two-dimensional) Fourier transform of the PSF is called optical transfer function (OTF). The modulation transfer function (MTF) is obtained by taking the absolute value. The MTF describes how different spatial frequencies are processed by the optical system. The finite aperture of an optical system acts as a low pass filter for the spatial frequencies with the Abbe cut-off frequency

$$k_{\text{Abbe}} = 1/r_{\text{Abbe}}\,, \qquad \text{where} \qquad r_{\text{Abbe}} = \frac{\lambda}{2\text{NA}} \tag{4.2}$$

---

[1] According to the definitions, the exit pupil is the geometric image of the entrance pupil with respect to the complete optical system.

is the Abbe radius, with the wavelength λ and the NA defined in Section 2.2. An image is therefore always blurred to a certain degree.

The sharpest PSF is realized by a diffraction-limited system, which for a circular aperture is the Airy disk. For such a system, the Abbe radius gives the optical resolution, or diffraction limit[2] [120]. For our microscope objective that collects fluorescence light at $\lambda_{\mathrm{D2}} = 852\,\mathrm{nm}$, the maximal NA of 0.92, for example, gives the Abbe radius of 463 nm, which is lower than the horizontal lattice spacing $\lambda_{\mathrm{h}}/\sqrt{2} = 612\,\mathrm{nm}$. The horizontal lattice can thus be optically resolved. At the intermediate NA of 0.6, an Abbe radius is 710 nm.

For objects that are distant from the focal plane, the PSF becomes blurred, the so-called defocus aberration. To a certain extent, this allows conclusions to be drawn about the axial position. Similar to the Abbe radius, the sharpness of the PSF along the optical axis can be characterized by the DOF, which depends on the NA as

$$\mathrm{DOF} = \frac{\lambda}{2\mathrm{NA}^2}\,. \tag{4.3}$$

For our microscope, the maximal NA yields DOF = 503 nm. We will come back to what this means for axial resolution.

It should be noted, however, that employing the knowledge of the physical system, such as the shape of the PSF or the structure of the imaged object (e.g. atoms in a lattice), the optical resolution limit can be exceeded to a certain extent. Such methods are known under the term super-resolution, and are developed and applied in particular in the field of microscopy of biological systems, where the non-linear response to excitations, or the temporal behavior of the employed fluorophores is used to ensure that there are only isolated emitters per image [122–124]. Exploiting the knowledge of the PSF, the emitter position can then be super-resolved by deconvolution of the image. The diffraction limit could also be overcome for three-dimensional localization of single molecules [74, 78, 79]. Super-resolution methods also have application in the context of microscopy of single atoms in optical lattices [39, 125]. The fundamental resolution limit for an unbiased position estimator is given by the so-called Cramér-Rao lower bound (CRLB), the inverse of the Fisher information matrix [126–128]. This limit can be approached by knowing the imaging system response and all physical noise properties.

4.2.3 Diffraction-limited systems and aberrations

Following Reference [119] again, we can further define the previously mentioned concept of a diffraction-limited system. Its defining property is that an incoming diverging spherical wave (originating from an ideal point source) is transformed by the system into a converging spherical wave at the exit pupil, converging towards an ideal point in the image plane.[3] In real imaging systems, this is at best the case within limited regions of the object or image space. The system can then be considered diffraction limited over these regions. If the wavefront emerging from the exit pupil deviates from the ideal spherical wave, such a system is said to have aberrations.

---

[2] Ernst Abbe derived this in 1873 within his theory of image formation in microscopes [120]. A similar expression for the resolution limit is provided by the heuristic criterion named after Lord Rayleigh, according to which two adjacent points can just be resolved if the first minimum of one Airy disk coincides with the maximum of the other [121]. The Airy radius $r_{\mathrm{Airy}} = 1.22 \cdot \lambda/(2\mathrm{NA})$ i.e., the first zero of the Airy disk is thus also the resolution limit defined in this way.

[3] The position of this ideal image point is related to the position of the original object point only by a scaling factor (the magnification), which is the same for all points in the image field, and possibly an inversion.

Concretely, such wavefront errors can be described by imagining that a perfect spherical wave enters the pupil, but that the wavefront gets distorted there. With the effective optical path-length error $W(u, v)$, we can define the generalized pupil function

$$\mathcal{P}(u, v) = P(u, v)\ \exp\left(\mathrm{i}kW(u, v)\right)\ , \tag{4.4}$$

with $k = 2\pi/\lambda$. The PSF of an aberrated system is determined by the Fraunhofer diffraction pattern of the aperture, as in the aberration-free case (see Section 4.2.1), but this time with the amplitude transmittance $\mathcal{P}(u, v)$. Specifically, it is given by

$$\mathrm{PSF}(x, y) = \left|\mathcal{F}\left\{E_0\,\mathcal{P}(u, v)\right\}(\kappa_u, \kappa_v)\right|^2\ , \tag{4.5}$$

where E_0 is electric field in the pupil plane and the Fourier transform is evaluated at the spatial frequencies $\kappa_u = kx/f$ and $\kappa_v = ky/f$. Here, f is the distance from the exit pupil to the image plane provided that (u, v) are the coordinates in the exit pupil and (x, y) in the image plane. A useful basis for describing arbitrary aberrations in a system with circular aperture are the orthogonal Zernike polynomials defined on the unit disk [129] (see Appendix C.3). The lower-order polynomials correspond to the typically most pronounced aberrations such as the tilt, astigmatism, defocus, trefoil, coma, or also spherical aberrations.

Aberrations generally lead to a (not necessarily axially symmetric) broadening of the Airy disk. This is usually undesirable due to the resulting lower achievable resolution. The combined effect of diffraction and aberration is fully described by the PSF. The high-NA objective lens used in our experiment was previously examined with respect to aberrations, as reported in Reference [59]. The measured PSF at different positions in the object plane using a fiber tip with a diameter of approximately 100 nm, was then fitted with the PSF calculated from Equation 4.5 using the expansion in the lowest-order Zernike polynomials by means of non-linear least squares minimization. The Strehl ratio was used to quantify the aggregate aberrations[4], and is defined as the ratio of the maximum of the PSF and the maximum of the corresponding ideal Airy disk. According to the Maréchal criterion, an optical system with a Strehl ratio ≥ 80 % can be considered diffraction limited [130]. It could be concluded that the field of view, in which this is fulfilled, has a diameter of 76 µm. The further away from the optical axis, the stronger the aberrations, which is the result of both the measurement and the theoretical prediction based on the objective lens design.

4.3 Methods of three-dimensional localization

The ability to resolve minute structures has rapidly made optical microscopy an important pillar of the natural sciences ever since its emergence at the beginning of the 17th century [131]. Nonetheless, major advances are still being made centuries later. In 1953, for example, Frits Zernike was awarded the Nobel Prize in Physics for the development of the phase contrast method, with which phase shifts of light passing through an object can be observed as intensity modulation [129]. Super-resolution microscopy techniques, mentioned in Section 4.2.2, have overcome the Abbe resolution limit and enabled resolutions at the molecular level [122], for which the 2014 Nobel Prize in Chemistry was awarded. Remarkably, such methods combined with PSF engineering have recently led to three-dimensional super-resolved

---

[4] A relationship between the Strehl ratio SR and the root mean square (RMS) deviation of the wavefront is provided by the Maréchal approximation $\mathrm{SR} \approx 1 - \left(kW_{\mathrm{rms}}\right)^2$ [130].

microscopy of biological structures [74, 78, 79].

In this section I present common methods of three-dimensional imaging of single fluorescing emitters which, for instance, are reviewed in References [82, 83, 123, 132]. The mentioned reviews arose from fluorescence microscopy of molecules, however, most results are applicable to the largely equivalent fluorescence microscopy of single atoms. I therefore also discuss, in particular, the applicability of each method to our experiment. The methods of three-dimensional imaging can be divided into those in which sequential images of the object are acquired while scanning the focus, also called tomography, and those in which the three-dimensional information is obtained in a single image. These rely on simultaneously taking multiple images of the same object through different beam paths as in multifocal plane microscopy, on recording the full field information as in light field microscopy, or on engineering the three-dimensional shape of the PSF. Although the microscopy methods for our application in imaging cold atoms are not different in concept from those used in biology, unlike the other methods, the engineering of PSF has not yet been used with the goal of acquiring the three-dimensional positional information of individual atoms.

In a conventional imaging system, the lateral position of an emitter can be readily extracted from the location of its image. The axial position can be retrieved from differences in the shape of its image at different distances from the focus, for instance, the defocus. However, as the DOF Equation 4.3 scales as $1/\mathrm{NA}^2$, the standard PSF decays slower in the axial direction as in the lateral direction, where the width scales with $1/\mathrm{NA}$ (cf. Equation 4.2). Accordingly, the axial in-focus localization precision is worse, and the smaller the NA, the more so. Moreover, in contrast to lateral localization, several axially distant emitters cannot be localized from a single image, since these emitters have to be located within the DOF to remain resolvable. Methods of three-dimensional imaging must accordingly increase the axial resolution ideally also in the focus, and maintain it over as large an axial distance as possible.

4.3.1 Tomography

The idea of tomography is to sequentially create images of the same object while scanning the focus over a desired range. Emitters at different axial positions thus appear sharp in different images. Subsequently, the three-dimensional position can be reconstructed from the set of images. To change the focus, either the object itself, the camera, or the objective lens can be translated.

The method has been used to localize atoms in three-dimensional lattices [46] as well as arrays of optical tweezers [60], where in both cases the vertical plane separations are larger than in our case. Reference [61] reports a quantum gas microscope whose piezo-steered objective lens of $\mathrm{NA} = 0.69$ allows tomography of single atoms in a three-dimensional optical lattice with the same vertical lattice spacing as ours. Figure 4.3 a) shows images taken at different focus settings. A fit of the measured peak intensity as a function of the focus setting can then be employed to calculate the vertical position. Given the finite lifetime of the atoms in the dipole trap, the need for multiple shots for this comparatively simple method is a major drawback. Our microscope cannot be equipped with a piezo control of the objective lens anyway, as it is in-vacuo. The displacement of the atoms is not easily feasible, nor can the camera be moved by centimeters[5] within milliseconds.

---

[5] A displacement in image space corresponds to a displacement in object space multiplied by the square of the magnification.

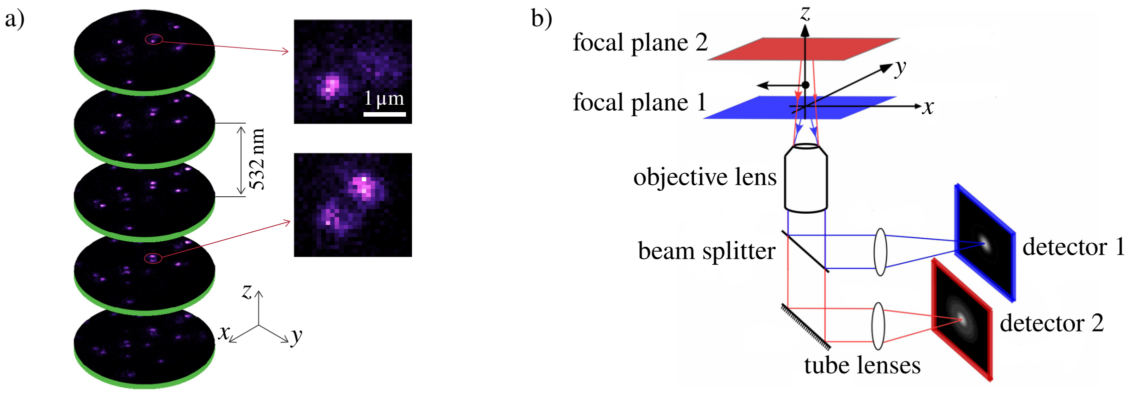

Figure 4.3: a) Fluorescence images of single atoms in an optical lattice taken with different focal plane positions. The focal plane is changed by a piezo-controlled shift of the objective lens position along z. The enlarged image sections shows two atoms from which the frame-dependent defocus can be discerned. Modified taken from Reference [61]. b) Schematic of multifocal plane microscope configuration using two different focal planes. The fluorescence light is split into two paths by a beam splitter, each of which have a detector placed at a different total distance from the objective lens. The two detectors thus operate with distinct focal planes. fluorescence signal is detected from only one side of the sample. Taken and modified from Reference [133].

4.3.2 Multifocal plane microscopy

In multifocal plane microscopy, the same principle is used, except that images with different focus settings are acquired simultaneously in different detectors or separate areas of the same detector instead of being taken temporally separated. This significantly reduces the recording time. The number of partial images of different foci is left to choice, although most microscopes work with two. Figure 4.3 b) shows a possible configuration. Another architecture sometimes used are two objective lenses facing each other around the object space (4π geometry), each with a camera, doubling the amount of collected light.

However, multifocal plane microscopy comes at the cost of a significant increase in instrumental complexity. Moreover, the fluorescence imaging of atoms is a photon-limited process. I.e., for the same signal-to-noise ratio (SNR), more photons must be scattered at the atoms due to the splitting of the light into the different images, increasing the probability of atom loss and hopping. This is probably why multifocal plane microscopy has not yet been used to image cold atoms.

4.3.3 Light field microscopy

Three-dimensional information can be captured with a single image in a light field microscope. An overview of the technique is given in Reference [134]. A micro lens array partitions a sensor array, with each micro lens covering an area of several pixels, just as in a Shack-Hartmann wavefront sensor. This allows to measure not only the intensity, but also the parallax of the rays originating from a point in object space, providing information about the field wavefront. The field gradient depends on the axial position of an emitter and therefore allows conclusions to be drawn about the axial position. The micro lens array is typically placed in an image plane where it samples the spatial domain, generally resulting in a large pixel size. Reference [69] reporting the three-dimensional imaging of a rubidium MOT is an example of such a configuration. The need for multiple pixels per microlens results in a loss of lateral resolution, which is not an option for our application.

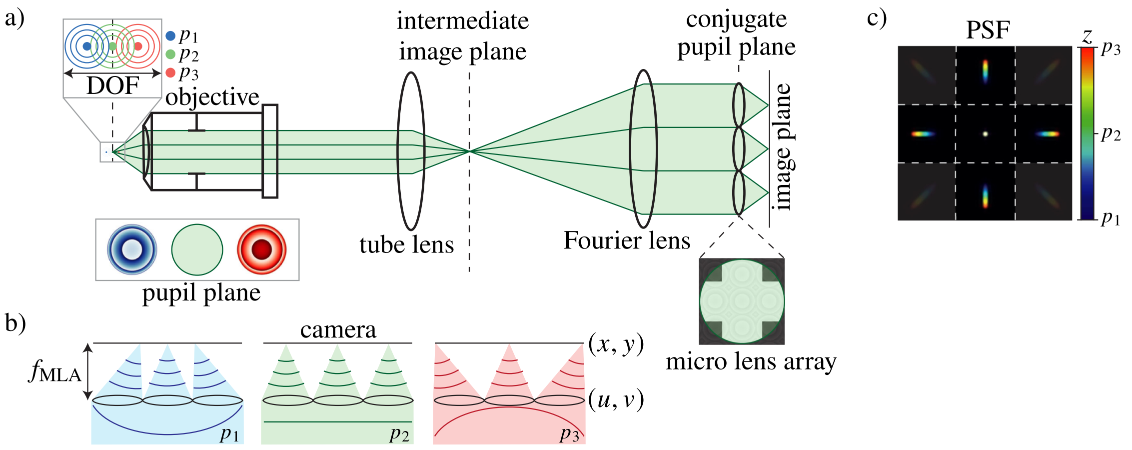

Figure 4.4: a) Schematic of a Fourier light field microscope. A micro lens array is positioned in a conjugate pupil plane. b) The micro lens array samples spatial and angular information of the incident wavefront. Depending on the wavefront gradient on a certain microlens, the corresponding image is shifted. Thereby, two emitters located below (blue) and above (red) the focal plane are imaged at different positions in each perspective view due to their curved wavefront in the pupil plane. c) Simulated point spread functions as a function of the emitters axial z-position. Taken and modified from Reference [135].

However, the micro lens array can also be placed in a plane conjugate to the pupil of the microscope objective, a configuration also known as Fourier light field microscopy. It is depicted in Figure 4.4. Each microlens produces a focused image that is shifted according to the local average wavefront gradient. Thus, axially displaced emitters are imaged at different positions in each subframe. Although Fourier light field microscopy provides higher spatial resolution than the traditional configuration, it is at the expense of field of view (FOV) and DOF. It should be noted that this method could be readily implemented by programming an array of holographic lenses on the SLM in the setup present in this work. Reference [135] reports on using the technique achieving three-dimensional super-resolution of single molecules over a DOF of 6 µm.

4.3.4 PSF engineering

Based on the observation that axially dependent aberrations do carry information about the axial position, it is conceivable to introduce such aberrations in a controlled manner into a conventional microscope. In fact, when observing atoms in our optical lattice, those that are out of focus not only appear blurred, but their measured PSF is deformed differently due to residual aberrations depending on which side of the focus they are [84]. The PSF can be modified by modulation of the amplitude and/or phase of the fluorescence light field. The three-dimensional PSF is designed so that the axial position of an emitter can be unambiguously established from its measured two-dimensional intensity distribution.

The main advantage of PSF engineering is that quasi-volumetric images are obtained from a single shot. The choice of PSF modifications is inherently broad. References [83, 132] review common choices. A straightforward PSF modification consists of introducing astigmatism, creating elongated peaks along a direction depending on the emitters side to the focal plane. However, although this increases axial localization precision within the DOF, it does not extend the DOF and deteriorates lateral resolution. PSFs which consist of azimuthally structured lateral intensity distribution that rotate along the axial dimension can be used to achieve both higher axial resolution and increased DOF while maintaining high lateral resolution. As we will see, a PSF in the form of a double helix is particularly suitable and can be created by phase modulation alone in the pupil plane.

Because of these advantages, we choose the rotating PSF technique for our experiment, which I therefore discuss in detail in Section 4.4 hereafter.

4.4 Introduction to the rotating PSF

In conventional imaging systems, single atoms in fluorescence images appear as Airy disks in the absence of aberrations, as we saw in Section 4.2.1. The position along the line of sight can only be determined by the defocus. As we will see, this method suffers from a low resolution. For example, the vertical lattice structure can be resolved only for very high NAs which are difficult to reach and also severely limit the DOF. We will also see that the defocus is not suitable to determine on which side an atom is located relative to the focal plane. The key idea is to break the axial symmetry of the PSF, and encode the axial position into the rotation angle of the modified PSF. To determine the three-dimensional position of an atom, the axial position must then be determined from the rotation angle of the measured PSF in addition to determining the lateral position.

The rotating PSF was first proposed in 1996 [71], further developed in Piestun's group [72, 73, 136], and subsequently realized in fluorescence microscopy for biological systems [75, 76, 79, 81, 137, 138]. Also contributing here was the group of Moerner [74, 77, 80, 132], recognized with the 2014 Nobel Prize in Chemistry for the development of super-resolution fluorescence microscopy.

4.4.1 Construction from Laguerre-Gauss modes

As shown in Reference [71], a rotating PSF in the paraxial approximation can be constructed from Laguerre-Gauss (LG) modes. To understand the necessary conditions and to get analytical expressions for the expected rotation angles, I briefly introduce the LG modes.

The LG modes form a complete orthogonal[6] (basis) set of solutions of the paraxial Helmholtz equation (see Appendix A.1 for details) in cylindrical coordinates [109]. The LG transverse mode of order (l, p) is given by

$$u_{lp} = C_{lp} \frac{w_0}{w(z)} \left(\frac{r\sqrt{2}}{w(z)} \right)^{|l|} \exp\left(-\frac{r^2}{w^2(z)} \right) L_p^{|l|} \left(\frac{2r^2}{w^2(z)} \right) \exp\left(ik \frac{r^2}{2R(z)} \right) \exp\left(il\phi - i\psi_{lp}(z) \right) , \quad (4.6)$$

---

[6] The orthogonality relation is given by $\langle l', p' | l, p \rangle = \delta_{ll'} \delta_{pp'}$, with the scalar product defined by $\langle \Psi | \Phi \rangle = \int_0^{2\pi} \mathrm{d}\phi \int_0^\infty \mathrm{d}r r\, \Psi^*(\boldsymbol{x}) \Phi(\boldsymbol{x})$. The notation is explained in Appendix B.1.

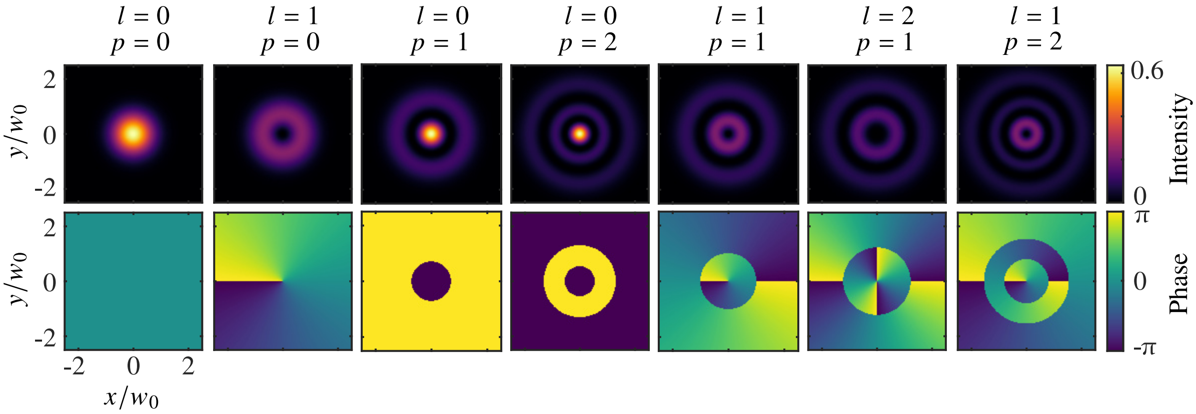

Figure 4.5: The first seven Laguerre-Gauss modes at $z = 0$. The upper row shows the intensity $|u_{lp}|^2$, the lower row the phase $\arg(u_{lp})$. The fundamental mode u_{00} corresponds to a Gaussian beam. The azimuthal mode index l determines the number and direction of azimuthal phase windings, while the radial mode index p defines the number of radial phase discontinuities. The intensity at phase discontinuities and singularities is zero, giving rise to a ring-like intensity profile.

with

a normalization factor[7] $$C_{lp} = \sqrt{\frac{2p!}{\pi(p+|l|)!}}\,, \tag{4.7}$$

the beam waist $$w_0\,,$$

the beam radius $$w(z) = w_0\sqrt{1+(z/z_\mathrm{R})^2}\,, \tag{4.8}$$

the Rayleigh distance $$z_\mathrm{R} = \pi w_0^2/\lambda\,, \tag{4.9}$$

the phase curvature radius $$R(z) = z\left(1+(z_\mathrm{R}/z)^2\right)\,, \tag{4.10}$$

the Gouy phase $$\psi_{lp}(z) = (2p+|l|+1)\arctan(z/z_\mathrm{R})\,, \tag{4.11}$$

and the generalized Laguerre polynomials $$L_p^l\,.$$

Figure 4.5 shows the intensity and phase profiles at the waist $z = 0$ of the seven first LG modes. The azimuthal mode number $l \in \mathbb{Z}$ gives the number and direction of phase windings $\mathrm{e}^{\mathrm{i}l\phi}$ around the optical axis, giving rise for $l \neq 0$ to an optical vortex of topological charge l. In addition to the spin angular momentum associated with polarization, a photon in this mode will carry an orbital angular momentum $\hbar l$ [139, 140]. Interestingly, beyond the paraxial approximation, it is no longer true that spin and orbital angular momentum are decoupled, and spin-orbit coupling occurs [141, 142]. The radial mode number $p \in \mathbb{N}$ determines by the zero crossings of the Laguerre polynomials the number p and position of radial phase discontinuities. The intensity at phase discontinuities must be zero, which is manifested by the ring-like structure of the intensity profile with p rings of vanishing intensity. Moreover, for $l \neq 0$ the intensity on the optical axis is zero because of the phase singularities located there. The LG modes, just

---

[7] This normalization constant is chosen such that $\int_0^{2\pi}\mathrm{d}\phi\int_0^\infty r\mathrm{d}r|u_{lp}(r,\phi,z)|^2 = 1$. The deviating normalization constant reported in Reference [71] is chosen to yield $\max\left(|u_{lp}(r,\phi,z)|^2\right) = 1$.

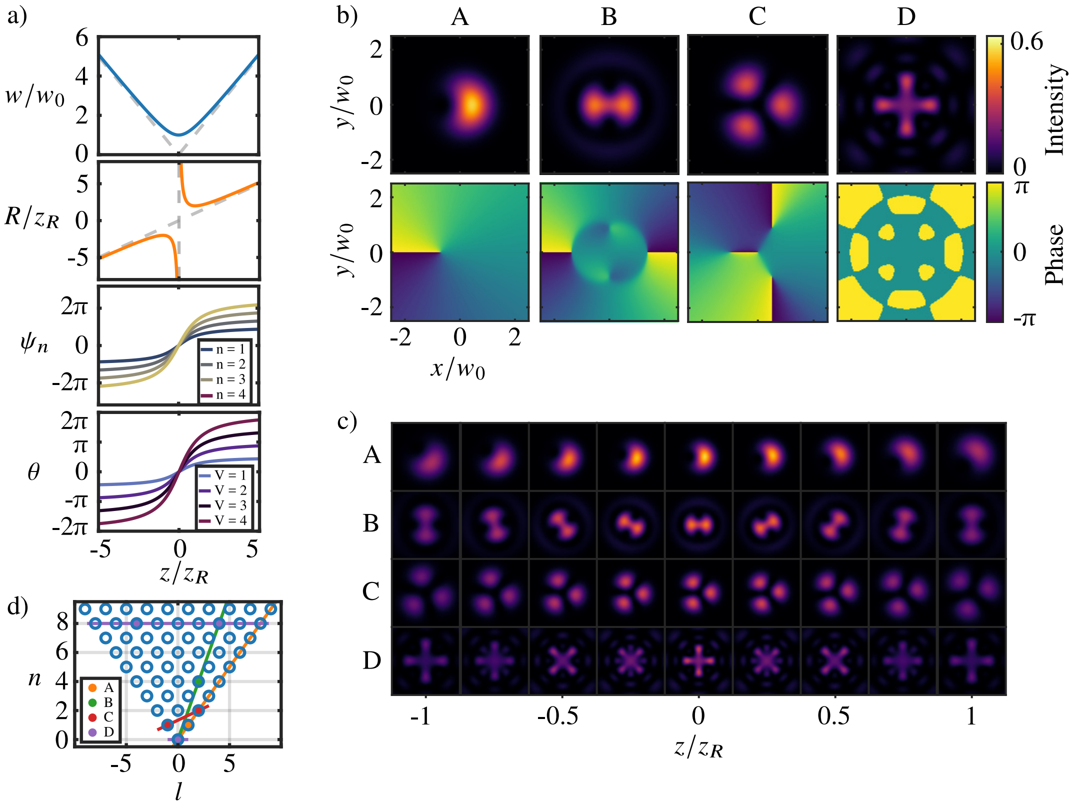

Figure 4.6: a) Plots of the beam radius (Equation 4.8), phase curvature radius (Equation 4.10), Gouy phase for various combined mode indices $n = 2p + |l|$ (Equation 4.11), and rotation angle for various constants $V = \Delta n/\Delta l$ (Equation 4.16) as a function of z-position. The asymptotes are indicated by gray dashed lines. b) Examples of LG mode superpositions at the waist $z = 0$. The Example A shows the superposition of the modes u_{00} and u_{10}, Example B of the modes u_{00} and u_{21}, Example C of the modes u_{-10} and u_{20} and Example D of the modes u_{00}, u_{42} and u_{-42}, each with equal coefficients preserving normalization. The upper row shows the intensity profile $|u_{lp}|^2$, the lower row the corresponding phase profile $\arg(u_{lp})$. c) Intensity profiles at different z-positions within the Rayleigh range for the four examples. The color scale is the same throughout. d) LG modal plane with the examples marked. Examples A-C lie on straight lines, Example D lies on two lines parallel to the l-axis.

like their fundamental mode (a Gaussian beam), have a point of smallest radial extent at $z = 0$ and a Gaussian envelope that diverges according to $w(z)$ (cf. equations 4.6 and 4.8) with increasing distance z on the scale of the Rayleigh length z_R (Equation 4.9). The LG modes have apart from the azimuthal phase windings a plane phase front in the waist as well as at infinity. In between, however, they are curved because of the non-constant amplitude distribution at the waist as opposed to plane waves, with the maximum curvature being at the Rayleigh distance. This phase curvature is given by the reciprocal of the phase curvature radius (Equation 4.10). A LG mode also undergoes a Gouy phase shift of $2p + |l| + 1$ times the Gouy phase shift $-\pi$ of a Gaussian beam when passing through the focus from $-\infty \longrightarrow +\infty$ (cf. Equation 4.11). These z dependencies are shown in Figure 4.6 a).

Each LG mode is stationary in z (except for the scaling with $w(z)$ and the laterally constant Gouy phase) and an eigenmode of rotation around the z-axis.[8] In particular, this means that the intensity distribution $|u_{lp}|^2$ is axially symmetrical and stationary. To break the axial symmetry and stationarity, two or more LG modes can be superimposed. The intensity of a superposition of two modes can then be expressed by

$$I \propto |u_{lp} + u_{l'p'}|^2 = |u_{lp}|^2 + |u_{l'p'}|^2 + 2\,\mathrm{Re}(u_{lp}u^*_{l'p'})\,, \tag{4.12}$$

where the first two terms each originate from the two modes alone and thus continue to be axially symmetric. However, the interference term

$$2\,\mathrm{Re}(u_{lp}u^*_{l'p'}) = 2|u_{lp}||u_{l'p'}|\cos\big((l-l')\phi - (2p+|l|-2p'-|l'|)\arctan(z/z_\mathrm{R})\big) \tag{4.13}$$

has a phase term with azimuthal dependence as long as $\Delta l = l - l' \neq 0$ and is non-stationary in the axial direction when $\Delta n = n - n' \neq 0$, where $n := 2p + |l|$ is the combined mode number. If these conditions are met, the interference of the modes with different orbital angular momentum phases $\mathrm{e}^{\mathrm{i}l\phi}$ and $\mathrm{e}^{\mathrm{i}l'\phi}$ and Gouy phases ψ_{lp} and $\psi_{l'p'}$ let the intensity distribution undergo a scaled-rigid rotation along the z-axis.

For the sake of simplicity, I have shown this for the superposition of two LG modes with unity coefficients, but the conclusions drawn below remain valid for the superposition with complex coefficients of any number of LG modes, provided that all interference terms rotate at the same velocity. This is the case if

$$\frac{n_{j+1}-n_j}{l_{j+1}-l_j} = \frac{\Delta n_j}{\Delta l_j} =: V_j \tag{4.14}$$

is the same for all LG modes j in ascending order $n_j \leq n_{j+1}$, that is, $V_j = \text{const.}$ holds. The derivation for this general case is shown in Appendix B, which details the results in Reference [71].

Figure 4.6 b) shows examples of LG mode superpositions. As can be seen, the phase profiles of the superpositions exhibit vortex singularities and discontinuities like the pure LG modes themselves, but are no longer on the optical axis, respectively radially symmetric. Accordingly, regions of vanishing intensity can be found again at these locations. This forms the azimuthally asymmetric intensity profiles with several lobes off the optical axis. Example A results in a lobe "anti-lobe" pair centered around the optical axis, examples B and C result in two and three lobes respectively. Example D results in an intensity profile where the brightest regions form a cross.

In the following, we will examine the properties of rotation in general, and then in relation to these examples.

4.4.2 Properties of the rotating PSF

We will first restrict ourselves to PSFs obtained from LG mode superpositions that satisfy the condition of scaled-rigid rotation (i.e., Equation 4.14). The angular velocity of the rotation following from Equation 4.13 is

$$\frac{\mathrm{d}\phi}{\mathrm{d}z} = V\frac{\mathrm{d}}{\mathrm{d}z}\arctan(z/z_\mathrm{R}) = V\frac{1}{1+(z/z_\mathrm{R})^2}\,, \tag{4.15}$$

---

[8] Applying the rotation operator around the z-axis, $\mathbf{R}_z(\theta)\,u_{lp} = \mathrm{e}^{\mathrm{i}l\theta}u_{lp}$, it is easy to see that u_{lp} is an eigenfunction of $\mathbf{R}_z(\theta)$ with eigenvalue $\mathrm{e}^{\mathrm{i}l\theta}$.

where $V := \Delta n/\Delta l$ is the ratio of mode number differences. Integration gives the rotation angle of the intensity pattern relative to the one at $z = 0$

$$\theta(z) = V \arctan(z/z_{\mathrm{R}})\,, \tag{4.16}$$

which is also plotted in Figure 4.6 a). The intensity pattern thus rotates by $V \cdot \pi/2$ within the Rayleigh range, and overall by $V \cdot \pi$ from $-\infty \to +\infty$.

The intensity profiles at different z-positions of the previously discussed mode superposition examples are shown in Figure 4.6 c). The scaled-rotating character is directly visible for examples A-C. It is also apparent that they rotate to different degrees. Within the Rayleigh range shown, Example A rotates by $\pi/2$, since $V = 1$ in this case. For Example B, $V = 2$ results in a rotation of π of the double-helix-shaped intensity distribution along z. Remarkable is the very slow rotation of the triple helix in Example C, which results from the fact that the azimuthal mode indices of the constituent LG modes have different magnitude *and* sign and enter Δn as their absolute value, but Δl with their sign, giving $V = 1/3$ and thus a rotation of $\pi/6$ within the Rayleigh range. It becomes clear that the rotation speed can be chosen arbitrarily large or small (in discrete steps) by careful choice of the mode numbers.

Example D does not exhibit scaled-rigid rotation, since the condition for such rotation (Equation 4.14) is not fulfilled. Nonetheless, this mode superposition exhibits a rather interesting behavior: The cross in the waist is imaged back on itself at exactly the Rayleigh distance (and again in the far field), and appears at half the Rayleigh distance rotated by exactly $\pi/4$. In between, no rotation happens, but rather a gradual switching of intensity from the vertically oriented cross to the twisted cross and vice versa.

In fact, rotating LG mode superpositions are only a subset of a more general group of so-called generalized self-imaging beams, as elaborated in Reference [136]. Their defining condition, Equation 4.14 with $\Delta l \neq 0$ and $\Delta n \neq 0$, can also be represented in the modal plane spanned by the mode indices l and n as all mode combinations laying on straight lines. As can be seen from Figure 4.6 d), this is the case for examples A-C. Example D can be classified into another subcategory, the scaled self-imaging beams, for which the transverse intensity profile is self-reproduced at certain z-positions with in general different orientations and scales. Such mode combinations lie on a set of equidistant lines parallel to the l-axis, as in the case of Example D.

The scaling behavior of the generalized self-imaging beams remains unchanged from the LG modes. For the group of rotating mode combinations, this can be seen from equations 4.12 and 4.13 (or from the analogous Equation B.10 for any number of modes). Any lateral distance d_0 within the intensity profile at $z = 0$ therefore scales as the beam radius Equation 4.8. By insertion of Equation 4.16 one obtains the scaling

$$d = \frac{d_0}{\cos\left(\frac{\theta(z)}{V}\right)} \tag{4.17}$$

in terms of the rotation angle $\theta(z)$.

4.4.3 PSF engineering in the pupil plane

The original PSF of an imaging system can be modified by modulating the amplitude and/or phase of the light beam forming the image. In order to form the PSF as LG mode (superposition), phase modulation is required, as this is the only way to create the essential phase vortices. Ideally, one has control over both phase and amplitude, but phase-only modulation will be discussed here, as this entails less instrumental complexity. Since we want to change the PSF independently of the lateral position in the object plane, the modulation must take place in the Fourier plane, which, as we saw in Section 4.2.1, corresponds to the pupil plane.

The pupil function of a typical[9] imaging system is simply the circ-function,

$$P(u,v) = \mathrm{circ}_a\left(\sqrt{u^2+v^2}\right) , \tag{4.18}$$

i.e. unity within the pupil of radius a and zero outside.[10] The phase-modulated generalized pupil function (cf. Section 4.2.3) can then be written as

$$\mathcal{P}_{\mathrm{mod}}(u,v) = P(u,v)\, \exp\left(\mathrm{i}kW(u,v)\right)\, \exp\left(\mathrm{i}\Phi(u,v)\right) , \tag{4.19}$$

with the curved phase front due to aberrations $W(u,v)$ and a phase mask $\Phi(u,v)$. Hence, the phase engineering can also be viewed as a controlled manipulation of the aberrations of the system.

Our objective lens was designed to fulfill the Abbe sine condition, which makes the objective insensitive in first order to comatic aberration, so that off-axis objects can be imaged sharply [16]. It requires that the sine of the object space angle is always proportional to the sine of the image space angle [143]. Given the high numerical aperture of our objective lens, the amplitude of an isotropically emitting point source is not constant in the pupil plane. This so-called apodization must be taken into account, and is described in Reference [16]. In the case of the Abbe sine condition, the intensity increases as $A_{\mathrm{Abbe}} = 1/\cos(\alpha)$ at the edges of the pupil plane, where α is the incidence angle with respect to the optical axis.

The modified three-dimensional PSF may then be written as the absolute squared two-dimensional Fourier transform of the modified electric field in the pupil plane

$$\mathrm{PSF}(x,y,z) = \left|\mathcal{F}\left\{\mathcal{E}_0(u,v)\,\mathcal{P}_{\mathrm{mod}}(u,v)\,\mathrm{e}^{\mathrm{i}kz\mathrm{NA}w(u,v)/a}\right\}(\kappa_u,\kappa_v)\right|^2 , \tag{4.20}$$

evaluated at the spatial frequencies $\kappa_u = kx/f$ and $\kappa_v = ky/f$, i.e. similar as for the two-dimensional PSF (cf. Section 4.2.3). Here, f denotes the system's front or back focal length. The term $\mathrm{e}^{\mathrm{i}kz\mathrm{NA}w(u,v)/a}$ accounts for the defocus, where

$$w(u,v) = \sqrt{a^2/\mathrm{NA}^2 - \left(u^2+v^2\right)} , \tag{4.21}$$

using $\mathrm{NA} = \sin\left(\alpha_{\mathrm{max}}\right) = a/f$ and the collimated beam radius a. It can then be thought as the defocus aberration to add to the pupil function depending on the z-coordinate at which the PSF is evaluated. A derivation based on References [144, 145] is presented in Appendix C.1. The incident electric field is given by

$$\mathcal{E}_0(u,v) = E_0\left(1 - \frac{u^2+v^2}{a^2}\mathrm{NA}^2\right)^{-1/4} \tag{4.22}$$

according to the apodization function written in pupil coordinates. A derivation can be found in

---

[9] Typically, optical systems have a circular aperture stop, as is the case for our system.

[10] Or in mathematical terms, $\mathrm{circ}_a(\rho) = \begin{cases} 1, & \text{if } \rho \le a \\ 0, & \text{otherwise} \end{cases}$.

Appendix C.2.

That gives us a model for a PSF of the microscope arbitrarily phase-modulated in the pupil plane. We will also exploit this in Section 4.5.3 to simulate engineered PSFs by numerically computing Equation 4.20. However, it is at first non-trivial how to find a suitable phase mask to form (superpositions of) LG modes from the original PSF. However, we can take the same holographic approach as when creating pure LG modes using phase-only modulation [146–149] and simply use the phase of the LG mode combination $U = \sum_i a_i\, u_{l_i p_i}$ at the waist as the phase mask, i.e.

$$\Phi(u, v) = \arg\left(U|_{z=0}\right) . \tag{4.23}$$

By applying the phase of the desired field U to the field incident in the pupil plane, we obtain the desired field with high purity. The purity is given by the field overlap and is bounded in that we do not have control over the amplitude.

The LG modes are eigenfunctions of the Fourier transform[11] [136, 150], so we also get the LG mode combination in the image plane. Diffraction at the limited aperture must also be considered. Since the field in the pupil plane is multiplied by the pupil function $P(u, v)$, the field in the image plane can be described according to the convolution theorem[12] as the field without any aperture convolved with the Airy disk.

From our considerations, the choice of the parameter w_0 of the LG modes is not yet evident. In fact, this choice is not simple either, as the amount of light in the desired modes[13] depends on the ratio of aperture radius and LG mode waist a/w_0, even if we could modulate the amplitude, in a way that depends on the modes themselves [151, 152]. This can be easily understood if one remembers that the properties primarily determining a particular LG mode are the phase discontinuities and singularities, which (especially also for LG mode superpositions) are located away from the optical axis. The more the aperture cuts off in the pupil plane, the less of the desired mode components are still contained in the resulting field. Moreover, since we do not modulate the amplitude and it is constant in the pupil plane (leaving aside the apodization), too large a/w_0 would also reduce the mode purity again, since the amplitude then deviates more and more from the amplitude of the desired field. As has been shown in Reference [149], the theoretically achievable output mode purity of our method indeed has a maximum of around 80 % at a certain value a/w_0, which depends on the LG mode.[14] Due to the complexity, for our rotating PSF it is easiest to manually optimize the w_0 used so that the resulting PSF in the image plane matches the desired PSF as closely as possible.

The fact that we cannot produce the rotating PSF from LG mode combinations with perfect purity raises the question whether the rotational properties remain unchanged. This is significant as our axial localization is based on accurate knowledge of the rotational behavior. However, the fidelity of the PSF engineering can be made large enough that it follows the simple model of scaled-rigid rotation of Equation 4.16. This was verified for our choice of PSF in an optical test setup as well as in a simulation

---

[11] This can be shown via the Hankel transform and gives the eigenvalue $(-1)^p (\mathrm{i})^{|l|} = \mathrm{e}^{\mathrm{i}(2p+|l|)\frac{\pi}{2}} = \mathrm{e}^{\mathrm{i}\frac{\pi}{2}n}$ corresponding to a LG eigenfunction u_{lp} [150].

[12] The convolution theorem states that $\mathcal{F}\{f * g\} = \mathcal{F}\{f\} \cdot \mathcal{F}\{g\}$ for one- or multi-dimensional functions f and g [119]. As corollary, applying the inverse Fourier transform also yields $\mathcal{F}\{f \cdot g\} = \mathcal{F}\{f\} * \mathcal{F}\{g\}$.

[13] The projection of an arbitrary field V on the mode combination $U = \sum_i a_i\, u_{l_i p_i}$ is given by $\langle V|U\rangle$, with the scalar product and the notation explained in Appendix B.1.

[14] For the LG fundamental mode, the Gaussian beam, the ideal a/w_0 is the one that gives the highest overlap with the Airy disk (the diffraction pattern of a circular aperture).

(see Section 4.5.3).

Moreover, as we will see in Section 4.4.5, the fidelity can be optimized beyond these limits.

4.4.4 Comparison with standard PSF

Engineering a rotating PSF is only useful if it also gives better three-dimensional position information than the already present regular PSF. The information theoretic approach mentioned in Section 4.2.2 provides the mathematical framework to study this question and is introduced e.g. in Reference [153].

The Fisher information gives the possible precision of the localization. More precisely, the reciprocal of the Fisher information with respect to a parameter is a lower bound for the variance of an unbiased estimator of this parameter. This follows from the so-called Cramér-Rao inequality which also gives the name CRLB to the lower bound. To define the Fisher information, consider an observable X whose probability depends on a parameter η. The Fisher information describes the amount of information that the observable X contains about the unknown parameter η. It is defined to be the variance of the partial derivative of the log-likelihood function with respect to the parameter. For a single parameter η and the probability density function $f(X;\eta)$, the Fisher information can thus be written as

$$I(\eta) = \mathrm{E}\left[\left(\frac{\partial}{\partial\eta}\ln f(X;\eta)\right)^2 \middle| \eta\right] = \int \left(\frac{\partial}{\partial\eta}\ln f(\chi;\eta)\right)^2 f(\chi;\eta)\mathrm{d}\chi\,. \tag{4.24}$$

Note that it does not have to be a probability distribution over a one-dimensional space. The distribution is assumed to be single-parametric here; for multi-parameter models, the Fisher information can be written as a matrix.

A normalized transverse intensity distribution can be understood as a probability density. Thus, Equation 4.24 can be used to calculate and compare the Fisher information with respect to a spatial coordinate $\eta \in \{x, y, z\}$ for transverse intensity distributions

$$f(x, y; \eta) = \left| U|_{z=z_0} \right|^2 \tag{4.25}$$

at axial position z_0. Accordingly, the integration $\mathrm{d}\chi$ is along both transversal dimensions. Figure 4.7 shows the Fisher information as a function of the axial position z with respect to each coordinates x,y and z for the DH-PSF (Example B in Figure 4.6) and in comparison for the fundamental mode (the first example in Figure 4.5). The latter can be considered the standard PSF in terms of LG modes. For the fundamental LG mode, one obtains the simple analytical expressions

$$I(z) = 4\left(\frac{w_0}{z_\mathrm{R}}\right)^2 \cdot \frac{(z/z_\mathrm{R})^2}{\left(1+(z/z_\mathrm{R})^2\right)^2} \qquad \text{and} \qquad I(x) = I(y) = \frac{4}{1+(z/z_\mathrm{R})^2}\,. \tag{4.26}$$

For more complex expressions, such as those arising in the DH-PSF, the derivative and integration can be computed numerically.[15]

As can be seen in Figure 4.7, the DH-PSF provides higher Fisher information for the localization along all dimensions as compared to using the standard PSF. In particular, unlike the standard PSF, it

---

[15] To evaluate the numerical error introduced hereby, the numerical calculation for the fundamental mode was compared with the analytical result from Equation 4.26, revealing a very high agreement.

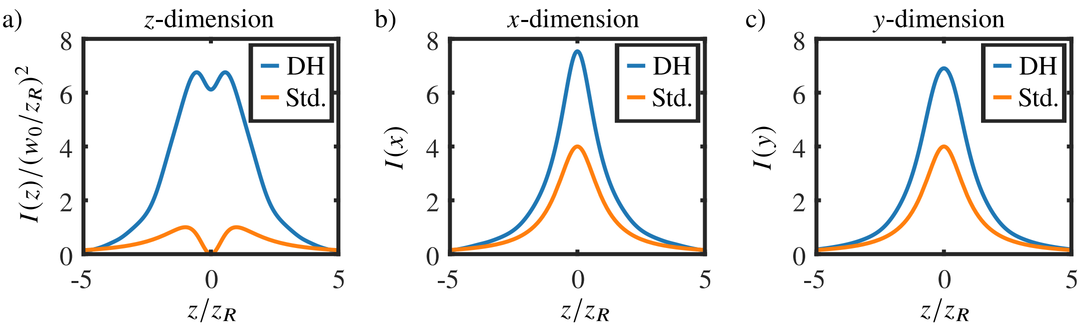

Figure 4.7: Fisher information as a function of axial position z of the DH-PSF and the standard (Std.) PSF with respect to the a) axial z-dimension, b) x-dimension and c) y-dimension. The DH-PSF corresponds to Example B in Figure 4.6. The standard PSF corresponds to the fundamental Gaussian mode, shown first in Figure 4.5. Note the different units of the ordinate.

provides high axial information even near the focus, as evident from Figure 4.7 a). The superior axial information of the double helix thus provides a decisive advantage over merely relying on the defocus. Moreover, it exceeds the axial information of the standard PSF over a large axial domain, meaning an enhancement of the DOF by the DH-PSF. It is interesting to note that the double helix provides a larger Fisher information even for localization along the lateral dimensions, as can be seen in figures 4.7 b) and 4.7 c). However, this does not necessarily mean that the double helix is better for applications involving a single lateral plane, as the larger extent of the PSF makes the localization of closely spaced emitters less trivial and the peak intensity is lower for a limited photon budget. The slightly higher maximal Fisher information of the DH-PSF along the x-dimension compared to the y-dimension results from its azimuthal asymmetry. In focus, it consists of two lobes displaced from the origin in x-direction, wherefrom it becomes apparent that it gives more information about the x- than the y-position.

Here, for simplicity, we assumed no noise or other detrimental effects (such as the limited mode fidelity described in Section 4.4.3), so that the Fisher information can be calculated analytically from the theoretical intensities. But also when considering a limited SNR and taking into account the limited mode fidelity, the conclusions remain, as shown in references [75, 83, 137]. The DH-PSF provides higher and more uniform Fisher information for three-dimensional localization as compared to using a standard PSF.

It should be emphasized here that the Fisher information evaluates local changes of a parameter. Nonlocal properties of the PSF, such as its repetition along the optical axis, are in fact not incorporated. Arguably, rotating PSFs also have a distinct advantage over the standard PSF in that they are not symmetric about $z = 0$.

For quantum gas microscope experiments with densely filled optical lattices [85], it is of relevance not to lose the lateral single-site resolution due to the widening of a modified PSF leading to overlapping PSFs. Taking the DH-PSF as an example, the larger extent and the task of correctly pairing lobes of overlapping PSFs can initially be believed to be an inherent disadvantage. However, as reported in Reference [79], the particular shape and spacing of the lobes can help determine the underlying positions of the emitters. In fact, similar to the one-dimensional PSF case described in Reference [39], relatively dense ensembles in which the PSFs of close-by emitters overlap can be super-resolved, in all three dimensions [79].

4.4.5 Optimization of the rotating PSF

The mode fidelity limitations arising from diffraction and sole phase modulation (see Section 4.4.3) can be overcome by iteratively optimizing the phase mask. Optimization also permits to select a PSF according to specific features. Reference [73] proposes for this purpose to optimize the pupil function for a continuous rotation of the main lobes within a bounded axial range only, the maximum intensity being directed into the main lobes, and the transfer function modulating only the phase. The intensities in the pupil plane and the three-dimensional PSF must be constrained, and the phase degrees of freedom of the two domains are used as the free degrees of freedom. The PSF we determined analytically (cf. Section 4.4.3) is taken as a first estimate. To enforce the rotational property in the iterative process, the field is projected onto the LG modes and multiplied in the LG modal plane by a weighting function that amplifies the modes that lie on a cloud around the line defining the exactly rotating PSF. This method is nothing but a form of computer-generated hologram calculation, a well-established way of creating particular intensity patterns using a phase mask [119, 154]. The main disadvantage of rotating PSFs, the distribution of intensity into a larger area, which is a problem for photon-limited applications like ours, can be mitigated by this optimization, since over 30 times more intensity can be concentrated into the main lobes compared to exactly rotating PSFs, as has been reported in Reference [73]. The super-resolved three-dimensional localization of single molecules reported in Reference [74] uses a PSF optimized in this way.

These geometric PSF design approaches are simple and computationally fast. However, they are not optimal because they do not reach the fundamental limit of precision for a given physical system. They also lack consideration of effects of existing noise statistics on their optimality. To achieve the fundamental resolution limit of localization (the CRLB, see Section 4.2.2), the pupil plane phase mask can be optimized by means of maximizing the information content of the PSF (including the noise statistics). Reference [78] took the approach of optimizing the number and position of vortex singularities used for an analytical phase mask in the pupil plane for maximum Fisher information, while Reference [80] restricts the phase degree of freedom in the pupil plane to the first 55 Zernike modes.

Such optimization problems are generally not convex, so finding a global minimum is not guaranteed. One approach is to run the optimization routine several times with random initial values and select the best final result. The choice of optimization algorithm plays an important role for convergence, one choice could be the genetic algorithm as described in Reference [155]. The optimization can be done on simulated PSFs as in the presented literature. I suggest to do it directly in the system with the atoms, as this way all noise sources are automatically taken into account correctly. I elaborate on this in more detail in Section 4.5.1.

For experiments with high emitter densities, e.g. for densely filled optical lattices, an optimized PSF should be laterally compact in order to minimize their overlap, especially in cases where the Abbe radius is larger than the horizontal lattice constant. For example, the lobes of a DH-PSF can be moved further together until a bean-shaped, helicoidally rotating distribution is formed. Therefore, I propose to include in addition to the Fisher information an area cost function in any such PSF optimization, which penalizes PSF with large extent. I expect this to facilitate the three-dimensional localization of dense ensemble as reported in Reference [79].

For optical lattices, because of their discrete nature, the constraints on the axial form of the PSFs can also be relaxed to require that only discrete axial positions have easily distinguishable PSFs. As an illustrative example, consider Example D from Figure 4.6. Ultimately, the choice of PSF must be tailored precisely to the intended experiment.

4.4.6 Other approaches and applications

Inspired by the pioneering works of constructing rotating PSFs with LG modes, other methods for creating rotating PSFs have been developed using Fresnel zones in the Fourier plane, where successive zones carry spiral phase profiles with successively larger topological quantum number [156]. Interesting extensions of the pupil plane engineering idea are described in reference [157, 158], which demonstrate possible setups to engineer the optical wavefront independently in both polarization directions. This allows, in addition to the three-dimensional localization, aberrations in both polarization channels to be measured and removed independently. The rotating PSF has applications not only in fluorescence microscopy of single molecules, or in our case, single atoms. The idea has also been used in laser scanning microscopes [81]. PSFs consisting of LG mode superpositions were also used as optical tweezers [159].

It should be noted that rigid rotation is by no means necessary, but is merely a simple way of parameterizing the axial position from an axially changing PSF. As long as the axial behavior of the PSF is known and unambiguous, the axial position can be inferred from the measured PSF.

A similar approach was recently reported in Reference [160]. Wave-front shaping in a quasi-image plane, i.e., a plane in between pupil and image plane, enables to sharply image three-dimensional configurations of atoms. For this purpose, different areas of the FOV are focused differently using holographic Fresnel lenslets. As these areas have to be selected prior to a measurement, it is *a priori* not possible to extract the axial position from a single image beyond the level of precision of the defocus.

4.5 Experimental implementation of PSF engineering

To implement the PSF engineering described in Section 4.4.3, we need a way to spatially modulate the phase of the light emitted by the atoms. This can be done using a spatial light modulator (SLM), which I describe in Section 4.5.1. In Section 4.5.2, I describe the design and adjustment of the new microscope setup. I then discuss the choice of PSF for subsequent measurements in Section 4.5.3. In particular, a simulation is used to to show that vertically adjacent lattice sites are expected to be resolvable.

4.5.1 Spatial light modulator

To realize the spatial phase modulation, a reflective liquid crystal on silicon (LCoS) SLM with parallel-aligned nematic (PAN) arrangement is used.[16] To understand how SLMs can be used for this purpose, I will give a brief overview of the principle of operation. A good description can be found in references [161, 162].

Principle of operation. Liquid crystals (LCs) simultaneously exhibit the viscous properties of a liquid and macroscopic anisotropy as in a crystalline solid. In the so-called nematic phase, LC molecules tend to align their long axes with respect to neighboring molecules, resulting in long-range orientation order and hence optical anisotropy. The local average orientation of the molecules is called the director and is described by the field of unit vectors $\hat{\boldsymbol{n}}(\boldsymbol{r})$. Without external forces affecting the director field, nematic LC materials are uniaxially birefringent. The refractive indices for light with polarization perpendicular and parallel to $\hat{\boldsymbol{n}}$ are denoted as n_o and n_e, respectively (ordinary and extraordinary ray). For light

---

[16] SLM-100 from Santec.

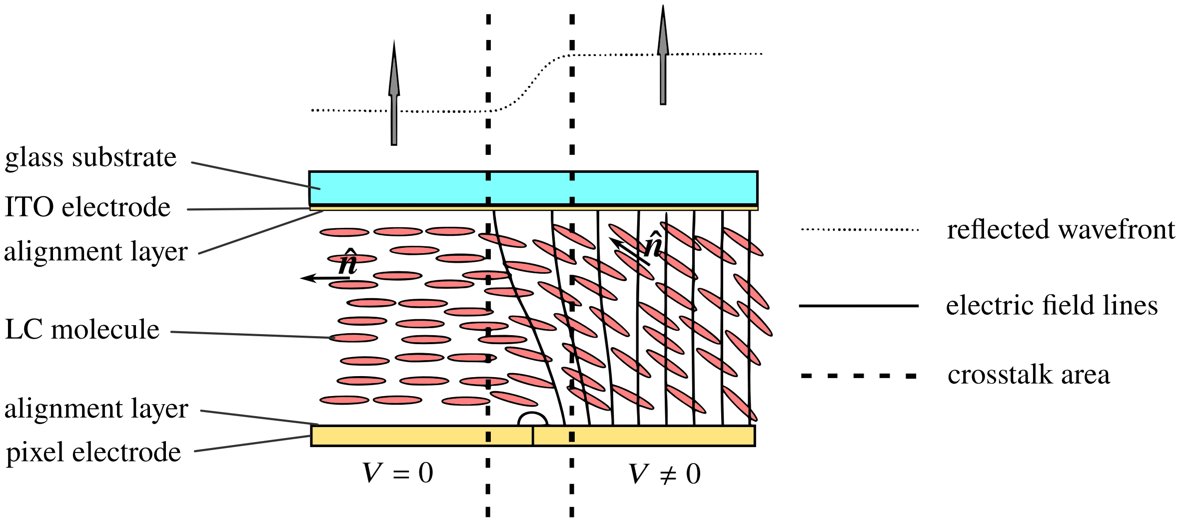

Figure 4.8: Section of two adjacent pixels of a PAN LCoS-SLM. No voltage is applied to the left pixel, so the LC molecules align parallel to the alignment layer. The higher the AC voltage applied to the pixel on the right-hand side, the more it aligns the molecules in the electric field direction. This results in a different refractive index and thus a phase difference for the polarization lying in the sectional plane (i.e., parallel to the optical axis of the SLM) in this pixel. The local average orientation $\hat{\boldsymbol{n}}$ is indicated at two points. Crosstalk occurs in the boundary region of the pixels due to the smooth transition of the director field. Taken and modified from [161].

propagating at an angle θ relative to $\hat{\boldsymbol{n}}$, the polarization component in the plane of $\hat{\boldsymbol{n}}$ and the direction of propagation experiences an effective refractive index [161, 162]

$$n_{\mathrm{eff}}^2 = \frac{n_o^2 n_e^2}{n_o^2 \sin^2(\theta) + n_e^2 \cos^2(\theta)} . \tag{4.27}$$

In the LCoS-SLM, the LC is located between two parallel oriented alignment layers, near which surface interaction causes the molecules to arrange themselves accordingly (hence the term *parallel-aligned nematic* arrangement), cf. Figure 4.8. In the presence of an electric field, LC molecules align in the field direction due to induced molecular dipole moments. The alignment $\hat{\boldsymbol{n}}$, and thus the refractive index n_{eff}, can therefore be controlled by varying the field strength. For light polarized in the plane of rotation of LC molecules, the resulting optical path length difference is $2d\Delta n$, where d is the thickness of the LC layer and $\Delta n = n_{\mathrm{eff}} - n_o$ is the birefringence. Note that the reflective design doubles the modulation depth as the light passes through the LCs twice. This allows for variable phase retardation

$$\Delta\varphi = 2\pi \frac{2d\Delta n}{\lambda} \tag{4.28}$$

of light at a wavelength λ. The other polarization component, i.e. the ordinary ray, does not undergo any modulation. The field is applied by a transparent indium tin oxide electrode at constant potential on the top and reflective pixel electrodes controlled by complementary metal-oxide-semiconductor (CMOS) technology on the silicon substrate on the bottom. To avoid damage to the LC material by ion migration, the polarity of the applied field is switched [161–163], in our device at 1.2 kHz [164].

Specifications and limitations. A requirement for the SLM used is a high spatial resolution, as well as a high fill factor. This is fulfilled by 1 050 × 1 440 pixels of 10.0 µm length separated by 0.4 µm.[17] Indeed, the spatial digitization of the phase mask leads to a globally sinc^2-weighted diffraction intensity, which is more pronounced the coarser the sampling of the desired pattern [165]. Crosstalk occurs in the inter-pixel region, which smoothens the phase response to a certain degree (cf. Figure 4.8). Depending on the phase pattern, this can lead to both improved (e.g. for blazed gratings) and degraded phase response [166]. Reference [167] has determined the effective size of a Gaussian smoothing kernel to be at most 0.2 SLM pixels for our SLM. An anti-reflective (AR) coating minimizes losses from reflection at the transparent electrode and allows the overall reflectivity to be close to the panel reflectivity of around 80 %. The panel reflectivity is wavelength-dependent and amounts to 70 % for our imaging wavelength[18], the caesium D2 line at 852 nm. The applied voltages have a 10 bit addressing resolution [164] and provide a modulation depth of more than 4π at our wavelength [167]. This is important because phase digitization generally degrades image quality, depending on the phase pattern displayed [165]. The phase modulation is typically stable up to $10^{-3} \times 2\pi$ according to the manufacturer [164], whereas a stability of $8 \times 10^{-4} \times 2\pi$ was measured on our device [168]. The driver of the SLM reads the grayscale pattern to be displayed from a computer video signal and converts it to corresponding pixel voltages. The lookup table (LUT) to convert phase response to gray value at our wavelength established by Reference [167] is used. The response time depends on the phase pattern and is typically 100 ms.

The SLM also should not introduce aberrations into the system, i.e., the output light field should have as little additional phase front distortion as possible. SLMs however have a spatially slightly varying LC layer thickness and are slightly bend due to manufacturing conditions, causing a spatially inhomogeneous phase modulation. This was precisely measured for the SLM being used through phase shift interferometry, as reported in Reference [167]. The measured curvature amounting to $2.14\,\lambda$ peak-to-valley (PV) can be compensated for up to $\lambda/15$ PV or $\lambda/78$ RMS by superimposing a compensation mask on any desired phase pattern. It was rechecked by the method described in Reference [169] that the curvature has not changed much since the characterization. The wavefront distortion caused by the SLM after compensation is of the order of those arising from the (on-axis) aberrations of the high-NA objective lens. For example, the largest RMS wavefront distortions are caused by secondary astigmatism amounting to $-\lambda/67$ and primary astigmatism amounting to $-\lambda/100$ [59].

A major disadvantage of using an SLM is the need to work with polarized light, which means that initially only half of the unpolarized light from the atoms can be used. However, optical configurations have been designed that use both polarizations [157, 158]. Custom manufactured diffractive optical elements do not have this disadvantage and can reach higher optical efficiency [83], but at the cost of losing the programmable flexibility of an SLM.

How practical the SLM's programmability can be is illustrated by the idea, that it can be exploited to perform the optimization of the rotating PSF described in Section 4.4.5 directly on the system itself. To this end, in each iteration of the optimization algorithm, the PSF is measured at different axial positions, and the SLM is reprogrammed according to the optimization. In this way, all noise sources, such as the noise of the SLM, background noise, shot noise and camera noise, but also any aberrations (e.g. also of the SLM) are automatically taken into account correctly. This has not yet been done, instead in previous literature only simulated PSFs have been optimized [73–75, 78, 80].

---

[17] This gives a pixel pitch of 10.4 µm.

[18] The manufacturer specifies a reflectivity varying from 70 % to 90 % over the spectrum. Newer models also achieve over 90 % at our wavelength.

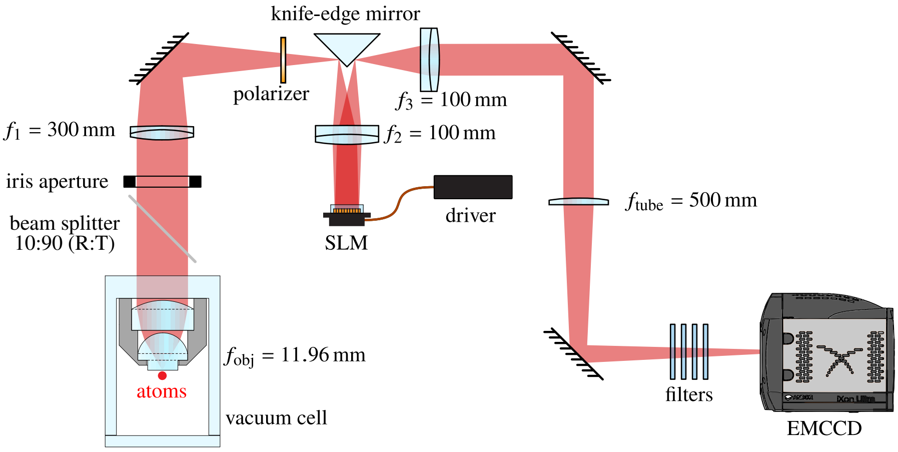

Figure 4.9: Schematic of the optical setup for phase-engineering the PSF. The fluorescence light from the atoms is collimated by the high-NA objective into a beam of 22 mm diameter at maximal NA, passes through a 10:90 (R:T) beam splitter (for the vertical MOT and PGC beams), a motorized iris, a polarizer, achromatic doublets and a knife-edge mirror to create another accessible pupil plane in which the SLM stands, and a tube lens to focus the light onto the camera. Filters in front of the camera block residual light from the vertical cooling (at 895 nm), the vertical lattice (at 1 064 nm) and stray light. A tube system (not shown in the figure) further reduces stray light.

4.5.2 Modified imaging system

In order to integrate the SLM into the existing imaging system described in Section 2.2, the system must be modified. Namely, the pupil plane of the system is located still inside the vacuum cell and is therefore inaccessible. Moreover, the SLM has to be used in reflective configuration at an angle as small as possible.

Experimental setup. The modified imaging system is shown schematically in Figure 4.9. A secondary pupil plane can be conveniently brought to an external location using a $4f$ relay. The focal lengths of the two lenses of the resulting telescope are chosen so that the collimated beam incident on the SLM is brought to the suitable size. To be precise, the collimated beam diameter of 22 mm at the maximal NA must be demagnified to fit the SLM chip with 10.92 mm along the shorter side. The chip should be utilized as much as possible to keep a high pixel resolution. A suitable choice are the lenses with $f_1 = 300$ mm and $f_2 = 100$ mm focal length respectively, so that a certain tolerance remains for centering the imaging beam on the SLM.

The optical design was made to preserve the existing beam path (cf. Figure 2.3), thereby minimizing new mechanical stresses caused by a different weight distribution on the optical breadboard, which could otherwise lead to misalignment of the optical lattice beams. To realize the necessary perpendicular incidence on the SLM, I used a knife-edge mirror[19] directing the light onto the SLM and back again, as it is shown in Figure 4.9. The knife-edge mirror is mounted in the intermediate image plane, since this is where the image beam has the smallest extent. For atoms at the edge of the field of view, the corresponding intermediate image is formed about 1 mm away from the optical axis. The mirror is therefore mounted such that the prism edge is more than 1 mm below the optical axis.

---

[19] Right-angle prism with broadband dielectric coating.

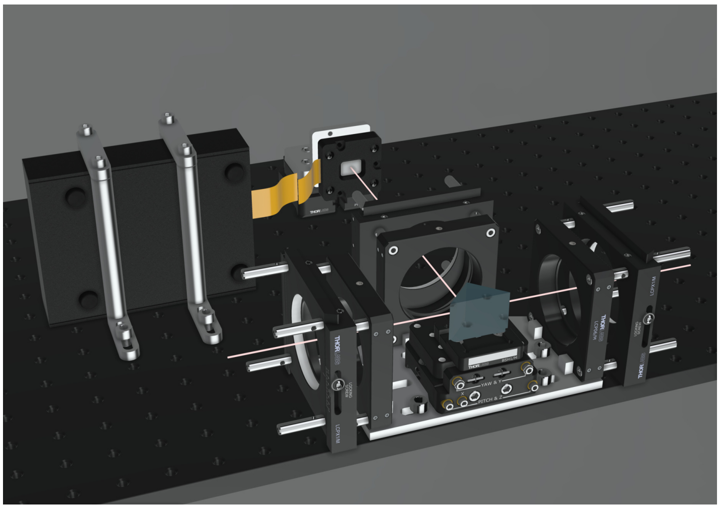

Figure 4.10: CAD model[20] of the mounts of the SLM, the SLM driver and the knife-edge mirror. The breadboard is vertically mounted on top of the upper level of the experimental table above the vacuum cell. Both the SLM and the knife-edge mirror are installed on a 5-axis stage. Translating cage segment plates allow to set the height of the mirror prism relative to the beam (46 mm above the breadboard). The optical axis is marked by a light red line.

A polarizer is required in the beam path, as the SLM only works with linear polarization. It is mounted in a switchable holder allowing the microscope to be used without a polarizer when the SLM is switched off. Due to the relatively small free aperture of the polarizer, it is mounted just before the intermediate image plane at the knife-edge mirror.

Finally, another telescope produces the image that can be captured by the electron-multiplying charge-coupled device (EMCCD) camera. The focal lengths of the lenses are selected so that the overall system has the desired transverse magnification while remaining compact. The magnification for this setup amounts to

$$M = \frac{f_1}{f_{\text{obj}}} \cdot \frac{f_{\text{tube}}}{f_3} = 125.42\,, \tag{4.29}$$

thus satisfying the Nyquist-Shannon condition $r_{\text{Abbe}} > 2\Delta_{\text{s}}$ [39] with a factor of 3.6 at maximal NA, where $\Delta_{\text{s}} = \Delta_{\text{px}}/M$ is the sampling spacing in the object plane and $\Delta_{\text{px}} = 16\,\mu\text{m}$ is the pixel size of the EMCCD camera. The initial design magnification of $M = 104.5$ (see Section 2.2) can be easily obtained in this setup by reducing the magnification between the intermediate image plane and the camera plane. For the purposes of this work, the field of view is not required to be as large as possible, which is why the magnification chosen is perfectly suitable. The axial magnification is given by $M_z = M^2$.

To allow adjustment of the image beam through the microscope, especially relative to the installed SLM, both the knife-edge mirror and the SLM are mounted on 5-axis stages. Figure 4.10 shows a rendering of the designed CAD model. A tube system can be attached to the mounts to shield as much stray light as possible from the camera.

Alignment procedure. The main challenge lies in alignment, as the light from the atoms is too faint for coarse alignment and no brighter point source can be placed in the atom plane.

---

[20] Kindly compiled by Waldemar Graf from the precision mechanics workshop of the institute. The rendering was done by me.

As an aid to coarse alignment without the atoms, a collimated laser beam at $\lambda_{\mathrm{D2}} = 852\,\mathrm{nm}$ is directed to the free port of the 10:90 (R:T) beam splitter (from the right side in Figure 4.9). The vertical dipole trap (VDT) beam retroreflected at the objective lens is used as a reference for the imaging optical axis. Thus, the first step is to ensure that the VDT beam is well aligned and retroreflected into its fiber coupler. Then, the top vertical MOT and PGC beams both impinging the beam splitter are overlapped with the VDT by fiber coupling. Subsequently, the bottom MOT and PGC beams are overlapped with their respective counterparts from the top. The auxiliary beam can now be overlapped with the upper MOT or PGC beam and then used for a first coarse adjustment of the beam path through the microscope, at first without knife-edge mirror, SLM and the lenses.

However, because of the finite thickness of the beam splitter, the auxiliary beam adjusted in this way is slightly displaced relative to the optical axis defined by the VDT. In a next adjustment iteration, the residual transmission of the VDT through the objective is therefore exploited. At high intensity (e.g. at 5 W) the VDT can be observed and centered on the camera with the filter for $\lambda_v = 1\,064\,\mathrm{nm}$ removed. The optical axis is now also given by an iris diaphragm screwed to the camera and the motorized iris diaphragm. The auxiliary beam can be matched to the optical axis by maximizing the power transmitted through both nearly closed iris diaphragms, allowing it to be used for the adjustment of all optical elements.

The positions of the lenses can be optimized based on the wavefront curvature measured by a shear plate interferometer. The distance of the first lens ($f_1 = 300\,\mathrm{mm}$) from the back focal plane of the objective can however only be positioned using a length measurement. Therefore, the pupil plane only matches the SLM plane up to this precision. Using the 5-axis stages, the auxiliary beam can be precisely adjusted through knife-edge mirror and SLM center. The axial camera position can then be optimized based on the sharpness of atom images (with the SLM turned off). The polarizer is then placed in the beam and its axis is aligned to the SLM polarization axis by maximizing the diffraction efficiency of a blazed grating (for details, see e.g. Reference [167]) displayed on the SLM.

The last step is to fine-tune the centering of the SLM's phase mask. This can of course be done using the 5-axis stage, however this would be unwieldy given the iterative process involved. It is simpler to display the desired phase mask on the SLM with the corresponding displacement. To determine the required displacement, we first note that the image of the atoms can be shifted arbitrarily in the image plane based on orientation and period of a blazed grating (equivalent to a wrapped linear phase ramp) displayed on the SLM. As an illustration of this, compare Figure 4.11 a) without grating and Figure 4.11 b) with gratings in opposite directions. Similarly, we can also set a (long focal length) holographic lens, i.e., a parabolic phase mask, which shifts the atom images in a different direction when there is a mismatch between the optical axis and the phase mask center.[21] The displacement of the phase mask on the SLM is optimized in that the comparison between images with and without the holographic lens no longer shows a displacement of the imaged atoms.

Compensation of aberrations Despite careful alignment, aberrations are clearly visible, see Figure 4.11 c), taken at maximum NA. These can come from imperfect adjustment of the lenses and inherent lens aberrations. It remains to be investigated by ray tracing methods how large the effect on the aberrations is. However, I estimate them to be relatively insignificant due to the relatively small NAs up to 0.037 on the image side of the objective. Another cause of the aberrations could be an imperfect curvature compensation of the SLM (cf. Section 4.5.1). The phase curvature of the SLM could have

---

[21] This is no different from the displacement of a beam centered on the optical axis after passing through an uncentered lens.

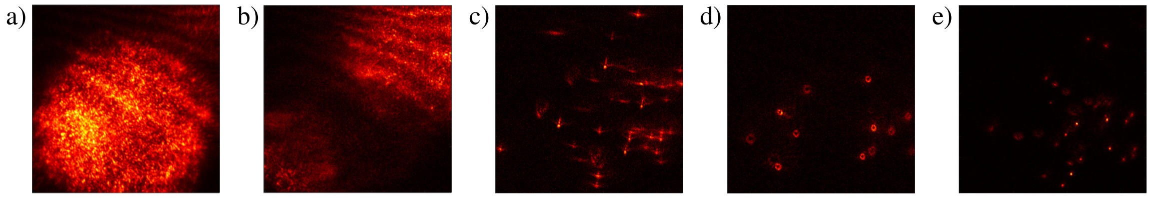

Figure 4.11: Example fluorescence images of the adjustment process. a) Filled three-dimensional optical lattice. b) A phase mask consisting of a diagonal blazed grating inside a circle and an oppositely oriented grating outside leads to diametrically diffracted images of the atoms. c) Sparsely filled lattice imaged with a regular PSF without aberration compensation. d) Sparsely filled lattice imaged with a "doughnut" PSF (or more specifically the LG mode u_{10}) after aberration compensation. e) Sparsely filled lattice imaged with a regular PSF after aberration compensation. Images a) and b) were taken at NA = 0.72, images c)-e) at NA = 0.92.

changed slightly, for example, due to the SLM chip lying horizontally in this setup in contrast to the characterization measurements. Furthermore, the aberration could also result from an imperfect position of the optical lattice relative to the objective lens. As follows from the aberration characterizations outside the vacuum cell presented in Reference [59], the aberrations significantly deteriorate already 38 µm from the optical axis of the objective lens. The center of overlap of the VDT and horizontal dipole trap (HDT) beams must therefore be adjusted to micrometer accuracy, a demanding challenge.

The aberrations could have been determined as described in Section 4.2.3 and Reference [59] by fitting the measured PSFs with the lowest-order Zernike polynomials and subsequently compensated by displaying the inverse Zernike decomposition phase on the SLM. As a less complex and time-consuming, yet sufficient method for the purposes of proof-of-principle measurements, the Zernike aberration compensation mask to be displayed on the SLM was manually optimized. For this, the lowest 13 Zernike orders were used[22], i.e., astigmatism, coma, trefoil, secondary astigmatism (each vertical and oblique), and spherical aberration, but omitting piston and tilt (vertical and horizontal). The standard regular PSF is to be optimized, which must resemble an Airy disk as much as possible. However, a more clearly aberration-sensitive PSF helps with this type of optimization. I used the Doughnut-shaped LG mode with an azimuthal phase winding u_{10} (cf. Figure 4.5) for which aberrations lead to an unevenly distributed intensity across the ring. By iteratively changing the Zernike coefficients, a relatively uniform Doughnut can be created, as can be seen in Figure 4.11 d), leading to sharp regular PSFs with clearly less aberrations, as shown in Figure 4.11 e).

Visual optimization provided the best PSF with the coefficients $4.5\,\lambda$ for vertical astigmatism and $-1.5\,\lambda$ for oblique astigmatism, whereas changes in other Zernike coefficients did not provide visible improvements and were therefore left at zero. This result is not surprising, since the aberration characterization from Reference [59] already identified the primary and secondary astigmatism as the strongest aberrations with respectively $-0.010(1)\,\lambda$ and $-0.015(1)\,\lambda$ RMS wavefront error of the objective lens. The much stronger astigmatism in this system indicates that the center of the optical lattice deviates from the optical axis of the objective lens, as this causes astigmatism in the first order. However, other causes cannot be ruled out; further examinations would be required for this.

Owing to the flexible programmability of the SLM, the astigmatism could be identified as the strongest aberration and could be compensated for the most part. This now enables specific engineering of the PSF. A more detailed characterization of the residual aberrations is subject of future research.

---

[22] The complexity rapidly increases with the dimension of the optimization problem.

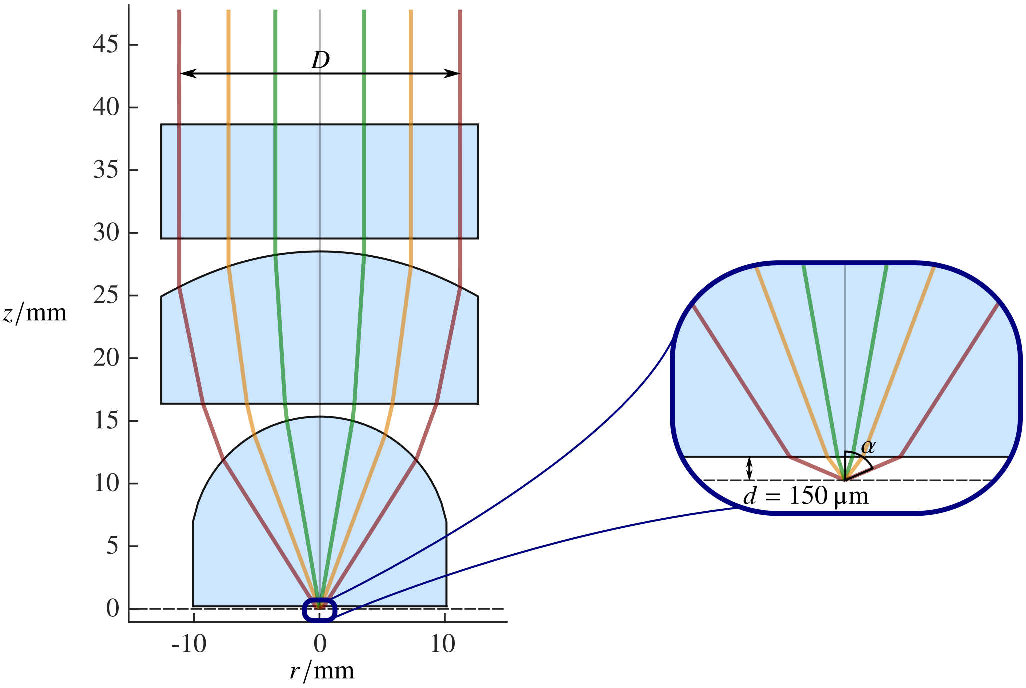

Figure 4.12: Ray tracing[23] of though the high-NA objective lens. Shown in different colors are the marginal rays for the NAs 0.3, 0.6 and 0.92. The region just below the objective is shown enlarged on the right. The rays each start on the axis at the working distance $d = 150\,\mu\text{m}$ under different angles α.

Setting the aperture stop In the original microscope setup, the pupil size could be adjusted by the motorized iris (see Figure 2.3). This then defines the NA as shown in Figure 4.12. However, the SLM can alternatively be used to define the pupil size, as it is located in a secondary pupil plane by design. For this purpose, a blazed grating with a sufficiently small period is displayed outside a circle corresponding to the aperture, and diffracts the light impinging there away from the camera's field of view. This is advantageous in that the programmed aperture can be centered exactly around the SLM's found center pixel (cf. Section 4.5.2). To limit the amount of stray light and the small undiffracted component, the motorized iris aperture is set as small as possible, but always slightly larger than the aperture defined on the SLM. If both apertures are the same, lateral misalignments risk making the overall aperture stop of the system asymmetrical by clipping.

Practically, the motorized iris is controlled by a step motor that adjusts the pupil diameter up to 35 mm in discrete steps.[24] For a target NA, the pupil diameter D is computed from

$$\text{NA} = \sin\left(\alpha_{\text{max}}\right) = \frac{D/2}{f_{\text{obj}}} \tag{4.30}$$

with the effective focal length of the objective lens $f_{\text{obj}} = 11.96\,\text{mm}$. For the pupil size in the SLM plane, the demagnification of $f_2/f_1 = 1/3$ has to considered. For instance, the diameters of 230, 460 and 705 SLM pixel are to be used to program the NAs 0.3, 0.6 and 0.92, respectively. The marginal rays

---

[23] Using a MATLAB based ray tracing software written by Dr. Andrea Alberti and the lens design reported in Reference [59].

[24] The possible motor positions range from 0° to 90° in steps of 1°, linearly corresponding to the diameters 0 mm to 35 mm.

corresponding to these NAs are shown in Figure 4.12.

4.5.3 The choice of the rotating PSF

We aim to extend the lateral single-site resolution to the axial dimension by engineering the PSF. In Section 4.4, I introduced the rotating PSFs suitable for this purpose. The DH-PSF subclass has a particularly suitable topology, since it allows a simple and robust determination of the rotation angle using the two lobes, and yet, thanks to the compactness, it provides relatively high intensities for a good SNR (cf. Figure 4.6). Based on the slope V in the modal plane, the rotation speed and thus the total rotation of the PSF along the optical axis can be set (see Section 4.4.2 and in particular Equation 4.16). The finite resolution of any angle determination ultimately determines the axial resolution, which is why the highest possible rotational speed is aimed for. However, the ambiguity of the intensity distribution is undesirable, being repeated after its rotational symmetry angle or, at the latest, after one complete rotation. Due to the defocus also occurring, the ambiguity is of course only complete in the angle of rotation, and intensity distributions can be distinguished by their scaling.

A good compromise for the DH-PSF with twofold rotational symmetry is made with the choice $V = 2$, whereby the PSF rotates by π within the Rayleigh range and overall by 2π. With this choice, the angle of rotation remains unambiguous within the entire Rayleigh range. To preserve lateral resolution as much as possible, modes with smallest radial extent are selected, i.e., with small radial mode numbers p, respectively small combined mode numbers n. The simplest implementation of this PSF is chosen, which is given by the LG mode superposition $U = u_{00} + u_{21}$ (Example B in Figure 4.6).

The choice of the waist w_0, or equivalently the ratio of aperture radius and waist a/w_0 has a certain optimal value due to the finite aperture and the uncontrolled amplitude in the pupil plane, as we saw in Section 4.4.3. In the following I will describe how this optimum is found. Subsequently I present the simulation of the light propagation made to ensure a PSF engineering fidelity sufficiently large for the PSF to follow the scaled-rigid rotation model (see the discussion in Section 4.4.3). This also allows to test if the amount of rotation between adjacent vertical lattice planes is sufficient.

Choosing the LG waist The choice of the ratio of aperture radius and LG mode waist a/w_0 affects the shape of the resulting PSF. For pure LG modes created by sole phase-modulation with a homogeneous amplitude, it was shown in Reference [149] that the optimum of the resulting mode fidelity is given at values around $a/w_0 = 2$ to 4 for low mode numbers $p, l \leq 5$, depending on the specific LG mode. As our DH-PSF consists of a superposition of modes in this range, I expect an optimum in this order of magnitude here as well. The waist was manually optimized in an optical test setup until the resulting PSF most closely matches the desired DH-PSF, giving $a/w_0 = 2.97$. The optimization can certainly be refined by a quantitative evaluation of the mode overlap. However, a variation of this parameter has confirmed this optimum also for DH-PSF with the atoms.

Simulating the PSF. The basic idea of the simulation is to physically model the light field in the pupil or SLM plane, then calculate the far field generated by the tube lens in the image or camera plane, to then propagate it along the optical axis. The resulting intensity then corresponds to the measured PSF at a given image space z-position of an object in the focus plane. This can also be understood as the PSF measured in the (in-focus) camera plane of objects at different axial positions due to the conjugate nature of the object and image spaces, where the respective z coordinates are then simply related via the axial magnification.

The model of the light field in the pupil plane is described in Section 4.4.3. The field is given by the apodization function of the objective lens (Equation 4.22) and the phase-modulated generalized pupil function (Equation 4.20), which can capture arbitrary aberrations and selected phase masks. The numerical simulation has to be performed in a discrete manner. Therefore, the pupil plane field is defined in a $1\,050 \times 1\,050$ matrix with the physical pixel size corresponding to the SLM pixel size for convenience. This is a reasonable choice, as the amplitude given by the apodization and Zernike polynomials describing the aberrations vary smoothly and relatively slowly across the pupil plane. Phase discontinuities are introduced only by the phase mask on the SLM, and in fact in discrete pixels due to the digital nature of the device.

It is also straightforward to account for the smoothening effect of the cross-talk at the boundary of adjacent SLM pixels described in Section 4.5.1 by dividing each SLM pixel into subpixels and then convoluting with a Gaussian kernel. However, the inter-pixel cross-talk turns out to have negligible effect on the PSFs obtained.

Exemplary, I present the simulation for $\mathrm{NA} = 0.3,\ 0.6$ and 0.92, for which the corresponding pupil diameters in the SLM plane are $D = 230,\ 460$ and 705 SLM pixels, as we saw in Section 4.5.2. For now, I neglect any aberrations and only add the phase of the double-helix LG mode superposition. For comparability, I choose the same waist w_0 as for the experimental measurements, for which the optimal value of $a/w_0 = D/2w_0 = 2.97$ was found. The resulting SLM plane field for the NA of 0.6 is shown in Figure 4.13 a).

The corresponding field in the image plane is given by the Fourier transform (see Appendix A.3), which can be calculated numerically using the two-dimensional discrete Fourier transform (DFT). Since the field outside the aperture is zero, the field matrix in the pupil plane can be zero-padded, i.e. symmetrically embedded in a larger matrix of zeros. In this way, the resolution of the output plane is arbitrarily increased. I choose a zero-padding factor of 10, giving a matrix of $10\,500 \times 10\,500$, as this yields reasonably good resolution in the output plane. The output plane pixel size is given by $\lambda f_{\mathrm{tube}}/d$, where d is the physical side length of the input matrix. The microscope's magnification M relates the image plane coordinates to the object or atom plane. Figure 4.13 b) shows the zoomed-in[25] resulting field in object plane coordinates, the PSF. As can be seen, the resulting intensity is similar to the target LG mode superposition (cf. Example B in Figure 4.6); two peaks surrounded by a fainter ring. The phase retains its pattern of discontinuities, but on a new radial scale, as expected. However, discrepancies can be observed. The deviations are not surprising, since we only modulate the phase, but the intensity in the pupil plane is fixed (cf. Section 4.4.3 on the PSF engineering).

The field in the image plane can now be propagated to other positions along the optical axis using the Fresnel diffraction as long as the near field conditions are satisfied. This is described in more detail in Appendix A.2. Practically, one takes advantage of the fact that the Fresnel integral can be expressed as a convolution with the so-called Fresnel kernel (cf. Equation A.12), and this can be implemented computationally efficient as a multiplication in the Fourier plane according to the convolution theorem. Both the standard PSF and the DH-PSF are shown for different axial positions and NAs in Figure 4.13 c). For ease of interpretation, the axial distance in the conjugate object or atom space is given, in units of the vertical lattice constant $\mathrm{d}z_{\mathrm{vert}} = \lambda_v/2 = 532\,\mathrm{nm}$. The simulation reveals the helical behavior of the DH-PSF. The amount of rotation strongly depends on the NA, as is expected from the LG treatment in Section 4.4.2; a high NA corresponds to a small radial and axial scale w_0 and z_{R} of the PSF in the image plane, giving a faster rotation and defocus. Note the inevitable increase in size of the DH-PSF compared

---

[25] The zoom-factor is chosen to be 50. The part of the matrix shown in Figure 4.13 thus corresponds to 210×210 pixels.

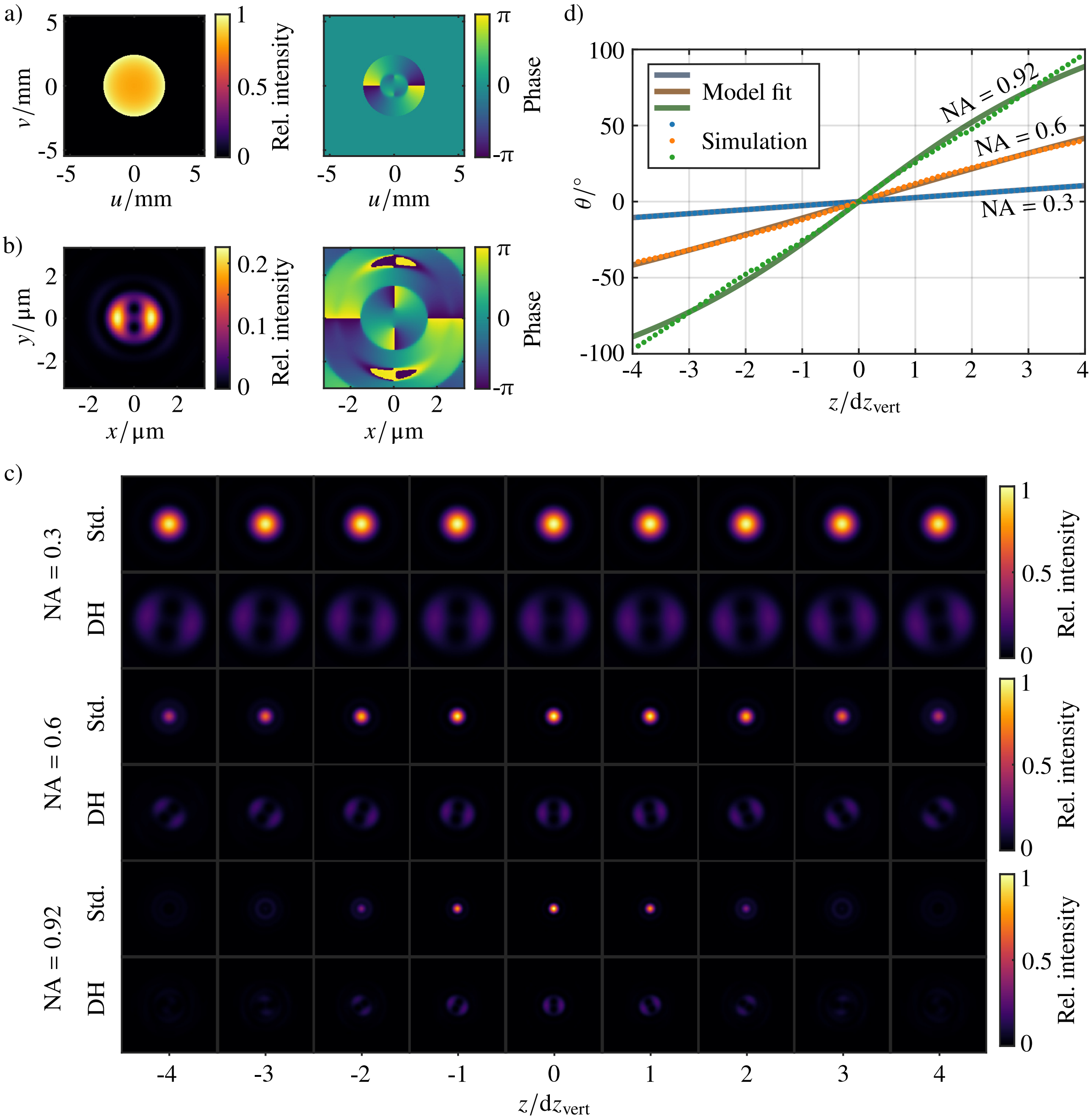

Figure 4.13: Simulation results of the DH-PSF. a) Intensity and phase in the SLM plane. The intensity normalized to its maximum increases towards the edges due to the apodization of the objective lens. b) Resulting intensity and phase of PSF in object/atom plane coordinates. Only a section of the center of the calculated output matrix is shown, so that the PSF can be easily seen. The intensity is normalized to the maximal intensity of the standard PSF. c) Intensity of the PSF field Fresnel-propagated to different axial planes in units of corresponding vertical lattice spacings $\mathrm{d}z_{\mathrm{vert}}$ for the standard (Std.) PSF and the DH-PSF at $\mathrm{NA} = 0.3,\ 0.6$ and 0.92. In all cases, the image size is chosen to be identical to the one shown in b). The intensity is normalized for each NA to the respective maximum intensity of the standard PSF. Apparent is the progressive defocus, the helical behavior of the DH-PSF and the NA dependent axial scaling of the rotation. d) Computed rotation angles and corresponding model fits of the DH-PSFs at the three NAs. For this purpose, the PSF was calculated at each of 81 axial positions in the interval from -4 to $4\,\mathrm{d}z_{\mathrm{vert}}$.

NA	MSE	$z_R/\mathrm{d}z_{\mathrm{vert}}$	$\theta(1\,\mathrm{d}z_{\mathrm{vert}})/^\circ$
0.3	0.000594	43.47 ± 0.02	2.6356 ± 0.0012
0.6	0.682	10.51 ± 0.04	10.87 ± 0.04
0.92	11.7	4.08 ± 0.04	27.5 ± 0.3

Table 4.1: Effective Rayleigh range z_R and MSE of the fitted rotation curves at different NAs of the simulated DH-PSF. For reference, the rotation angle between a lattice site in the focus to its neighbor is computed.

to the standard PSF. The dependence of the DOF on the NA (cf. Equation 4.3) can easily be seen from the standard PSF. It scales inversely quadratic with the NA.

Differences in the standard PSFs of adjacent vertical lattice planes can be observed at NA = 0.92. In this respect, at this NA axial localization with this precision is theoretically possible, which is also the conclusion from the DOF being about one vertical lattice site. Practically, however, atoms lost towards the end of the exposure time can also cause a lower brightness. Gradients of light shifts, for example due to the finite profile of the lattice beams also cause spatially slightly different brightnesses due to changed resonance conditions. This would make the vertical single-site resolution very difficult in contrast to utilizing the clear difference in the DH-PSFs. In addition, the standard PSF is symmetric with respect to $z = 0$, but this ambiguity is not present in the DH-PSF.

The rotation angle is shown in Figure 4.13 d), which is determined as I will describe in Section 4.6.2. A non-linear least squares minimization is used to fit the rotation angle to Equation 4.16 describing the expectation for a LG mode combination laying on a single line in the modal plane. The resulting effective Rayleigh distances z_R and the mean squared error (MSE) are listed in Table 4.1. As was already apparent in the plot and is also expressed in the MSEs, the smaller the NA, the better the fit of the LG model for this selected axial range. Despite the visible deviations from the targeted LG mode, we can conclude that the DH-PSF created by sole phase modulation is still quite well described by this model, in particular at low and intermediate NAs. This is partly because of the high mode fidelity, but also because leakage into other LG modes occurs symmetrically about the straight line in the LG modal plane, as was shown by Reference [73], thereby hardly influencing the rotational behavior.

This reinforces that Equation 4.16 can be a suitable model for recovering axial position from a measured PSF, despite sole phase modulation. In case of significant deviations, a LUT of axial position from the detected rotation angle can of course be established. By way of example, the rotation angle between the focus and one vertical lattice separation as obtained from the simulation is also given in Table 4.1. For all NAs investigated, this should be sufficient to be able to resolve the vertical lattice structure and thus determine the vertical plane of an atom.

Measuring the PSF outside the experiment. As a proof-of-principle, the DH-PSF was generated in a prior optical test setup outside of the experiment using the SLM. For this purpose, the SLM was illuminated by a linearly polarized laser beam at $\lambda = 852\,\mathrm{nm}$. The beam incident under a small angle is beforehand expanded to yield nearly homogeneous intensity on the SLM chip. The SLM is placed in the front focal plane of a lens of focal length $f = 300\,\mathrm{mm}$, creating the Fourier transform of the SLM output light field in the back focal plane, where a charge-coupled device (CCD) camera is placed to record the generated PSF. This setup is just a physical realization of the simulation, where the Fourier transform was implemented by a lens. It has allowed a prior generation and optimization of the DH-PSF and, like the simulation, has shown good agreement of the measured rotation angle with the expectation from the

LG mode model.

4.6 Three-dimensional localization of single atoms

The fluorescence microscope equipped with phase engineering can be used with the help of a DH-PSF to localize single atoms in the three-dimensional optical lattice along all three dimensions. Images of axially thick atomic ensembles of a sparsely filled optical lattice are used to characterize the modified PSF and test the three-dimensional localization. I describe how these are recorded in Section 4.6.1, and how the atoms are detected in Section 4.6.2. Section 4.6.3 describes the required calibration of the axial rotation; a certain rotation angle needs to be assigned to the corresponding axial position. I then conclude by demonstrating the resolution of the vertical lattice in Section 4.6.4.

4.6.1 Imaging the lattice with the engineered PSF

The experimental sequence to load and then image atoms in the optical lattice remains largely unchanged from previous experiments, as those presented in References [17, 18, 84]. In the following, I describe the sequence with a focus on the differences and additions to the typical sequence described in Section 2.1. In particular, I describe how the SLM is controlled throughout the sequence.

The experimental sequence. The phase mask on the SLM is set. After loading the MOT from the dilute background vapor, it is moved by shifting the magnetic trap to the position of the dipole trap. There, the optical lattice is turned on and the MOT beams are turned off, causing the atoms to transfer into the lattice. No state preparation, and no vertical selection of atoms is performed. The lattice is thereby filled with many atoms, such as in Figure 4.11 a). To obtain a sparsely filled lattice, a waiting time of 4 s is used, resulting in an adjustable loss due to the finite lifetime of the atoms in the lattice.[26] The atoms are then molasses cooled by being illuminated with the PGC beams. They are subsequently imaged by illuminating them with PGC beams within the camera's exposure time, which cools them and causes them to fluoresce. For a sufficient SNR at NA = 0.6 an exposure time of 1 s is necessary. The fluorescence light passes through the microscope onto the camera and, depending on the SLM setting, forms an image of the atoms with the corresponding PSF. After closing the camera shutter, a new phase pattern is loaded onto the SLM within a 500 ms window, ensuring that the SLM is correctly set for the second image. A second image of the atoms is taken, followed by a third after another change of the SLM phase mask. All atoms are then pushed out by a resonant beam in order to take a background image with the same settings as the previous images. The sequence is then repeated with the loading of a new MOT. Each run takes about 9 s without the hold times for the SLM, the exposure times and the waiting time for a sparsely filled lattice. Including these results in about 18 s.

Controlling the SLM. Timing the SLM is of importance if the phase pattern is changed within a sequence. The desired phase masks are created in advance. The experiment control on the laboratory computer[27] programs the digital and analogue real-time processing systems (see Section 2.3.3). Trigger signals programmed into the sequence are sent to a second computer controlling the SLM when the

---

[26] Here, the sequence could be shortened by partially heating out through resonant beams and subsequent cooling of the surviving atoms instead. This was however discarded due to time constraints.

[27] Implemented in MATLAB.

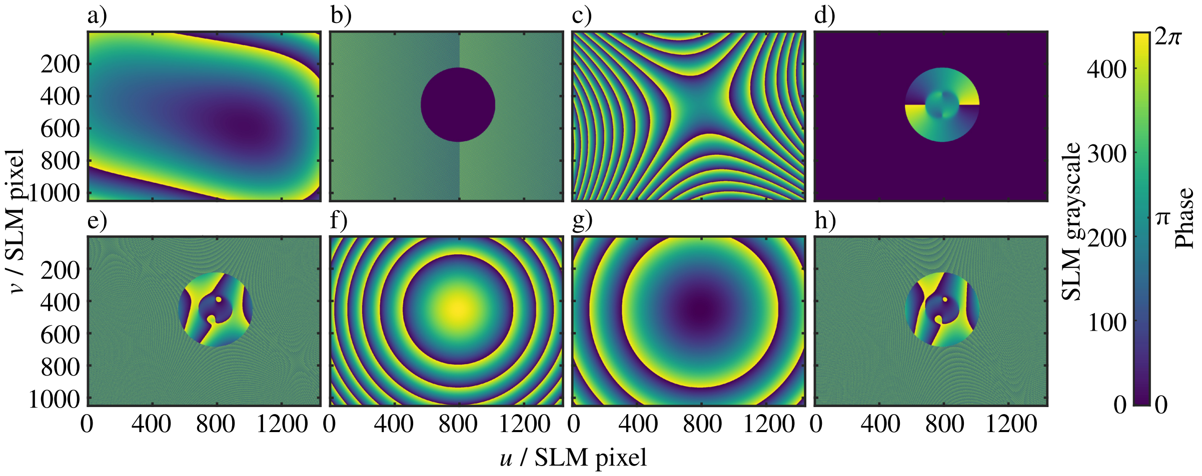

Figure 4.14: Phase masks programmed on the SLM. a) Curvature compensation mask. b) Aperture-defining blazed grating with a period of 6 pixel. c) Zernike polynomials for aberration compensation. d) DH-PSF phase mask. e) Superimposition of all phase masks a) to d). f) Holographic lens with $f_{\mathrm{hol}} = 7.4\,\mathrm{m}$. g) Holographic lens with $f_{\mathrm{hol}} = -14.8\,\mathrm{m}$. h) Superimposition of all phase masks a) to d) and the holographic lens g). It should be noted that the phase ramps originating from the blazed gratings may not be discernible or moiré patterns may appear due to the small period.

phase pattern is to be changed. This computer waits for a trigger[28] and then changes the video signal sent to the SLM driver accordingly.

The overall delay and settling time for the response of the SLM was assessed by adding to the second image's phase mask a blazed grating shifting the image with respect to the previous shot. The SLM trigger is sent immediately after an image is taken. The following image is taken after a certain hold time. By gradually decreasing the hold time, the time at which the image shift is not yet complete can be determined. This is the minimum time that must be waited between two images. I estimated 400 ms, which is why I chose a slightly longer hold time of 500 ms in the sequence, in order to account for the variability of different phase patterns. I attribute the longer response time compared to the typical 100 ms given by the manufacturer to delays in receiving and processing the trigger signal from the SLM controlling computer and in switching the video signal sent to the SLM.

The SLM phase mask. The phase masks of different purposes are displayed together on the SLM by adding them modulo 2π. The individual phase masks and the resulting total mask are shown in Figure 4.14, exemplary at NA = 0.6 (i.e. with an aperture diameter of 460 pixel, see Section 4.5.2). When the SLM is off, it acts as a mirror with poor flatness. In all cases, therefore, the curvature compensation mask shown in Figure 4.14 a) is displayed, which flattens the phase response (see Section 4.5.1). The aperture-defining blazed grating outside the aperture is shown in Figure 4.14 b). For all measurements, the Zernike polynomials shown in Figure 4.14 c) are displayed for aberration compensation (see Section 4.5.2). The Zernike coefficients were determined at full NA, and are therefore tied to that specific aperture size. Finally, the LG mode superposition phase of the DH-PSF is added, see Figure 4.14 d). According to the optimal ratio a/w_0, the waist is chosen as $w_0 = 77.3$ SLM pixels

---

[28] A MATLAB script is running, which waits for an incoming trigger read by a I/O device (National Instruments USB-6000).

(cf. Section 4.5.3). All phase masks account for the shift of the optical axis relative to the SLM chip center by −72 vertical and 70 horizontal SLM pixels. In addition, the geometrically determined angle of incidence of $\alpha = 2.9^\circ$ onto the SLM is compensated by stretching the phase mask along the u-axis, which is given by the intersection of the SLM surface and the plane of incidence. The stretching is realized by scaling all physical lengths along the u-axis with $\cos(\alpha)$. It is hardly visible in the phase masks due to the nearly vertical angle of incidence.

Shifting the plane of focus. The SLM can also be used to change the focus of the microscope. This can be understood as a controlled insertion of a defocus aberration, or equivalently as programming a holographic lens or Fresnel lens of focal length f_hol located in the SLM plane. It is simply a quadratic phase

$$\varphi_\text{hol}(u,v) = -k\frac{u^2+v^2}{2f_\text{hol}} \mod 2\pi\,, \tag{4.31}$$

where $k = 2\pi/\lambda$ [119]. Figures 4.14 f) and 4.14 g) show such holographic lenses for different focal lengths. Figure 4.14 h) shows the addition of a holographic lens to the previous phase mask. The focal plane is shifted by $\Delta z_\text{I} = -f_2^2/f_\text{hol}$ in the intermediate image plane, which corresponds to a shift

$$\Delta z = \frac{f_\text{obj}^2 f_2^2}{f_1^2 f_\text{hol}} \tag{4.32}$$

in the object space. The derivation is shown in Appendix C.4. A focal length of $f_\text{hol} = 29.9\,\text{m}$ is required to shift the focus by, for example, one vertical lattice site, i.e. by 532 nm.

As we will see, moving the focal plane between subsequent images of the same atoms is an efficient way to perform the axial localization calibration. This method is technically significantly easier to implement than, for example, piezo control of the objective lens as reported in Reference [74].

4.6.2 Detecting atoms by their DH-PSF

The EMCCD camera provides images in the form of detected fluorescence photons, which are integrated pixel by pixel over the exposure time. The camera converts the incident photons into electrons with a quantum efficiency of 63 % at the imaging wavelength $\lambda_\text{D2} = 852\,\text{nm}$. The electron registers can be amplified, hence EM for electron multiplication. Using the fluorescence images, the position of the atoms can be determined. The common method of identifying the atoms based on the image's local maxima and approximating the PSF as a Gaussian peak evidently needs to be modified when using a DH-PSF. Therefore, in the following I present how the atoms measured with the DH-PSF are detected, the PSF is modelled and the rotation angle is extracted. I also show and comment an example of measured PSFs.

Preprocessing. The images contain a background which does not originate from the fluorescence photons, but from unsought scattered light and camera noise. In order to correct the images, a background image is always taken in each sequence run. This consists of an image taken with the exact same experimental parameters as the previous images in the sequence, but a push-out beam ensures beforehand that no atoms are left in the lattice. For each set of experimental parameters, a mean background image is created so that shot noise is statistically suppressed. This is then subtracted from each individual image. Figure 4.15 a) shows the gray value histograms of the raw atom images, the background images, and the

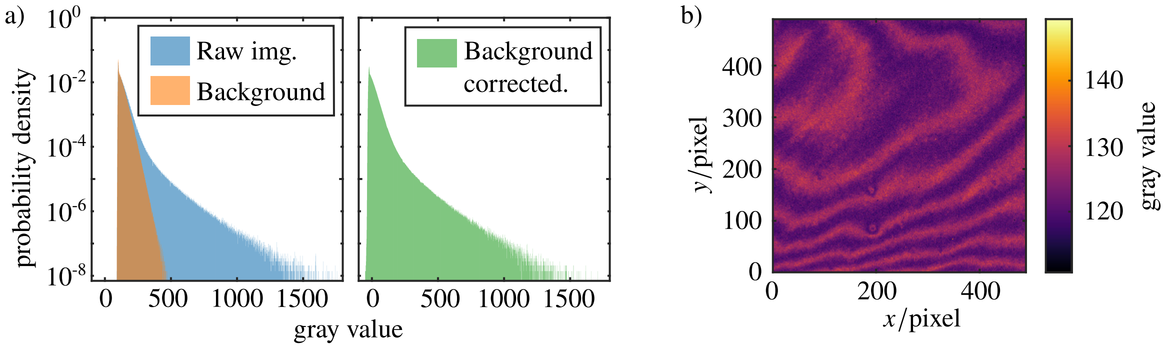

Figure 4.15: a) Example of gray value histograms of raw atom images (blue), background images (orange) and mean-background corrected images (green). The atom image histograms consists of 1 800 frames taken at NA = 0.6 with the DH-PSF, the background histogram consists of 600 frames. The probability axis is logarithmic. The histograms are truncated at a gray value of 1 800. Occasionally, brighter pixels due to cosmic ray events do occur. b) Corresponding mean background image over 600 frames. Etaloning stripes are noticeable, as well as two rings caused by dust grains presumably on the filters.

atom images after mean background subtraction. The read noise maximum at the bias level of 100 gray values can be observed, followed by the tail consisting of signal and noise. The subtraction of the mean background leads to a reduction of the noise. Figure 4.15 b) shows the corresponding mean background image. The visible stripes originate from etalon interference effects typical of back illuminated EMCCD cameras in the near infrared. These are caused by back and forth reflections within the depletion region, which cannot be completely avoided due to the imperfections of the AR coatings at this wavelength. This is how a static spatially inhomogeneous sensitivity arises, which can be compensated for by multiplying acquired images by the inverse sensitivity. An inverse sensitivity mask can be created by a low-pass filtered mean image of many frames taken with a homogeneous illumination. For our purposes, however, the spatially rather slowly modulated sensitivity is not a problem, as we are not interested in absolute brightness. The etaloning is therefore ignored. In rare cases, cosmic rays cause a very bright and localized cluster of pixels up to camera saturation. Background images with such events are sorted out beforehand by a brightness threshold.[29]

Example PSF measurement. Figure 4.16 shows sections of typical images of the sparsely filled lattice at NA = 0.6 with standard PSF and DH-PSF, respectively. Atoms with similar standard PSF show a clear angle difference in the DH-PSF. In this example, the DOF enhanced by the DH-PSF can be observed very well; even atoms that look blurry with the standard PSF can be localized well based on the DH-PSF. Furthermore, this example demonstrates again that the symmetry of the standard PSF with respect to $z = 0$, which is problematic for an axial localization, does not apply to the DH-PSF. It is noticeable that the in-focus rotation angle is not zero with respect to the horizontal as expected, which we will come back to later. Also, this example shows a disadvantage of the DH-PSF, namely that the energy is split between two peaks, giving a poorer SNR compared to the standard PSF. Ultimately, further studies must be conducted to determine the extent to which this affects the gained resolution given the noise present here. As was discussed in Section 4.4.4, References [75, 83, 137] have indeed

---

[29] A threshold of 500 gray values is chosen which is above the regular background pixel brightnesses at the parameters used, and below the bright cosmic ray pixels.

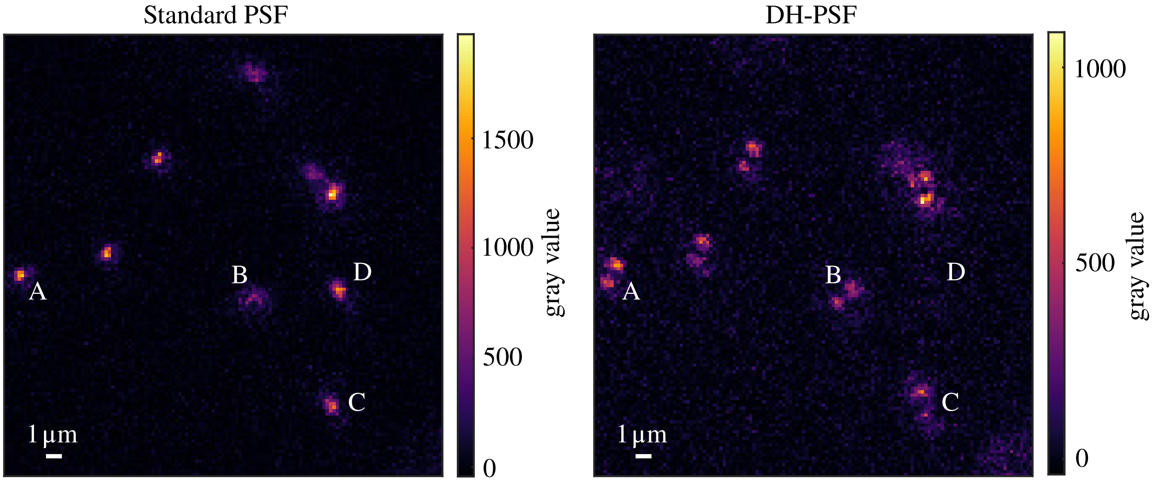

Figure 4.16: Example of an image section taken with the standard PSF (left) and the DH-PSF (right). The (background corrected) images at NA = 0.6 with an exposure time of 1 s have been consecutively taken from the same ensemble of atoms. Note the different color scale as a result of the reduced SNR for the DH-PSF. Atom A appears relatively in focus, while atom B is clearly out-of-focus, resulting in a different angle. Atom C also appears moderately defocused, but based on its DH-PSF angle it can be concluded that, unlike atom B, it is located below the focal plane. Atom D shows an example of an atom that is lost. The length scale in the object space is indicated.

shown an improved three-dimensional resolution in the presence of typical noise.

Detecting and pairing peaks. Figure 4.17 a) shows an example of a full image taken with the DH-PSF. I specifically chose a slightly fuller lattice, as this defines the challenge of determining the position. In the case of the DH-PSF, as for the standard PSF, the peak positions are obtained from the local maxima. To avoid maxima caused by noise, the images are first smoothened with a Gaussian filter. This is implemented using the convolution theorem as a multiplication in Fourier space, see Figure 4.17 b). The filter kernel width is chosen as the Abbe cut-off frequency[30] (cf. Equation 4.2 in Section 4.2.2). This suppresses high frequency noise and avoids loss of physical information. To find the local maxima of an image, the pixels are determined where all eight neighboring pixels have a lower value.[31] In addition, the image is thresholded beforehand, so that maxima in the background are disregarded and the computation performance is increased. The resulting image on which the local maxima are searched is shown in Figure 4.17 c). The threshold is selected based on typical peak amplitudes.[32] As an additional condition for the peak search, any island above threshold is required to have a certain area, as is expected for a PSF having a certain width.[33] This way, isolated bright pixels are not taken into account. An edge region of 12 pixels is ignored so that only fully captured PSFs are detected. In the given example, we find the maxima marked as crosses in Figure 4.17 d).

---

[30] At NA = 0.6, the Abbe cut-off frequency is $k_{\text{Abbe}} = 1/r_{\text{Abbe}} = 1.4\,\mu\text{m}^{-1}$. This corresponds in the DFT of the 489 × 489 image to the spatial frequency $0.18\,\text{pixel}^{-1}$, or 88 Fourier pixels.

[31] I used the algorithm written by Adi Natan, *Fast 2D peak finder* (`https://github.com/adinatan/fastpeakfind/releases/tag/1.13.0.0`), GitHub, 2013, Retrieved November 15, 2022, in a version modified by Otto Eliasson without the filtering procedures.

[32] For the DH-PSF at NA = 0.6 I chose the threshold of 180 gray values.

[33] For the DH-PSF at NA = 0.6 I chose a minimum of 10 pixels.

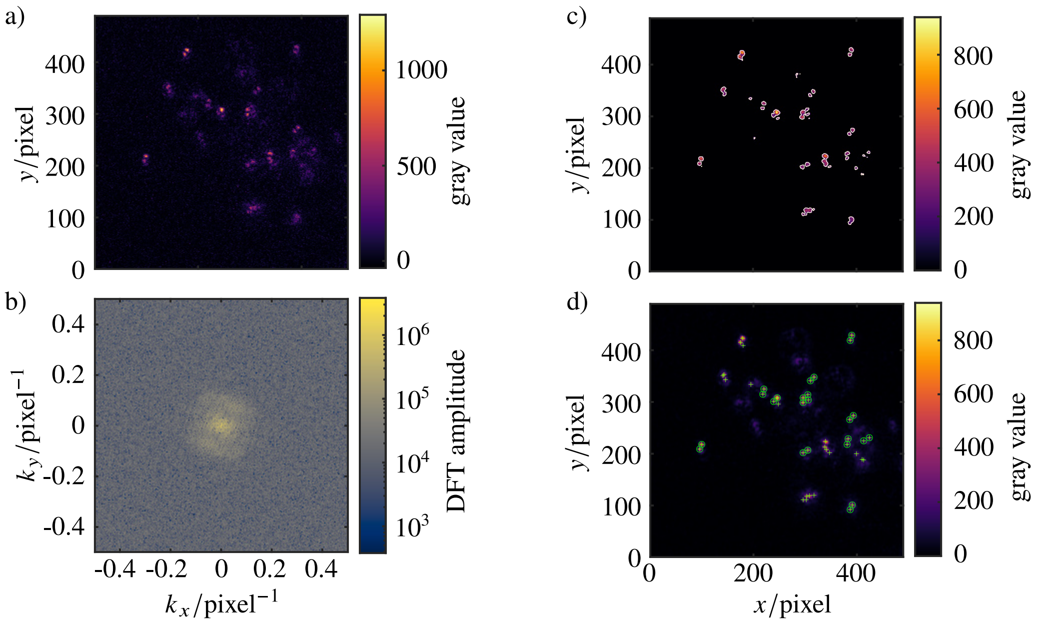

Figure 4.17: a) Example frame of a sparsely loaded lattice imaged with the DH-PSF at NA = 0.6. b) DFT of the image shown in a). The colormap is logarithmic. Physical information is contained in a radius of 0.18 pixel^{-1}, corresponding to the Abbe cut-off frequency. c) Filtered and thresholded image. The islands above the threshold of 180 gray values are demarcated by a white line. d) Filtered image with marked detected peaks (+) and identified atoms as paired peaks (○). In this example, a total of 44 peaks are detected, of which 24 are successfully paired to 12 atoms. Most of the unpaired peaks remaining are in regions with closely packed atoms, where the algorithm used cannot establish a unique pairing.

However, in the case of the DH-PSF, not only the peak location, but in particular the information about the pairing of the peaks constituting the PSF of a single atom is required. To obtain that information, the pairwise separation of all peak combinations in an image is calculated. From these, only those pairs are kept which are within a given distance range. The range is set by manual inspection of the detected PSFs.[34] Then, those pairs are sorted out in which at least one of the two peaks is also paired with yet another peak. This gives us unambiguous peak pairs, which by construction correspond to one atom each. In Figure 4.17 d), the detected pairs are marked as circles.

For sequences in which the same atoms are acquired multiple times (e.g. with different SLM settings), only the first image is scanned for atoms. Atoms will be found in the same place in subsequent images, will be lost, or will hop a short distance. However, no atoms will appear at substantially other locations. For the subsequent images, the localization algorithm is therefore limited to a region of interest (ROI) around the detected positions from the first image, saving considerable computation time.

Sub-pixel localization. Taking the pixel of the local maximum of a peak as its position, despite the spatial sampling of the camera, does not exploit all the positional information available. In the case of the standard PSF, a Gaussian peak is commonly fitted to a ROI containing the peak, with the initial position estimate as the previously established pixel position. In this way we get the position sub-pixel

---

[34] For the DH-PSF at NA = 0.6, I chose a minimum of 8 and a maximum of 14 pixels distance.

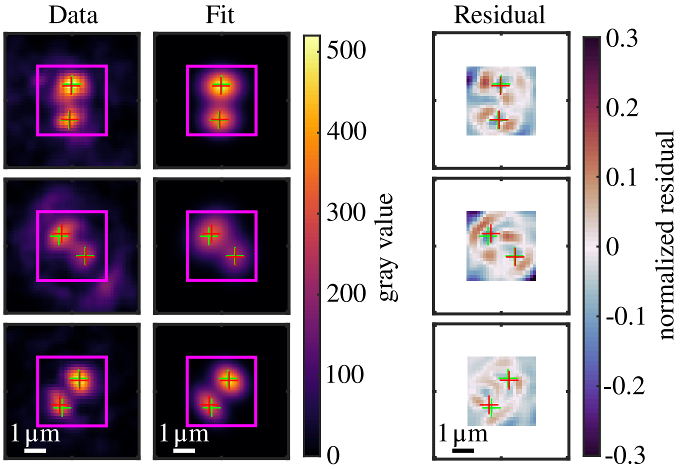

Figure 4.18: Examples of sub-pixel double Gaussian peak fits. The first column shows the filtered data (DH-PSF at NA = 0.6), the second column the resulting fit and the third column the normalized residual, namely the difference of fit and data normalized to the maximum of the fit. The previously determined peak maxima pixel positions (+) and the determined sub-pixel peak positions (+) are marked. The fit is performed in a 21 × 21 pixels area (□) of the 41 × 41 pixels ROI. The length scale in the object space is indicated.

resolved. This approach is in principle also possible for the DH-PSF, with two Gaussian peak fits per atom. Due to the partially overlapping peaks in the DH-PSF, the fit may be distorted by the other peak. Therefore, as a model for the measured DH-PSFs, the sum of two Gaussian peaks is used instead. To account for the incomplete symmetry of the peaks in contrast to the standard PSF, an elliptical degree of freedom is given. Figure 4.18 shows three examples of such fits. As initial estimates, the pixel positions of the peak maxima are used for the position and the associated gray value for the amplitude. For the axis angle of the elliptical two-dimensional Gaussians, the rotation angle determined from the pixel positions is used as the initial estimate, given that the ellipticities are usually orthogonal to the line connecting the two peaks. All widths are initially estimated with the same heuristic value.[35]

Dictionary of detected atoms. A dictionary is compiled from the information on the detected atoms. For each atom, it contains the run and image number of the sequence it was detected in, the peak pixel positions, the Gaussian peak fit results in particular with the sub-pixel positions, and a cropped image of a ROI around the center pixel.[36] The center pixel of a DH-PSF is calculated by the vectorial mean of the peak pixel positions. In the same way, the sub-pixel position of the atoms is computed from the fitted peak positions. The rotation angle with respect to the abscissa $\tilde{\theta}$ is calculated from the relative peak positions, i.e.,

$$\tilde{\theta} = \arctan\left(\frac{\Delta y}{\Delta x}\right) , \tag{4.33}$$

---

[35] For the DH-PSF at NA = 0.6 the widths are estimated as 2.5 pixels.

[36] The ROI size is chosen depending on the PSF size. It was chosen as 41 × 41 pixels for NA = 0.6. The ROI is centered on the center pixel.

with the position differences Δy and Δx. Similar to creating the mean background image, cosmic ray events are sorted out by defining a maximum brightness for individual pixels.[37] The $\approx 0.4\,\%$ of ROIs containing such pixels are simply discarded.

4.6.3 Calibrating the axial localization

The mapping of the rotation angle extracted from a PSF to the vertical position is in theory directly possible using Equation 4.16, as long as the Rayleigh length z_R of the LG mode superposition in object or image space is known. However, we define the z_R of the mode combination by choosing the LG waist w_0 in the pupil plane, wherein only the scale of the phase, not of the unmodulated amplitude is set (cf. Section 4.4.3). The resulting field in the image space has high overlap with the desired LG mode superposition, but here the w_0 or z_R defining the LG basis are unknown *a priori*.[38] Even with knowledge of the effective Rayleigh length z_R, a calibration of the vertical position would be desirable to account for influences of experimental effects not captured in the simple model, such as aberrations.

A vertical length reference is required for calibration. This is given, for example, by shifting the focal plane by a known distance, which we can do by programming a holographic lens (see Section 4.6.1). I took images of sparsely filled lattices as described in Section 4.6.1, each with three images of the same ensemble of atoms, programming the SLM with a holographic lens in the second image. An example ROI of an atom in these three images is shown in Figure 4.19 a). The change in the measured angle of the second image $\tilde{\theta}_2$ compared to the first image $\tilde{\theta}_1$ or third image $\tilde{\theta}_3$ can thus be related to the displacement of the focal plane. The comparison between the first and third images taken with the same settings gives insight into detrimental effects such as vertical hopping. Measurements were made with the four focal lengths $f_{\mathrm{hol}} = \pm 14.8$ and $\pm 7.4\,\mathrm{m}$, which correspond to shifts of the focal plane by roughly ± 2 and ± 4 vertical lattice planes, or more precisely ± 2.0186 and $\pm 4.0372\,\mathrm{d}z_{\mathrm{vert}}$. For each focal length, 600 respectively 200 sequence runs are acquired. The intermediate NA of 0.6 is used because, compared to the maximal NA, both the axial resolution through the standard PSF and the rotation angle per vertical lattice plane of the rotating PSF are smaller, thereby posing a greater challenge. Furthermore, the reduced solid angle also means a smaller SNR. Thus, the demonstration of the use of the DH-PSF at the more common intermediate NA = 0.6 is of greater relevance.

The atoms are detected and listed in a dictionary as described in Section 4.6.2. Before creating the calibration fit, vertically hopped, lost between successive images or incorrectly detected atoms must be filtered out.

Filtering of lost, hopped and incorrectly detected atoms. The post-selection described in the following consists of: ① the selection of atoms detected in all three frames; ② removing outliers due to vertically hopped atoms or incorrect atom detections; ③ restricting to a central area of the FOV.

During the experimental sequence, some atoms are lost from the lattice due to background collisions. When this occurs, the atom detected in the first image is missing in further images. If the atom is lost during the exposure time, it appears in the corresponding image with a lower brightness. Figure 4.19 a) shows the total number of atoms detected for each frame number, with the expected exponential decrease. Only the atoms detected in all three images are used for calibration. This portion is color-coded in the

---

[37] A threshold of 2 000 gray values is chosen which is above the maximal signal pixel brightnesses at the parameters used (cf. Figure 4.15), and below the bright cosmic ray pixels.

[38] From the numerical simulations, this scale could be determined by maximizing the projection onto the target LG mode superposition under variation of w_0.

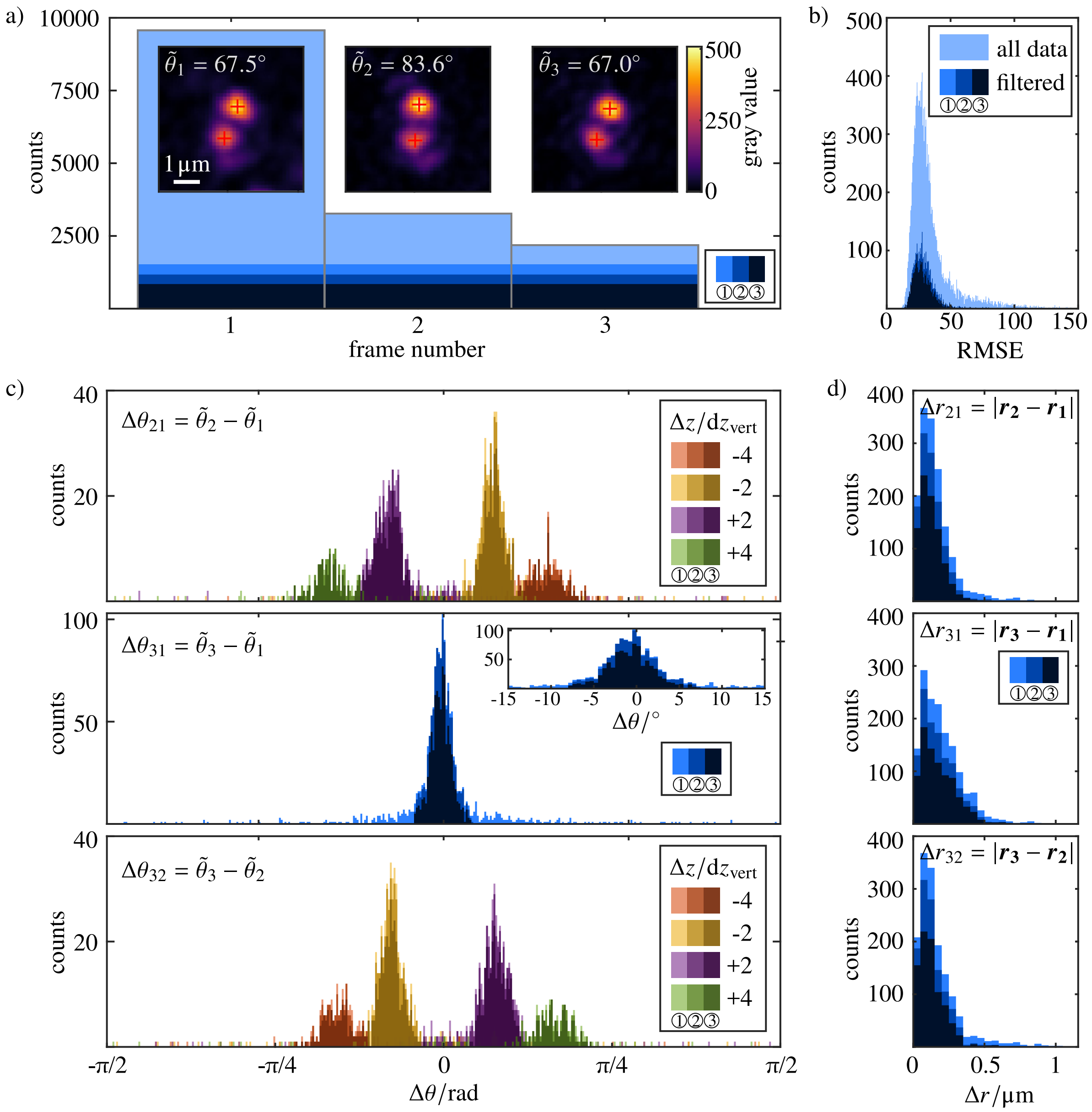

Figure 4.19: Example images and distributions of parameters relevant for the selection of atoms for axial calibration. In different color shades are the remaining distributions after selecting the atoms detected in all three images ①, filtering vertical hopping and incorrectly detected atoms ②, and limiting to a central region of the FOV ③. a) The ROI and the detected angles $\tilde{\theta}$ of an example atom with a focus shift of $\Delta z = -2\,\mathrm{d}z_\mathrm{vert}$ in the second frame, as well as the number of detected atoms for the each frame number. b) Distribution of the root mean squared error (RMSE) of the sub-pixel fits. c) Distributions of angle differences between two images for the different focal shifts $\Delta z = \pm 2.0186$ and $\pm 4.0372\,\mathrm{d}z_\mathrm{vert}$. By design, there is no shift in focus between frames 1 and 3. d) Distributions of the measured position differences between two frames.

figure as marked by ①. It does not correspond to the total number of atoms detected in the third image, because in some cases the atom imaged with modified focus is not detected in the second image. Figure 4.19 b) shows the distribution of the goodness of fit. There is a clustering in a certain range around the RMSE of 30, followed by a tail towards large deviations of the fit model.

Atoms can also hop from one lattice site to the next. If the atom hops horizontally, its position in the image changes, if it hops vertically, this is manifested in a different rotation angle of the DH-PSF. To detect vertical hopping, the angle difference between each image is considered. Its distributions are shown in Figure 4.19 c). As can be seen from the spread of angle differences between the first and third image $\Delta\theta_{31}$, which ideally should be zero, there is clearly vertical hopping. This can be attributed to insufficient cooling of the atoms or a too shallow lattice along the vertical (cf. Section 3.1). Anticipating the results of the calibration, 8.0° corresponds to one vertical lattice spacing away from the focus. Ten more lattice sites away, the angular difference between two planes is still 5.2°. In fact, sidelobes can be seen in the distribution in this range (cf. the inset in Figure 4.19 c)) and are caused by atoms that vertically hopped between the images. If an atom hops vertically within the exposure time, this leads to an additive contribution to the initial PSF by the PSF correspondingly rotated relative to it. This yields a measured PSF angle corresponding to an effective position between the hopped and initial positions of the atom. The statistical nature of hopping thus leads to smearing of the distribution of angle differences. The nonlinearity of the relationship between position and angle results in an additional broadening. This is all the larger, the greater the effective vertical distance between the respective images. Therefore, for $\Delta\theta_{21}$ and $\Delta\theta_{32}$, the distributions for $\Delta z = \pm 4\,\mathrm{d}z_{\mathrm{vert}}$ are wider than for $\pm 2\,\mathrm{d}z_{\mathrm{vert}}$.

It can also be seen that the distribution of $\Delta\theta_{31}$ is not exactly centered at 0°, but rather at the median of -0.63°. A shift is also present in the distributions for $\Delta\theta_{21}$ and $\Delta\theta_{32}$. There, the average of the medians of the sub-distributions of $\pm 2\,\mathrm{d}z_{\mathrm{vert}}$ give the shifts -0.43° and -0.18°, respectively. This can be attributed to the preferred downward vertical hopping direction due to gravity. The displacement is greatest for $\Delta\theta_{31}$, since here the atoms have more time and thus fall further on average. The scattered outliers in the angle difference distributions are due to incorrectly detected peak pairs, such as when a peak is paired with a detrimental sidelobe maxima from aberrations. Such cases inherently have a high RMSE. In principle, these can be avoided by improved detection algorithms. However, this is not of concern here, as these cases are easily filtered out.

Vertical hopping obstructs the knowledge about the effective vertical distance between the respective images and thus complicates axial calibration. However, the vertical length reference introduced into the system for calibration, the focal plane shift, is significantly greater than the effective hopping distance. This allows to statistically establish a calibration in the way as described below, including consideration of the bias due to the preferred hopping direction.

To exclude far vertically hopped atoms and failed peak detections the $\Delta\theta_{31}$ distribution is truncated by 10 % percentiles on both sides; for $\Delta\theta_{21}$ and $\Delta\theta_{32}$, 4 % percentiles each. This results in the distributions indicated by ② in Figure 4.19. It can be seen that, as expected, the scattered outliers and the tail towards large RMSE disappear.

Horizontal hopping can be detected by shifts of the PSF center. For this purpose, the difference of the atom positions between images is shown in Figure 4.19 d). As can be seen, only few atoms hop by the horizontal lattice constant $\lambda_h/\sqrt{2} = 612\,\mathrm{nm}$ or diagonally in the square lattice by $\lambda_h = 866\,\mathrm{nm}$ (see Section 2.3.2 for details about the lattice structure). The width of the distributions stem from the positional uncertainty of the detection method, but is also broadened by hopping within the exposure time, as in the case of vertical hopping. Since images 1 and 3 are separated by a longer period of time, there is a higher hopping probability between them, which results in the wider distribution. Quantitatively, by setting a limit at half the lattice constant $\Delta r > 306\,\mathrm{nm}$, we can say that 8 % of the atoms hopped horizontally between images 1 and 2, 11 % between images 2 and 3, and 18 % between images 1 and 3. Since atoms can also hop back, the percentages between the subsequent images are not expected to sum to the percentage between image 1 and 3. Horizontal hopping is however not problematic for vertical position calibration, as the rotation angle remains unchanged. The distributions of the position differences also demonstrate that the horizontal localization precision from the DH-PSF does not affect the single-site resolution, at least for isolated atoms.

When creating the calibration, it was noticed that atoms in the edge region of the FOV have PSFs with systematically different rotation properties, which I will discuss in more detail in Section 4.6.4. Therefore, only atoms in a central region of the FOV are considered. The resulting distributions are indicated by ③ in Figure 4.19. The central region is defined by a circle of 130 pixels or 16.6 µm of radius centered around a point that is shifted by 5.5 and 45.5 pixels or 0.7 µm and 5.8 µm along the x and y axes with respect to the center of the images. This choice is also motivated in Section 4.6.4.

Calibration fit. The axial length reference introduced for calibration, the focal plane displacement, corresponds for the measured angles to an effective relative displacement of the atoms by this distance. For the programmed DH-PSF phase mask, we theoretically expect the measured angle $\tilde{\theta}$ of the connecting line of both peaks with respect to the abscissa to be equal to the rotation angle with respect to the focal plane $z = 0$

$$\theta = V \arctan\left(z/z_\mathrm{R}\right) \tag{4.34}$$

(Equation 4.16 from Section 4.4.2). Experimentally, however, we do not know their connection

$$\beta := \tilde{\theta} - \theta \tag{4.35}$$

a priori, which is why we introduce this as a free fit parameter.

In the following, we define the zero position of the z-dimension as the focal plane of images without shift of the focus. Next, we relate the measured angle in the unshifted images

$$\tilde{\theta}_u = \beta + V \arctan\left(z/z_\mathrm{R}\right) \tag{4.36}$$

to the angle in the image focus-shifted by Δz

$$\tilde{\theta}_s = \beta + V \arctan\left(\frac{z - \Delta z}{z_\mathrm{R}}\right) , \tag{4.37}$$

giving by insertion of Equation 4.36 into Equation 4.37 the relationship

$$\tilde{\theta}_s = \beta + V \arctan\left(\tan\left(\frac{\tilde{\theta}_u - \beta}{V}\right) - \frac{\Delta z}{z_\mathrm{R}}\right) . \tag{4.38}$$

Finally, the experimental data sets with different shifts Δz are fitted to this model by non-linear least squares minimization. Both the data pairs where $\tilde{\theta}_u$ corresponds to frame 1 and those where $\tilde{\theta}_u$ corresponds to frame 3 are included. Furthermore, for $\Delta z = 0$, the data pairs $(\tilde{\theta}_1, \tilde{\theta}_3)$ are taken. The rotation angle factor is given by the mode combination as $V = 2$. The result is shown in Figure 4.20. The measured angles follow the model quite well. The nonlinearity determines the offset angle $\beta = (34.0 \pm 1.4)^\circ$, the separation between stripes of equal Δz the Rayleigh length $z_\mathrm{R} = (14.39 \pm 0.11)\,\mathrm{d}z_\mathrm{vert}$. Due to vertical

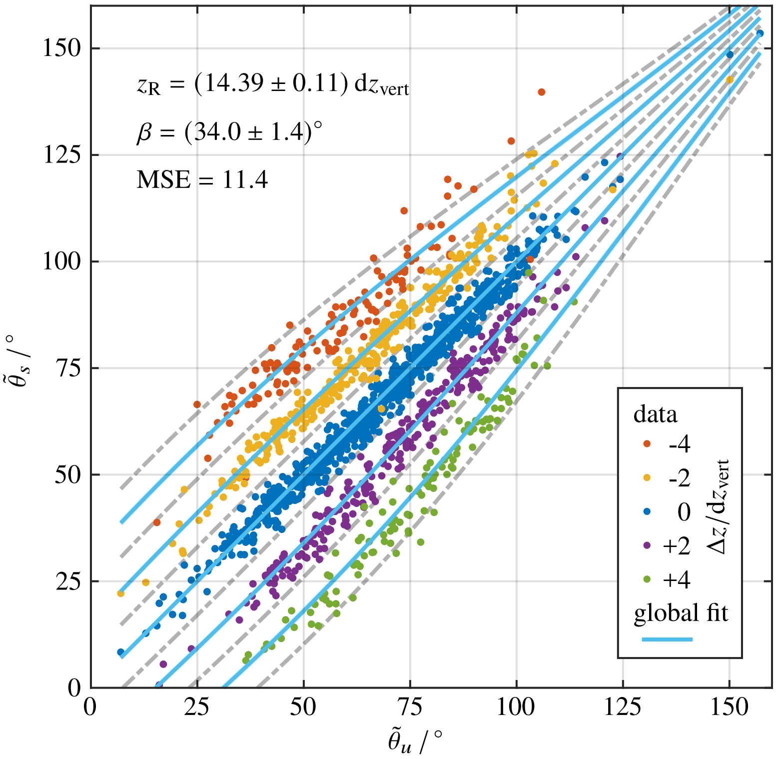

Figure 4.20: Axial calibration fit giving the effective Rayleigh range z_R, the angle offset β and the MSE. The angle measured in the image with shifted focal plane $\tilde{\theta}_s$ is related to the angle measured in the unshifted images $\tilde{\theta}_u$ by Equation 4.38. Different focal plane shifts Δz are shown in different colors. The lines corresponding to odd integer focal shifts in units of the vertical lattice constant are marked in gray dashed lines.

hopping, the data points are scattered around the fit lines corresponding to a particular vertical plane, which is also evident from the MSE of 11.4 despite the good description of the curve shape.

I expect that a reduction in vertical hopping will result in measured angles lying closer to the relevant lines, making the separation of the planes in question clearer. However, the prediction of the calibration parameters remains unaffected by the statistical spread. Systematic errors, for example due to limited accuracy of the focus shift through the holographic lens (the axial length reference) cannot be excluded. Because the fit includes both the $(\tilde{\theta}_1, \tilde{\theta}_2)$ and $(\tilde{\theta}_3, \tilde{\theta}_2)$ data pairs, angle shifts caused by gravity and the resulting directional vertical hopping are statistically cancelled out, as the shifts happen in opposite directions each. This is not true for $\Delta z = 0$, since here $(\tilde{\theta}_1, \tilde{\theta}_3)$ are taken as data pairs, which as we saw is expected to cause a systematic shift of the data points of around 0.63° below the identity line $\tilde{\theta}_s = \tilde{\theta}_u$. Upon closer inspection, a higher density of the blue points below the identity line can indeed be discerned in Figure 4.20. However, this does not affect the fit since Equation 4.38 yields the identity without free parameters for $\Delta z = 0$.

The determined angle β differs strongly from the value of 0° expected from the simulation of the DH-PSF (see Section 4.5.3). However, by including Zernike polynomials in the pupil plane in the simulation, it can be shown that certain (low order) aberrations can have a strong influence on this offset angle, namely vertical astigmatism, spherical aberration and secondary vertical astigmatism. This was also reported in Reference [170]. For instance, assuming an RMS wavefront error of $\lambda/2$ each, the offset angles $\beta = -12.4^\circ$, -28.8° and 23.3° are obtained respectively. This indicates that residual aberrations are still present after manual aberration compensation (cf. Section 4.5.2), and cause this offset angle. The other low-order Zernike polynomials (up to a total of 13), apart from the trivial case of defocus aberration, do not change β. The simulation also suggests that the uneven distribution of the intensity in both peaks observed in the experiment (see e.g. Figure 4.19 a)) may be caused by oblique trefoil.

Also the Rayleigh length differs from the value $z_\mathrm{R} = (10.51 \pm 0.04)\,\mathrm{d}z_\mathrm{vert}$ obtained in the simulation without aberrations (cf. Table 4.1). As the simulation shows, the higher value can be caused by aberrations. In particular, oblique secondary astigmatism comes into question, since this increases the effective Rayleigh distance of the rotation curve to a particular extent in contrast to the other low-order Zernike polynomials. If we take again the RMS wavefront error of $\lambda/2$, the simulation yields $z_\mathrm{R} = (18.32 \pm 0.05)\,\mathrm{d}z_\mathrm{vert}$. It is also noteworthy that this aberration focuses the energy more strongly into both main peaks and diminishes the ring-shaped structures in the DH-PSF (cf. the simulated PSF in Figure 4.13 a)), which is a desired effect. Thus, it is possible that the manual optimization performed to reduce existing aberrations left such PSF-improving aberrations unchanged. Another cause for a value deviating from the simulation can be a systematic error due to an inaccuracy of the axial length reference, the focal shift.

These effects emphasize the need for calibration on the experimental setup, and also the sensitivity of the DH-PSF to aberrations, which may well be exploited for the characterization or optimization of an optical system. The calibration now opens up the possibility of calculating the axial position of an atom. This can be employed, for instance, to determine the vertical distribution of atoms in the lattice. In this way, it is also possible to check the calibration against another known axial length reference, namely the vertical lattice constant.

4.6.4 Resolving the vertical lattice

The calibration is used to convert measured rotation angles into an absolute axial position relative to the focal plane. To this end, Equation 4.36 is rearranged into

$$z = z_\mathrm{R} \tan\left(\frac{\tilde{\theta} - \beta}{V}\right) . \tag{4.39}$$

The distribution of the determined vertical positions in the first frame for the atoms selected for calibration is shown as a histogram in Figure 4.21 a). Together with the determined lateral positions, the reconstructed three-dimensional image of the atoms in the lattice in Figure 4.21 b) is obtained, with the vertical position color-coded.

While atoms were detected over the entire FOV of the camera, it can be seen that those atoms remaining after the filtering steps ① and ② (cf. Section 4.6.3) are clustered in a certain circular region. This can be explained by the fact that the VDT with a waist of 50 µm is centered there. Imaging parameters are optimized for high survival in the center of VDT. The decrease of the VDT intensity towards the edge leads to a different differential light shift and thus to less optimal imaging parameters there. This finally leads to a decrease of the survival in the edge regions, so that atoms detected there are less likely to pass the selection. Since the VDT coincides with the optical axis of the microscope, a central region of the FOV with respect to the objective lens can be chosen as a circle centered about this cluster. This motivates the concrete centering choice for selection step ③. A radius of 16.6 µm is chosen which corresponds to about half the FOV within which the objective lens is diffraction-limited [59].

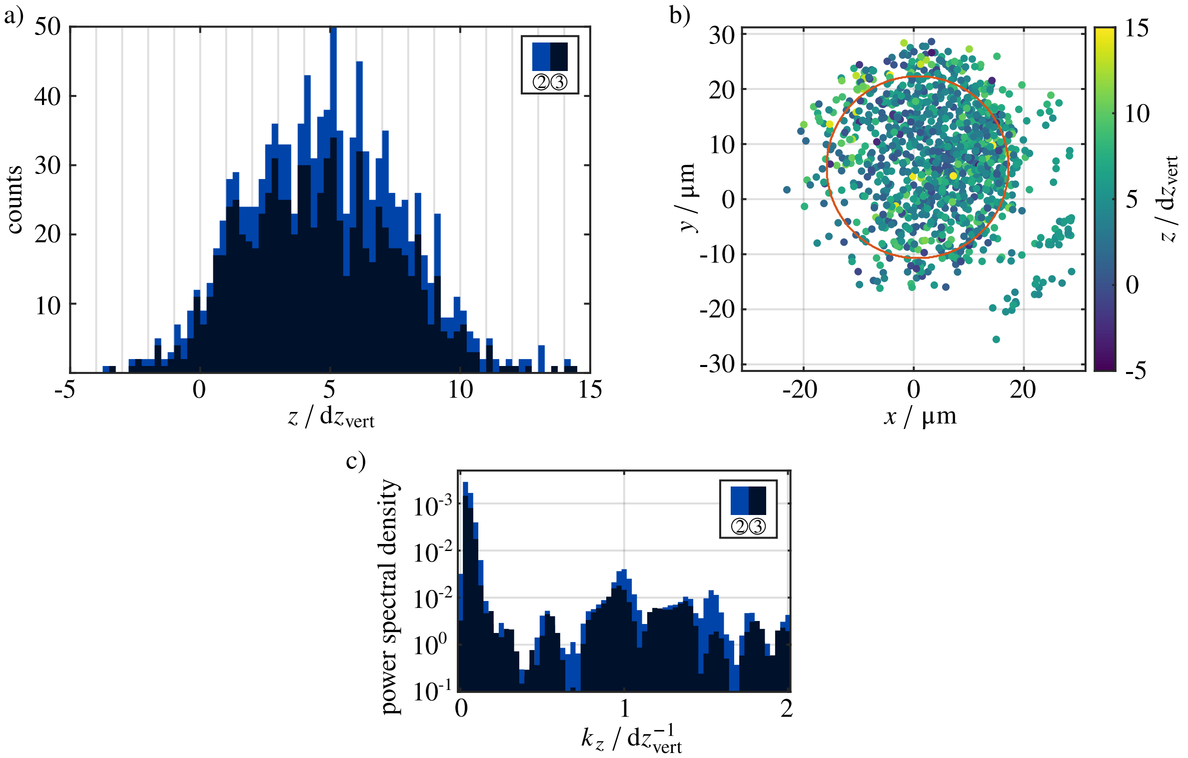

Figure 4.21: a) Histogram of determined vertical atom positions. The bin width is 0.25 dz_{vert}. Atoms filtered from outliers ② and in addition inside a central area of the FOV ③ detected in the first frame (cf. Section 4.6.3) are used, in total 1 173 and 846, respectively. b) Three-dimensional positions of the atoms. The red circle shows the selection region for ③. c) Spatial frequency spectrum of the vertical position histogram. The power spectral density is computed based on the DFT method reported in Reference [171]. The chosen bin width results in a frequency bin width of 0.0312 dz_{vert}^{-1} and a Nyquist frequency of 2 dz_{vert}^{-1}.

It can be seen in Figure 4.21 a) that the detected atoms are mostly above the focal plane within a range of around 10 vertical lattice planes centered around $z = 5\,\mathrm{d}z_{\text{vert}}$. This means that the focal plane of the microscope is shifted relative to the center of the atom cloud loaded into the lattice by about $5\,\mathrm{d}z_{\text{vert}} \approx 2.7\,\mu\mathrm{m}$. The enhanced DOF by the DH-PSF is apparent from the fact that atoms can be readily detected up to $\pm 10\,\mathrm{d}z_{\text{vert}}$ away from the focus, i.e. a range of over 10 µm, as opposed to the theoretical 1.2 µm DOF of the standard PSF at NA = 0.6.

A clustering at integer lattice sites is observed as expected from the nature of the vertical lattice. To investigate the periodicity of the vertical atom distribution in more detail, the spatial frequency spectrum shown in Figure 4.21 c) was calculated using the DFT as reported in Reference [171]. As can be seen, the spatial frequency spectrum peaks at the frequency $k_z = 1\,\mathrm{d}z_{\text{vert}}^{-1}$ as expected. Vertical hopping during the image exposure however leads to a smearing of the expected discrete structure in this histogram just as in the calibration fit Figure 4.20, where the data points are smeared relative to the lines of corresponding focal shifts of integer vertical lattice constants. Therefore, I expect to see more clearly separated clusters at each lattice site by reducing vertical hopping. Another contribution to the broadening is due to aberrations inhomogeneously distributed over the FOV. In fact, as was reported in Reference [59], the Strehl ratio of our objective lens reduces to 0.8 within 38 µm (cf. Section 4.2.3). We have seen that the measured angle at the focus β is sensitive to certain types of aberrations (cf. Section 4.6.3), leading to an inhomogeneous angle β over the FOV. Effectively, we are using an average angle β determined by the calibration fit and thus obtaining a bias in the vertical position determination. As atoms detected within a larger region of the FOV are included in the vertical position histogram, different biases lead to a smearing. This effect was also observed and characterized in DH-PSF microscopy of single molecules [172]. In order to calibrate the PSF sampled across the FOV with an accurate axial and lateral length reference, a regularly spaced sub-diffraction aperture grid filled with fluorescent dyes was used. Thanks to our lattice geometry, such a calibration parameterized over the FOV is possible using the data type described here. The reduced bias will thereby increase the accuracy of axial localization. All that is needed is a sufficient number of recorded atoms per FOV area.

The lattice structure that is nevertheless visible demonstrates the capability of vertical single-site resolution by the DH-PSF. It furthermore confirms the accuracy of the axial length reference used for the axial calibration, namely the use of a focal shift by a holographic lens on the SLM. This renders this novel calibration technique a much simpler alternative to the common technique of piezo-control of the objective [74] in systems in which an SLM is used for PSF engineering.

4.7 Summary and conclusion

Prompted by the need to have access to the axial position of individual atoms trapped in a three-dimensional optical lattice, I have presented a modification of our quantum gas microscope that implements PSF phase engineering, allowing single-site direction along all three dimensions over an extended DOF.

Quantum walks and single-atom interferometry using two-dimensional state-dependent transport require atoms to be in the same vertical plane of the lattice. Although the initially thickly filled lattice can be made to retain atoms only in a specific plane via vertical microwave spectroscopy, a few atoms always remain outside the target plane. Given the trade-off between plane selection fidelity and target plane survival, the ability to post-select the vertical position also allows one to choose a higher target plane survival.

The response of the microscope to a point source, the PSF, determines the localization precision. While the standard PSF is well suited for high lateral resolution, it retains little information about axial position. Different techniques that either acquire the PSF at different focus settings or acquire the full light field information allow axial localization with higher precision. The other approach is to modify the PSF itself so that it carries more axial position information. PSFs with broken azimuthal symmetry that rotate rigidly along the axial direction have been shown to provide easily detectable and unambiguous depth information through their rotation angle. Their rotational property can be implemented and understood in terms of the interference of orthogonal LG modes. A particularly useful example is the DH-PSF, which consists of two peaks spiralling around each other. It is shown that the DH-PSF inherently carries more information about the axial position, and in the noise-free case even about the lateral position over an extended DOF. Albeit the DH-PSF extending over a larger area than the standard PSF by construction, studies have shown that it is possible to retrieve the emitters position even in dense settings. In addition, rotating PSFs can be algorithmically optimized to maximize position information over target dimensions and regions.

In the fluorescence microscope at hand, the PSF is phase-engineered in the pupil plane by means of an SLM. For this purpose, the imaging system was redesigned to include a secondary pupil plane, as the microscope's pupil plane lies within the vacuum cell. The built-in SLM modulates only a linear polarisation, which requires the use of a polariser and reduces the amount of usable light. However, it introduces a high degree of flexibility into the apparatus, as demonstrated by the compensation of residual aberrations by the SLM itself and its use in the alignment procedure. Moreover, I presented a PSF simulation to help select an appropriate DH-PSF and to understand the detrimental effects of aberrations.

Finally, I demonstrated the axial localisation of single atoms in the three-dimensional lattice by determining the measured DH-PSF rotation angles. An algorithm is presented that detects peaks and pairs them to give the PSF location and orientation of the corresponding individual atoms. The axial localization is calibrated using sets of three images taken from the same ensemble of atoms, while shifting the focal plane of the imaging system in the second image by a known distance. The focal shift is achieved by a holographic lens of long focal length programmed on the SLM. The vertical lattice structure could be resolved, demonstrating the capability of vertical single-site resolution. It also confirms a high accuracy of the focal shift for the axial calibration, making the novel calibration technique proposed a much simpler alternative to piezo-control of the objective. Moreover, it was shown that atoms can be detected over an axial range of more than 10 µm, underlining the enhanced DOF by the DH-PSF

CHAPTER 5

Conclusion and Outlook

In this thesis, I presented a novel quantum gas microscopy technique enabling the three-dimensional localization of single atoms in an optical lattice with sub-micrometer resolution. The technique consists of modifying the point spread function (PSF) of the microscope via phase-engineering in the pupil plane to obtain an azimuthally asymmetric intensity distribution. With this, the position of an atom along the imaging axis can be extracted from the rotation angle of its corresponding PSF. The lateral position of the atom can be determined with unaffected precision from the center of the PSF in the image.

In particular, I demonstrated the method using a double-helix point spread function (DH-PSF) which proved to be particularly suitable. The observation of the vertical lattice structure with a plane separation of 532 nm has illustrated the single-site resolution at NA = 0.6. As the rotation rate of the engineered PSF increases with the numerical aperture (NA), the achieved resolution is accessible to typical quantum gas microscopes having NA $\gtrsim 0.6$ [14, 27, 38, 47, 48, 59, 61, 173, 174]. In the present work, DH-PSF allowed the localization over an axial range of more than 10 µm, i.e., well over the 1.2 µm depth of field (DOF) of the regular PSF. Many three-dimensional microscopes employing engineered PSFs use piezo-control of the objective lens to perform an angle-position calibration [74]. I have presented an alternative simple calibration method based on shifting the focal plane by a programmed holographic lens between consecutive images, which, to the best of my knowledge, has not yet been used. We note that it does not rely on the lattice geometry and could therefore be employed in microscopes for single molecules using phase modulating spatial light modulators (SLMs).

The idea of the DH-PSF is inspired by super-resolved three-dimensional fluorescence microscopy of single molecules [74, 78, 79, 132]. Sparse ensembles of fluorescing molecules can thereby be localized well below the diffraction limit along all three dimensions down to precisions of 20 to 40 nm by employing the knowledge of the PSF [132]. Detection methods reach the theoretical Cramér-Rao lower bound (CRLB) of localization precision along all dimensions [76]. My use of double Gaussian peak fitting as an estimator for the localization is computationally fast, as it is non-iterative. However, it uses only a part of the PSF geometrical shape and does not include any noise statistics, thus it is not expected to reach the CRLB resolution limit. Accordingly, the localization precision can be increased compared to the presented method. While maximum-likelihood estimators including noise and a faithful PSF model can reach optimal estimation, large calibration data sets required. Reference [76] reports a phase retrieval method, allowing to recover the three-dimensional PSF using fewer calibration measurements.

As I discussed, the CRLB can in turn also be used as a metric to design PSFs optimized with respect to achievable resolutions [80]. While the DH-PSF constructed from Laguerre-Gauss (LG) modes utilized

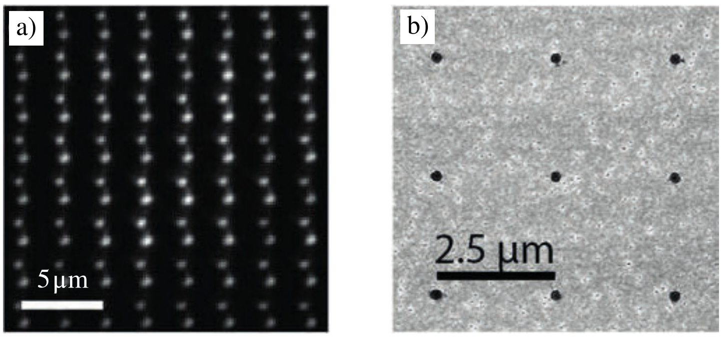

Figure 5.1: Aberration characterization for a DH-PSF molecule microscope. Taken and modified from Reference [172]. The spatial inhomogeneity of the DH-PSF angle across the FOV due to aberrations is apparent. a) Measured DH-PSF in a transversal plane along the FOV. b) Scanning electron microscope image of a nano hole array with a pitch of 2.5 µm and hole diameters ≤ 200 nm employed for the measurement.

in this thesis show clearly lower localization CRLBs than the regular PSF, I discussed several approaches to further optimize the PSF. In some sense, the manual aberration compensation I performed can already be understood as such an optimization, obviously unlikely to end in a global extrema.

The two fields of research, connected by a shared interest in precise detection of single fluorescent particles, could benefit from common synergies. For instance, cold atoms in optical lattices have also been localized well below the diffraction limit using computational methods [39, 125]. Furthermore, light field microscopy has been used for three-dimensional imaging of atoms, however at resolutions of 16 to 100 µm [69]. Utilizing a Fourier light field microscope configuration, precision up to 20 nm (thus comparing to the DH-PSF) have recently been attained with molecules [135]. Such a system could well be useful for cold atoms as well.

In this thesis, I showed by simulation that, besides the high precision, the accuracy of the DH-PSF is sensitive to certain aberrations. Ultimately, this high aberration sensitivity also allows to measure and correct the aberrations precisely [170], or to remove the resulting bias from measured angles [172]. I propose to parameterize the measured in-focus angle β over the field of view (FOV) and thus improve the accuracy of the axial calibration over the whole FOV. Figure 5.1 shows the measured DH-PSF of a lateral plane in a microscope for molecules, illustrating this idea. Having a system with known geometry at hand through the optical lattice makes this particularly easy. This is in contrast to microscopy of molecules for which a nano hole array filled with fluorescent dyes had to be prepared as a controllable sample of the DH-PSF along a transversal plane of the FOV.

In quantum gas microscopes, the use of only sparse distributions of atoms during imaging is *a priori* not an option, in contrary to the various methods employed in super-resolution microscopy of biological samples. There, the number of fluorescing molecules during an image acquisition can be tuned, e.g. by employing their temporal behavior [122–124]. However, this so-called labeling density limits data collection times. Therefore, efforts have been made to work at higher densities. In fact, a localization scheme allowing the identification of emitters in images with overlapping DH-PSFs while maintaining high localization precisions have been reported by Reference [79]. Figure 5.2 shows DH-PSF reconstructions at low densities (comparable to the ones in this thesis) and at high densities of 1.2 µm^{-2}. As a comparison, a unit filling of our lattice would correspond to 2.7 µm^{-2}. I however expect that the DH-PSF allows reconstructions at such densities for atoms in optical lattices, as the knowledge about the lattice geometry can be used. The increase of DOF by the DH-PSF complicates the imaging of

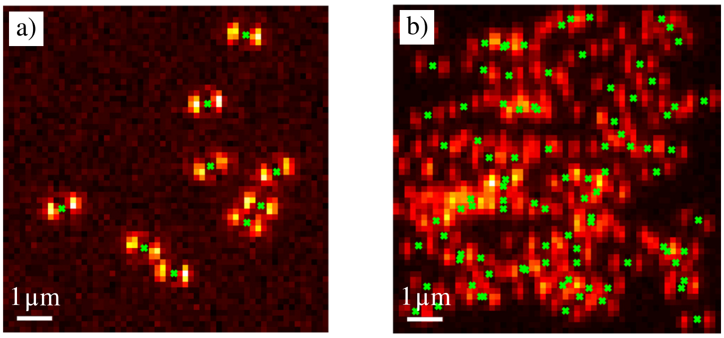

Figure 5.2: DH-PSF reconstructions at different densities (simulated images). The detected emitters are marked by x. Taken and modified from Reference [79]. a) Emitter density of 0.12 µm^{-2}. b) Emitter density of 1.2 µm^{-2}.

ensembles with high axial densities. By means of PSF optimizations, PSFs maximizing a figure of merit designed for a specific application could be constructed.

The polarizer required for the phase modulating SLM significantly reduces the reachable signal-to-noise ratio (SNR) for a given photon budget in the presented setup. Considering the finite lifetime of atoms in the lattice, increasing the exposure time for higher signals is not optimal, but still preferable to taking multiple images as in tomography. Optical configurations have been designed that use both polarizations [157, 158]. At the cost of losing the programmable flexibility of the SLM, a custom manufactured diffractive optical elements could be used, reaching higher optical efficiency as the phase modulation does not apply to a specific polarization [83].

In the measurements presented in this thesis, a substantial vertical and horizontal hopping probability has been observed. Adjustment of the vertical polarization gradient cooling (PGC) on the D1 line is not readily optimized over large FOVs due to light shift gradients caused by the inhomogeneity of the vertical dipole trap (VDT). Therefore, an abundance of available power of the VDT laser should be utilized to create a deeper and broader VDT giving more homogeneous conditions within the FOV. The vertical PGC should correspondingly be verified and adapted. The horizontal hopping, while not as severe, should also be addressed. I presented my contribution to a twofold increase of the horizontal dipole trap (HDT) depth in Chapter 3 by increasing the laser power usage efficiency. Additional increase could be achieved with by anti-reflective (AR) coating the employed photonic crystal fiber (PCF). However, there is not too much more leeway, since the laser power is ultimately limited. Further research needs to quantify hopping more precisely, and identify and address the heating effects.

The SLM in the pupil plane of the two-dimensional discrete quantum simulator (DQSIM) objective lens can finally also be employed for local site-resolved addressing of atoms. A structured intensity pattern can be holographically generated by an SLM as described in Reference [167] and characterized in Reference [169]. While microwaves are well suited for global coherent operations, Reference [20] proposes to shine a structured intensity pattern of Raman light onto the optical lattice, allowing spatially inhomogeneous operations. The high spatial resolution given by the objective lens allows a sharp addressability of single atoms. Another site-resolved addressing possibility is to induce AC Stark shifts on the target atoms by the structured intensity pattern. Microwave radiation tuned to the shifted resonance condition then locally drives the qubit state [17].

Ultimately, this new imaging technique broadens the toolbox for control in quantum gas microscopes.

Appendix

APPENDIX A

Short introduction to Fourier optics

In this appendix, the important principles of Fourier optics needed for the understanding of the experiment are presented. Starting from the basic equations of optics, the paraxial approximation as well as the diffraction integral and its Fresnel and Fraunhofer approximations are described. Building on that, the Fourier transform property of lenses is derived. All derivations are supported by References [99, 119], except stated otherwise.

A.1 The paraxial approximation

The Maxwell equations for linear, isotropic, homogene and non-dispersive dielectrics with refractive index n yields the wave equation

$$\left(\nabla^2 - \frac{n^2}{c^2}\frac{\partial^2}{\partial t^2}\right)\tilde{\boldsymbol{U}}(\boldsymbol{x},t) = 0\,, \tag{A.1}$$

where $\tilde{\boldsymbol{U}}(\boldsymbol{x},t)$ is the electric or magnetic field. For monochromatic waves with harmonic time evolution separation of variables $\tilde{\boldsymbol{U}}(\boldsymbol{x},t) = \boldsymbol{U}(\boldsymbol{x})\,\mathrm{e}^{-\mathrm{i}\omega t}$ gives the Helmholtz equation

$$\left(\nabla^2 + k^2\right)\boldsymbol{U}(\boldsymbol{x}) = 0\,, \tag{A.2}$$

where $\omega = ck$. An identical scalar Helmholtz equation holds for each components U of $\boldsymbol{U}$.

The paraxial approximation holds for a wave that propagates only in directions with small angles with respect to the optical axis, and approximates the scalar field as

$$U(\boldsymbol{x}) \approx v(\boldsymbol{x})\,\mathrm{e}^{\mathrm{i}kz} \tag{A.3}$$

for a function $v(\boldsymbol{x})$ slowly varying in z, i.e. $\left|\partial^2 v/\partial z^2\right| \ll \left|k\frac{\partial v}{\partial z}\right|$. The paraxial Helmholtz equation

$$\nabla_\perp^2 U(\boldsymbol{x}) + 2\mathrm{i}k\frac{\partial U}{\partial z} = 0 \tag{A.4}$$

with the transverse Laplacian $\nabla_\perp^2 = \frac{\partial^2}{\partial x^2} + \frac{\partial^2}{\partial y^2}$ is then obtained by insertion of Equation A.3 into the

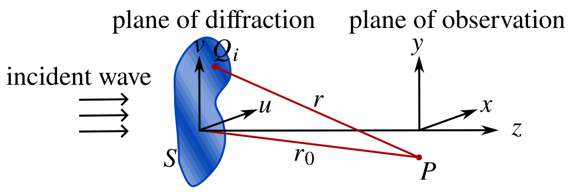

Figure A.1: Geometry of Kirchhoff's Diffraction Integral.

scalar version of Equation A.2 and using the slow variation of $v(\boldsymbol{x})$ in z.

A.2 The diffraction integral

Consider the scalar Helmholtz equation (cf. Equation A.2) for the field $U(\boldsymbol{x}) = A(\boldsymbol{x})\mathrm{e}^{\mathrm{i}\phi(\boldsymbol{x})}$ with amplitude $A(\boldsymbol{r})$ and phase $\phi(\boldsymbol{x})$. Following Huygens' principle, the field $U(\boldsymbol{x}_P)$ at a point P consists of the sum of spherical waves of all contributing point sources Q_i at positions $\boldsymbol{x}_{Q_i}$. The spherical waves

$$U_{Q_i}(\boldsymbol{x}) = U_{Q_i}(\boldsymbol{x}_{Q_i})\frac{\mathrm{e}^{\mathrm{i}kr}}{kr}\,, \tag{A.5}$$

with $r = |\boldsymbol{x} - \boldsymbol{x}_{Q_i}|$, are solutions of the Helmholtz equation. Kirchhoff's diffraction integral in the paraxial approximation

$$U(\boldsymbol{x}_P) = \frac{U_S k}{2\pi\mathrm{i}} \oint_S \tau(u,v)\frac{\mathrm{e}^{\mathrm{i}kr}}{r}\mathrm{d}u\mathrm{d}v \tag{A.6}$$

is derived by means of Green's theorem, where the geometry is defined as in Figure A.1. The surface S (the aperture) with the transmission function $\tau(u,v)$ is illuminated by a plane wave of amplitude U_S. The integral thus describes the field in the point P of the observation plane, given an incident wave and the transmission function of the aperture.

Expressing r and r_0 in the coordinates of the diffraction and observation planes, respectively, we get

$$r = \sqrt{(x-u)^2 + (y-v)^2 + z^2} = r_0\sqrt{1 - \frac{2(xu+yv)}{r_0^2} + \frac{u^2+v^2}{r_0^2}} \simeq r_0\left(1 - \frac{\kappa_u u + \kappa_v v}{kr_0} + \frac{u^2+v^2}{2r_0^2}\right)\,, \tag{A.7}$$

with the spatial frequencies $\kappa_u = kx/r_0$ and $\kappa_v = ky/r_0$, so that the phase factor in Equation (A.6) is decomposed into

$$\mathrm{e}^{\mathrm{i}kr} \simeq \mathrm{e}^{-\mathrm{i}kr_0}\mathrm{e}^{\mathrm{i}(\kappa_u u + \kappa_v v)}\mathrm{e}^{\mathrm{i}\frac{k(u^2+v^2)}{2r_0}}\,. \tag{A.8}$$

The last phase factor depending only on the aperture plane coordinates is called Fresnel factor. It determines the possible approximations to the diffraction integral, which is difficult to numerically solve, namely

$$\text{the Fraunhofer approximation for} \quad a^2 \ll \lambda z/\pi\,, \tag{A.9}$$

$$\text{and the Fresnel approximation for} \quad a^2 \geq \lambda z/\pi \quad \text{and} \quad a \ll z\,. \tag{A.10}$$

A.2.1 Fresnel diffraction

The Fresnel approximation valid in the near field is obtained by Tayler expanding the first expression in Equation (A.7)

$$r \simeq z\left(1 + \frac{(x-u)^2}{2z^2} + \frac{(y-v)^2}{2z^2}\right),$$

and inserting into the diffraction integral Equation A.6,

$$U(\boldsymbol{x}_P) = \frac{U_S k}{2\pi \mathrm{i}} \frac{\mathrm{e}^{\mathrm{i}kz}}{z} \oint_S \tau(u,v) \exp\left(\frac{\mathrm{i}k}{2z}\left((x-u)^2 + (y-v)^2\right)\right) \mathrm{d}u\mathrm{d}v\,. \tag{A.11}$$

taking $r \approx z$ in the denominator.

This can be written as a convolution of the aperture plane field further propagated by z with the kernel $K_z(x,y) = \frac{k}{2\pi \mathrm{i}z} \exp\left(\frac{\mathrm{i}k}{2z}(x^2+y^2)\right)$, i.e.,

$$U_z(x,y) = \left(\mathrm{e}^{\mathrm{i}kz} U_S \tau(x,y)\right) * K_z(x,y)\,. \tag{A.12}$$

The Fresnel diffraction integral solves the paraxial Helmholtz equation [175] (cf. Section A.1).

A.2.2 Fraunhofer diffraction

If the condition of Equation A.9 is met, the far field is described by the Fraunhofer approximation. The expansion of Equation A.7 is inserted in the diffraction integral Equation (A.6) taking $\frac{(u^2+v^2)k}{2r_0} \approx 0$. This yields with $r \approx z$ in the denominator

$$U(\boldsymbol{x}_P) = \frac{U_S k}{2\pi \mathrm{i}} \frac{\mathrm{e}^{\mathrm{i}kr_0}}{z} \oint_S \tau(u,v) \mathrm{e}^{-\mathrm{i}\left(\kappa_u u + \kappa_v v\right)} \mathrm{d}u\mathrm{d}v\,, \tag{A.13}$$

which corresponds to the spherical wave in point P modulated with the Fourier transform of the transmission function

$$T(x,y) = \iint \tau(u,v) \mathrm{e}^{-\mathrm{i}\left(\kappa_u u + \kappa_v v\right)} \mathrm{d}u\mathrm{d}v\,. \tag{A.14}$$

As an important example, consider the circular aperture as the diffraction object, which is present in most optical elements. Its Fraunhofer pattern has the well-known Airy disk as intensity.

A.3 The Fourier transform property of a lens

To work in the Fraunhofer far field, it is useful to reduce the distance imposed by Equation (A.9). This is possible by a converging lens[1], whose complex and thus phase modulating transmission function is

---

[1] Here as an idealized thin lens with positive focal length f.

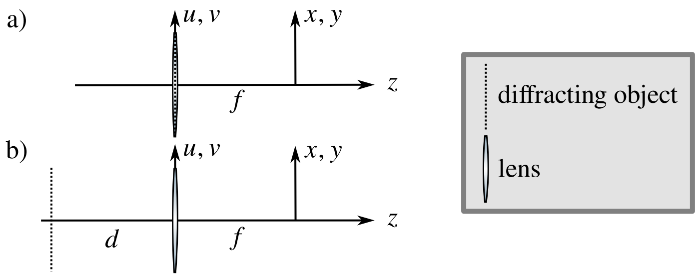

Figure A.2: Geometry of the Fourier transform property of a lens with the diffracting object a) at the position of the lens and b) at a distance d.

given by[2]

$$t_f(u,v) = \exp\left(-\mathrm{i}\frac{k}{2f}\left(u^2+v^2\right)\right), \tag{A.15}$$

where f is the focal length [119]. If the lens is superimposed on the diffraction plane as in Figure A.2 a), the light field immediately after is given by

$$U_L'(u,v) = U_0\tau(u,v)t_f(u,v), \tag{A.16}$$

where U_0 is the amplitude of the incident plane wave. To compute the field $U_f(x,y)$ in the back focal plane, we use the Fresnel diffraction Equation A.11 with $z = f$, i.e.

$$U_f(x,y) = \frac{k\mathrm{e}^{\mathrm{i}kf}}{2\pi\mathrm{i}f}\mathrm{e}^{\frac{\mathrm{i}k}{2f}(x^2+y^2)}\iint U_L'(u,v)\mathrm{e}^{\frac{\mathrm{i}k}{2f}(u^2+v^2)}\mathrm{e}^{-\frac{\mathrm{i}k}{f}(xu+yv)}\mathrm{d}u\mathrm{d}v, \tag{A.17}$$

where the exponent of the phase term inside the integral is multiplied out. By insertion of Equation A.16, the quadratic phases exactly cancel, giving

$$U_f(x,y) = \frac{k\mathrm{e}^{\mathrm{i}kf}}{2\pi\mathrm{i}f}\mathrm{e}^{\frac{\mathrm{i}k}{2f}(x^2+y^2)}\underbrace{\iint U_0\tau(u,v)\mathrm{e}^{-\frac{\mathrm{i}k}{f}(xu+yv)}\mathrm{d}u\mathrm{d}v}_{=\mathcal{F}\left\{U_0\tau\right\}\left(\kappa_u,\kappa_v\right)}, \tag{A.18}$$

which is a Fraunhofer diffraction pattern with an additional quadratic phase (cf. Equation A.13). The field is thus proportional to the two-dimensional Fourier transform of the light field incident on the lens evaluated at the spatial frequencies $\kappa_u = kx/f$ and $\kappa_v = ky/f$ and a quadratic phase curvature, even though the distance to the observation plane is only f.

Considering now the more general case as in Figure A.2 b), that the diffraction plane is at distance d of the lens, the field incident on the lens is the Fresnel diffraction pattern at distance d, which can be expressed by a convolution according to Equation (A.12). Its Fourier transform can be calculated by the convolution theorem to

$$\mathcal{F}\left\{\left(\mathrm{e}^{\mathrm{i}kd}U_0\tau\right) * K_d\right\}\left(\kappa_u,\kappa_v\right) = \mathrm{e}^{\mathrm{i}kd}\mathcal{F}\left\{U_0\tau\right\}\left(\kappa_u,\kappa_v\right)\cdot\mathcal{F}\left\{K_d\right\}\left(\kappa_u,\kappa_v\right). \tag{A.19}$$

---

[2] The lens is assumed to be infinitely extended. By an additional aperture factor which is 1 inside the lens and 0 otherwise, the lens aperture can be taken into account.

With $\mathcal{F}\left\{K_d\right\}\left(\kappa_u,\kappa_v\right)=\exp\left(-\frac{\mathrm{i}d}{2k}\left(\kappa_u^2+\kappa_v^2\right)\right)$ and under substitution of Equation A.18 we get the field in the back focal plane

$$U_f(x,y)=\frac{k\mathrm{e}^{\mathrm{i}k(d+f)}}{2\pi\mathrm{i}f}\mathrm{e}^{\frac{\mathrm{i}k}{2f}\left(1-\frac{d}{f}\right)\left(x^2+y^2\right)}\mathcal{F}\left\{U_0\tau\right\}\left(\kappa_u,\kappa_v\right)\ . \tag{A.20}$$

Note that the Fourier transform is again accompanied by a quadratic phase factor, which however vanishes for $d=f$. If the diffraction plane is placed in the front focal plane of the lens, it yields an exact Fourier transform in the back focal plane. This particular arrangement is called $2f$-configuration.

APPENDIX B

Superpositions of Laguerre-Gauss modes

For completeness, and for consistent notation, I present here the derivations concerning the rotating PSFs from the superposition of LG modes presented in Reference [71]. A simplified derivation for the superposition of two LG modes is described in section 4.4.1. I begin in Section B.1 by explaining the definitions used, and then examine the superposition of arbitrary LG modes in Section B.2.

B.1 Setting the stage: notation and the LG modes

The paraxial approximation is very useful in optics as it allows to derive simple analytical expressions. It is valid for waves that propagate only in directions with small angles with respect to the optical axis [119]. As shown in Section A.1 of Appendix A, the Maxwell equations yield under this approximation the paraxial Helmholtz equation A.4. In cylindrical coordinates, a complete orthogonal (basis) set of solutions to this equation is given by the LG modes [109]. I shortly remind the reader about the expression for the LG transverse mode of order (l, p), which is given by

$$u_{lp} = C_{lp} \underbrace{\frac{w_0}{w(z)} \exp\left(-\frac{r^2}{w^2(z)}\right) \exp\left(\mathrm{i}k\frac{r^2}{2R(z)}\right)}_{=:G(r,z)} \underbrace{\left(\frac{r\sqrt{2}}{w(z)}\right)^{|l|} L_p^{|l|}\left(\frac{2r^2}{w^2(z)}\right)}_{=:R_{lp}(r,z)} \exp\left(\mathrm{i}l\phi - \mathrm{i}\psi_{lp}(z)\right) , \quad \text{(B.1)}$$

with the definitions given by the equations 4.7 to 4.11. The field $\boldsymbol{U}(\boldsymbol{x}, t)$, for clarity, is then given by the components $U(\boldsymbol{x}, t) = u(r, \phi, z)\, \mathrm{e}^{\mathrm{i}kz-\mathrm{i}\omega t}$.

The notation used in this work differs from Reference [71] in that the LG modes are written out with the azimuthal mode index l and the radial mode index p, instead of the combined mode index n and the azimuthal mode index $m (= l)$. Furthermore, I group some terms in a different manner. E.g., Reference [71] calls only $\arctan(z/z_\mathrm{R})$ the Gouy phase, while I follow the more common convention to call $(2p + |l| + 1)\arctan(z/z_\mathrm{R})$ to Gouy phase, as in Equation 4.11 and e.g. [109]. The normalization constant reported in Reference [71] is chosen to yield unity for the maximal intensity of the mode, while I prefer the normalization to yield unity when integrating the LG transverse mode over the radial and azimuthal dimension, allowing direct comparison of the intensity of different LG modes of the same total optical power.

Interestingly, the paraxial Helmholtz equation A.4 has the same form as the free space Schrödinger equation in two dimensions, i.e.

$$-\frac{\hbar^2\nabla_\perp^2}{2m}\Psi(x,y,t) = \mathrm{i}\hbar\frac{\partial}{\partial t}\Psi(x,y,t) \quad\Leftrightarrow\quad \nabla_\perp^2\Psi(x,y,t) + 2\mathrm{i}\frac{m}{\hbar}\frac{\partial}{\partial t}\Psi(x,y,t) = 0 \tag{B.2}$$

under substitution of the z coordinate by the time t, the transverse mode function $u(\boldsymbol{x}) = \langle \boldsymbol{x}|l,p\rangle$ by the wave function $\Psi(x,y,t) = \langle x,y\,|\,\Psi(t)\rangle$ and the wave number k by $m/\hbar$. This allows us to use the quantum mechanics formalism for the analysis of paraxial waves by using time domain semantics to describe the evolution along the z-axis, e.g. the convenient use of Dirac notation. For instance, the orthonormality relation of the LG modes can concisely be written as

$$\langle l',p'|l,p\rangle = \delta_{ll'}\delta_{pp'}\,, \tag{B.3}$$

with the scalar product defined by

$$\langle\Psi|\Phi\rangle = \int_0^{2\pi}\mathrm{d}\phi\int_0^{\infty}\mathrm{d}r r\,\Psi^*(\boldsymbol{x})\Phi(\boldsymbol{x})\,. \tag{B.4}$$

B.2 Rotating intensity profiles from LG mode superpositions

Let us examine the intensity of any superposition of N LG modes with normalized coefficients $a_j\in\mathbb{C}$,

$$|A\rangle = \sum_{j=1}^{N} a_j\,|l_j,p_j\rangle\,,\quad\text{where}\quad \sum_{j=1}^{N}|a_j|^2 = 1 \tag{B.5}$$

with the modes sorted according to their combined mode indexes $n_j = 2p_j + |l_j|$ such that $n_j \le n_{j+1}$. It is, using the abbreviations defined in Equation B.1, given by

$$\begin{aligned}
I(\boldsymbol{x}) = \frac{\epsilon_0 c}{2}\,|\langle\boldsymbol{x}|A\rangle|^2 &= \frac{\epsilon_0 c}{2}\left|\sum_{j=1}^{N} a_j\,\langle\boldsymbol{x}|l_j,p_j\rangle\right|^2 && \text{(B.6)}\\
&= \frac{\epsilon_0 c}{2}\sum_{j=1}^{N}\sum_{i=1}^{N} a_j a_i^*\,\langle\boldsymbol{x}|l_j,p_j\rangle\,\langle l_i,p_i|\boldsymbol{x}\rangle && \text{(B.7)}\\
&= \frac{\epsilon_0 c}{2}\left(\sum_{j=1}^{N}|a_j|^2\,|\langle\boldsymbol{x}|l_j,p_j\rangle|^2 + 2\sum_{j=1}^{N}\sum_{i=j+1}^{N}\mathrm{Re}\left(a_j a_i^*\,\langle\boldsymbol{x}|l_j,p_j\rangle\,\langle l_i,p_i|\boldsymbol{x}\rangle\right)\right) && \text{(B.8)}\\
&= \frac{\epsilon_0 c}{2}\left(\sum_{j=1}^{N}|a_j|^2\,|\langle\boldsymbol{x}|l_j,p_j\rangle|^2 + 2\sum_{j=1}^{N}\sum_{i=j+1}^{N}\left(|a_j||a_i|\,|\langle\boldsymbol{x}|l_j,p_j\rangle|\,|\langle\boldsymbol{x}|l_i,p_i\rangle|\right)\right. && \text{(B.9)}\\
&\qquad\left.\times\cos\left(\arg(\langle\boldsymbol{x}|l_j,p_j\rangle) - \arg(\langle\boldsymbol{x}|l_i,p_i\rangle) + \arg(a_j) - \arg(a_i)\right)\right)
\end{aligned}$$

$$= \frac{\epsilon_0 c}{2} |G(r,z)|^2 \left(\sum_{j=1}^{N} |a_j|^2 C_{l_j p_j}^2 R_{l_j p_j}^2 (r,z) \right. \tag{B.10}$$
$$+ 2 \sum_{j=1}^{N} \sum_{i=j+1}^{N} |a_j||a_i| C_{l_j p_j} C_{l_i p_i} R_{l_j p_j}(r,z) R_{l_i p_i}(r,z)$$
$$\left. \times \cos\Big((l_j - l_i)\phi - (n_j - n_i) \arctan(z/z_\mathrm{R}) + \arg(a_j) - \arg(a_i) \Big) \right) .$$

For the case of two LG modes, this yields equations 4.12 and 4.13 derived in Section 4.4.1. The first sum is axially symmetric and stationary in z except for a scaling with $w(z)$. Thus, these terms do not contribute to the targeted scaled-rigid rotation. The terms in the second sum rotate linearly with $\arctan(z/z_\mathrm{R})$ at the rotation rates

$$\left(\frac{\mathrm{d}\phi}{\mathrm{d}z} \right)_{ji} = \frac{\Delta n_{ji}}{\Delta l_{ji}} \frac{\mathrm{d}}{\mathrm{d}z} \arctan(z/z_\mathrm{R}) , \tag{B.11}$$

where $\Delta n_{ji} := n_j - n_i$ and $\Delta l_{ji} := l_j - l_i$. Again, for the case of two LG modes, Equation 4.15 derived in Section 4.4.1 is obtained.

As can be seen in the Cosine term of Equation B.10, in order to break the axial symmetry, at least two modes have to have different azimuthal mode numbers, $\Delta l_{ji} \neq 0$, such that their different orbital angular momentum phases $\mathrm{e}^{\mathrm{i} l_j \phi}$ and $\mathrm{e}^{\mathrm{i} l_i \phi}$ give an azimuthal interference pattern. Similarly, the necessary condition for dynamic behaviour along the z-axis is that $\Delta n_{ji} \neq 0$ for at least two modes. The different Gouy phases $\psi_{l_j p_j}$ and $\psi_{l_i p_i}$ then lead to z-dependent interference patterns.

Without loss of generality, we can label the modes such that $n_j \leq n_{j+1}$. Scaled-rigid rotation occurs if and only if all interference terms rotate at the same velocity. Evidently, a *necessary* condition for this is that

$$\frac{n_{j+1} - n_j}{l_{j+1} - l_j} =: \frac{\Delta n_j}{\Delta l_j} =: V_j \tag{B.12}$$

is the same for all LG modes, that is,

$$V := V_j = \mathrm{const.} \quad \forall j \in \{1, 2, \ldots, N\} . \tag{B.13}$$

This condition is also *sufficient*, as can easily be by proven by induction: Assume that Equation B.13 holds. As by definition $n_j = 2p_j + |l_j|$, it follows that both $\Delta n_j = \mathrm{const.} =: \Delta n$ and $\Delta l_j = \mathrm{const.} =: \Delta l$ hold. We now need to show that $\forall i \in \{1, 2, \ldots, N\}$ with $i \neq j$ the fraction of mode number differences are equal to V, i.e.

$$\frac{n_i - n_j}{l_i - l_j} = V . \tag{B.14}$$

Without loss of generality, we can take $i > j$ (if $i < j$, just rename $i \leftrightarrow j$). From our assumption directly follows that Equation B.14 holds for $i = j + 1$. Thereby also $n_i - n_j = \Delta n$ and $l_i - l_j = \Delta l$ separately hold for $i = j + 1$. We proceed by showing the induction step $i \longrightarrow i + 1$

$$\frac{n_{i+1} - n_j}{l_{i+1} - l_j} = \frac{n_i - n_j + n_{i+1} - n_i}{l_i - l_j + l_{i+1} - l_i} = \frac{\Delta n + \Delta n_i}{\Delta l + \Delta l_i} = \frac{2\Delta n}{2\Delta l} = V \tag{B.15}$$

by using the induction hypothesis. It follows that Equation B.13 is also a sufficient condition for scaled-rigid rotation.

In particular, any combination of only two LG modes yield scaled-rigid rotation. We can conclude that for mode combinations meeting the condition of scaled-rigid rotation, the rotation velocity of the transverse intensity pattern can be written according to Equation B.11 as

$$\frac{\mathrm{d}\phi}{\mathrm{d}z} = V \frac{\mathrm{d}}{\mathrm{d}z} \arctan(z/z_\mathrm{R})\,, \tag{B.16}$$

which is nothing else but Equation 4.15 in Section 4.4.2.

APPENDIX C

Miscellaneous

This appendix presents derivations of some equations used in this thesis. In Section C.1, I derive an expression for the three-dimensional PSF. In Section C.2, I show how to obtain the field amplitude in the pupil plane due to the apodization of an optical system. I then give a brief overview of the low-order Zernike polynomials in Section C.3. Lastly, I derive the expression for the shift of the focal plane using a holographic lens in Section C.4.

C.1 An expression for a 3D PSF

To derive the expression of a three-dimensional PSF Equation 4.20 in Section 4.4.3, I follow the reasoning presented in References [144, 145]. Since the notation used differs with mine, I show the key steps in the derivation.

Consider the amplitude PSF as the inverse Fourier transform of the amplitude optical transfer function (OTF) (cf. Section 4.2.2)

$$\mathrm{PSF_A}(x, y, z) = \iiint \mathrm{OTF_A}(u, v, w)\, \mathrm{e}^{\mathrm{i}(\kappa_u u + \kappa_v v + \kappa_w w)} \mathrm{d}u \mathrm{d}v \mathrm{d}w \,, \tag{C.1}$$

with the pupil real space coordinates (x, y, z) and the corresponding Fourier coordinates (u, v, w). With the front or back focal length f, we have $\kappa_u = kx/f$, $\kappa_v = ky/f$ and $\kappa_w = kz/f$. For monochromatic light, the OTF is non-zero only on a spherical surface delimited by the aperture angle α_{max}, as sketched in Figure C.1. For small NAs, this surface can be considered flat. However, in general, we can parametrize

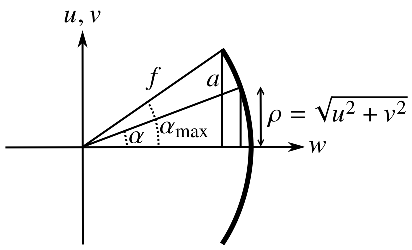

Figure C.1: Sketch of the geometry in the pupil space. Both lateral dimensions u and v are shown on one axis.

the surface by

$$w(u,v) = \sqrt{f^2 - (u^2 + v^2)} = \sqrt{a^2/\mathrm{NA}^2 - (u^2 + v^2)}\,. \tag{C.2}$$

The volume integral in Equation C.1 thus reduces to the surface integral

$$\mathrm{PSF_A}(x,y,z) = \iint \mathcal{E}_0(u,v)\,\mathcal{P}(u,v)\,\mathrm{e}^{\mathrm{i}\kappa_w w(u,v)}\,\mathrm{e}^{\mathrm{i}(\kappa_u u+\kappa_v v)}\mathrm{d}u\mathrm{d}v\,, \tag{C.3}$$

where we express the OTF on the non-zero spherical surface as the phase-modulated generalized pupil function $\mathcal{P}_{\mathrm{mod}}(u,v)$ multiplied with the incident field amplitude $\mathcal{E}_0(u,v)$ as defined in Section 4.4.3. The expression

$$\mathrm{e}^{\mathrm{i}\kappa_w w(u,v)} = \mathrm{e}^{ikz\mathrm{NA}w(u,v)/a} \tag{C.4}$$

can then be thought as the defocus aberration to add to the pupil function depending on the z-coordinate at which the PSF is evaluated. Altogether we get Equation 4.20 in Section 4.4.3.

C.2 Field amplitude in pupil plane due to apodization

As described in Reference [16], a point source uniformly radiating into the solid angle of the aperture leads to an intensity in the pupil plane scaling as

$$A_{\mathrm{Abbe}} = 1/\cos(\alpha)\,, \tag{C.5}$$

where α is the incidence angle with respect to the optical axis. Utilizing again the geometry of the pupil plane as in Figure C.1, we can write

$$\cos(\alpha) = \frac{\sqrt{f^2-\rho^2}}{f} = \sqrt{1 - \frac{u^2+v^2}{f^2}}\,. \tag{C.6}$$

For the electric field, this gives

$$\mathcal{E}_0(u,v) = E_0\left(1 - \frac{u^2+v^2}{f^2}\right)^{-1/4}\,. \tag{C.7}$$

Using $\mathrm{NA} = \sin(\alpha_{\mathrm{max}}) = a/f$ this yields Equation 4.22 in Section 4.4.3.

C.3 Zernike polynomials

Zernike polynomials are used to represent wavefronts, which can describe aberrations of optical systems (cf. Section 4.2.3). The polynomials are orthogonal on the unit disk and are named after Frits Zernike, who proposed them in 1934 [129]. The first 13 orthonormal Zernike polynomials are given in Table C.1, sorted by the so-called Noll index [176]. Figure C.2 shows the first 21 Zernike polynomials on the unit disk.

Type	Noll index	Radial degree n	Azimuthal degree m	Z_n^m
Piston	1	0	0	1
X-Tilt	2	1	1	$2\rho\cos\phi$
Y-Tilt	3	1	-1	$2\rho\sin\phi$
Defocus	4	2	0	$\sqrt{3}(\rho^2-1)$
Astigmatism (oblique)	5	2	-2	$\sqrt{6}\rho^2\sin 2\phi$
Astigmatism (vertical)	6	2	2	$\sqrt{6}\rho^2\cos 2\phi$
Coma (vertical)	7	3	-1	$\sqrt{8}(3\rho^3-2\rho)\sin\phi$
Coma (horizontal)	8	3	1	$\sqrt{8}(3\rho^3-2\rho)\cos\phi$
Trefoil (vertical)	9	3	-3	$\sqrt{8}\rho^3\sin 3\phi$
Trefoil (oblique)	10	3	3	$\sqrt{8}\rho^3\cos 3\phi$
Spherical aberration	11	4	0	$\sqrt{5}(6\rho^4-6\rho^2+1)$
Secondary astigmatism (vertical)	12	4	2	$\sqrt{10}(4\rho^4-3\rho^2)\cos 2\phi$
Secondary astigmatism (oblique)	13	4	-2	$\sqrt{10}(4\rho^4-3\rho^2)\sin 2\phi$

Table C.1: The first 13 Zernike polynomials [176].

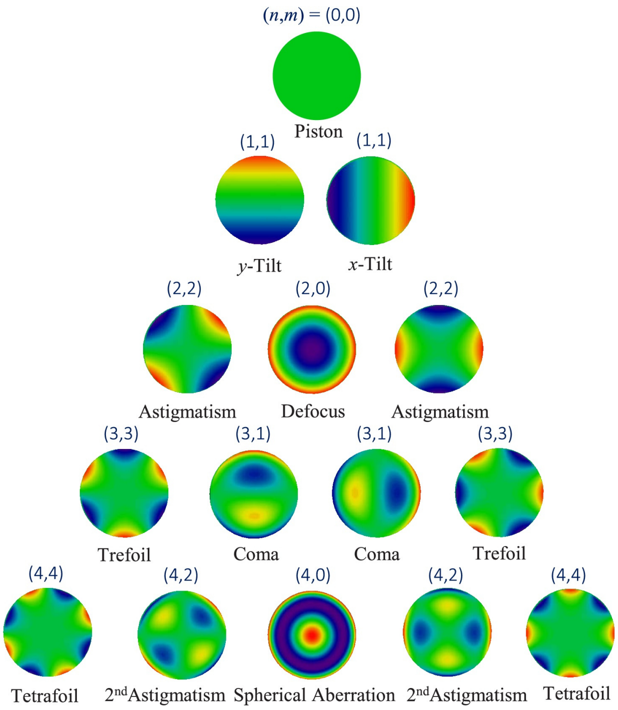

Figure C.2: The first 21 Zernike polynomials on the unit disk. Adopted with modifications from Reference [177].

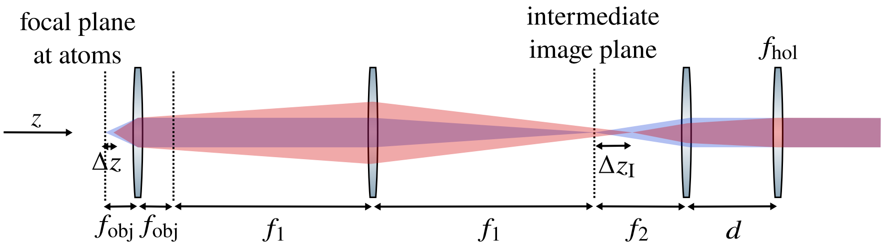

Figure C.3: Sketch of the lens system. The blue area represents a collimated beam passing through the system without holographic lens. The red area is the equivalent for the system with the holographic lens. Where the two overlap, the area is shown in magenta. The lengths shown are not to scale.

C.4 Focal plane shift of the holographic lens

I show the calculation of the displacement of the focal plane introduced by a holographic lens displayed on the SLM in the setup described in Section 4.5.2 (cf. Figure 4.9). Let us first look only at the lens system consisting of holographic lens and the lens with $f_2 = 100\,\mathrm{mm}$ creating the intermediate image, as schematized in Figure C.3. Their distance shall be d. The shift is calculated from the difference of the front focal length (FFL) of the lens system with and without holographic lens

$$\Delta z_{\mathrm{I}} = f_2 - \mathrm{FFL} = f_2 - \frac{f_2(d - f_{\mathrm{hol}})}{d - (f_2 + f_{\mathrm{hol}})} \tag{C.8}$$

which yields

$$\Delta z_{\mathrm{I}} = \frac{f_2^2}{f_{\mathrm{hol}}} \tag{C.9}$$

for $d = f_2$. The corresponding shift Δz with respect to the initial focal plane at the atoms is then related by the axial magnification f_{obj}^2/f_1^2 and yields

$$\Delta z = \frac{f_{\mathrm{obj}}^2 f_2^2}{f_1^2 f_{\mathrm{hol}}}\,. \tag{C.10}$$

We have calculated backwards in the optical system, which is fully equivalent to the reverse.

Bibliography

[1] *Report of the Forty-First Meeting of the British Association for the Advancement of Science*, 1872 1 (cit. on p. 1).

[2] N. Gisin and R. Thew, *Quantum communication*, Nature Photonics **1** (2007) 165, (cit. on p. 1).

[3] S. Pirandola et al., *Advances in quantum cryptography*, Advances in Optics and Photonics **12** (2020) 1012, (cit. on p. 1).

[4] S.-H. Wei et al., *Towards Real-World Quantum Networks: A Review*, Laser & Photonics Reviews **16** (2022) 2100219, (cit. on p. 1).

[5] T. Udem, R. Holzwarth and T. W. Hänsch, *Optical frequency metrology*, Nature **416** (2002) 233, (cit. on p. 1).

[6] V. Giovannetti, S. Lloyd and L. Maccone, *Advances in quantum metrology*, Nature Photonics **5** (2011) 222, (cit. on p. 1).

[7] C. L. Degen, F. Reinhard and P. Cappellaro, *Quantum sensing*, Reviews of Modern Physics **89** (2017) 035002, (cit. on p. 1).

[8] E. Polino, M. Valeri, N. Spagnolo and F. Sciarrino, *Photonic quantum metrology*, AVS Quantum Science **2** (2020) 024703, (cit. on p. 1).

[9] T. D. Ladd et al., *Quantum computers*, Nature **464** (2010) 45, (cit. on p. 1).

[10] I. Bloch, J. Dalibard and S. Nascimbène, *Quantum simulations with ultracold quantum gases*, Nature Physics **8** (2012) 267, (cit. on pp. 1, 3).

[11] J. I. Cirac and P. Zoller, *Goals and opportunities in quantum simulation*, Nature Physics **8** (2012) 264, (cit. on pp. 1, 3).

[12] I. M. Georgescu, S. Ashhab and F. Nori, *Quantum simulation*, Reviews of Modern Physics **86** (2014) 153, (cit. on pp. 1, 3).

[13] C. Gross and I. Bloch, *Quantum simulations with ultracold atoms in optical lattices*, Science **357** (2017) 995, (cit. on pp. 1, 3, 8).

[14] F. Schäfer, T. Fukuhara, S. Sugawa, Y. Takasu and Y. Takahashi, *Tools for quantum simulation with ultracold atoms in optical lattices*, Nature Reviews Physics **2** (2020) 411, (cit. on pp. 1, 8, 73).

[15] S. Brakhane, *The Quantum Walk Microscope*, PhD thesis: University of Bonn, 2017, (cit. on pp. 1, 3–5, 7, 11).

[16] C. Robens, *Testing the Quantumness of Atom Trajectories*, Thesis: University of Bonn, 2017, (cit. on pp. 1, 3, 40, 87).

[17] G. Ramola, *Ramsey Imaging of Optical Dipole Traps*, PhD thesis: University of Bonn, 2021, (cit. on pp. 1, 3, 6, 11–14, 57, 75).

[18] G. Ramola et al., *Ramsey Imaging of Optical Traps*, Physical Review Applied **16** (2021) 024041, (cit. on pp. 1, 8, 57).

[19] F.-R. G. Winkelmann et al., *Direct measurement of the Wigner function of atoms in an optical trap*, 2022, arXiv: `2205.15248`, (cit. on pp. 1, 3).

[20] T. Groh et al., *Robustness of topologically protected edge states in quantum walk experiments with neutral atoms*, Physical Review A **94** (2016) 013620, (cit. on pp. 1, 3, 6, 8, 11, 26, 75).

[21] M. Sajid, J. K. Asbóth, D. Meschede, R. F. Werner and A. Alberti, *Creating anomalous Floquet Chern insulators with magnetic quantum walks*, Physical Review B **99** (2019) 214303, (cit. on pp. 1, 3).

[22] C. F. Roos, A. Alberti, D. Meschede, P. Hauke and H. Häffner, *Revealing Quantum Statistics with a Pair of Distant Atoms*, Physical Review Letters **119** (2017) 160401, (cit. on pp. 1, 3, 8, 26).

[23] C. Robens et al., *Boson Sampling with Ultracold Atoms*, 2022, arXiv: `2208.12253`, (cit. on p. 1).

[24] H. Ott, *Single atom detection in ultracold quantum gases: a review of current progress*, Reports on Progress in Physics **79** (2016) 054401, (cit. on pp. 1, 2).

[25] I. Bloch, J. Dalibard and W. Zwerger, *Many-body physics with ultracold gases*, Reviews of Modern Physics **80** (2008) 885, (cit. on pp. 1, 13).

[26] J. J. Hope and J. D. Close, *Limit to Minimally Destructive Optical Detection of Atoms*, Physical Review Letters **93** (2004) 180402, (cit. on p. 1).

[27] C. Gross and W. S. Bakr, *Quantum gas microscopy for single atom and spin detection*, Nature Physics **17** (2021) 1316, (cit. on pp. 1, 26, 73).

[28] M. R. Andrews et al., *Direct, Nondestructive Observation of a Bose Condensate*, Science **273** (1996) 84, (cit. on p. 1).

[29] G. Reinaudi, T. Lahaye, Z. Wang and D. Guéry-Odelin, *Strong saturation absorption imaging of dense clouds of ultracold atoms*, Optics Letters **32** (2007) 3143, (cit. on p. 1).

[30] M. K. Tey et al., *Strong interaction between light and a single trapped atom without the need for a cavity*, Nature Physics **4** (2008) 924, (cit. on p. 1).

[31] N. Gemelke, X. Zhang, C.-L. Hung and C. Chin, *In situ observation of incompressible Mott-insulating domains in ultracold atomic gases*, Nature **460** (2009) 995, (cit. on p. 1).

[32] C.-L. Hung, X. Zhang, N. Gemelke and C. Chin, *Observation of scale invariance and universality in two-dimensional Bose gases*, Nature **470** (2011) 236, (cit. on p. 1).

[33] D. A. Smith et al., *Absorption imaging of ultracold atoms on atom chips*, Optics Express **19** (2011) 8471, (cit. on p. 1).

[34] K. Hueck et al., *Calibrating high intensity absorption imaging of ultracold atoms*, Optics Express **25** (2017) 8670, (cit. on p. 1).

[35] G. Ness, A. Vainbaum, C. Shkedrov, Y. Florshaim and Y. Sagi, *Single-Exposure Absorption Imaging of Ultracold Atoms Using Deep Learning*, Physical Review Applied **14** (2020) 014011, (cit. on p. 1).

[36] Z. Hu and H. J. Kimble, *Observation of a single atom in a magneto-optical trap*, Optics Letters **19** (1994) 1888, (cit. on p. 1).

[37] C. Weitenberg et al., *Single-spin addressing in an atomic Mott insulator*, Nature **471** (2011) 319, (cit. on pp. 1, 27).

[38] E. Haller et al., *Single-atom imaging of fermions in a quantum-gas microscope*, Nature Physics **11** (2015) 738, (cit. on pp. 1, 27, 73).

[39] A. Alberti et al., *Super-resolution microscopy of single atoms in optical lattices*, New Journal of Physics **18** (2016) 053010, (cit. on pp. 1, 7, 30, 43, 49, 74).

[40] M. Martinez-Dorantes et al., *State-dependent fluorescence of neutral atoms in optical potentials*, Physical Review A **97** (2018) 023410, (cit. on p. 1).

[41] E. Uruñuela et al., *Raman imaging of atoms inside a high-bandwidth cavity*, Physical Review A **105** (2022) 043321, (cit. on p. 1).

[42] D. Frese et al., *Single Atoms in an Optical Dipole Trap: Towards a Deterministic Source of Cold Atoms*, Physical Review Letters **85** (2000) 3777, (cit. on p. 1).

[43] S. Kuhr et al., *Deterministic Delivery of a Single Atom*, Science **293** (2001) 278, (cit. on p. 1).

[44] N. Schlosser, G. Reymond, I. Protsenko and P. Grangier, *Sub-poissonian loading of single atoms in a microscopic dipole trap*, Nature **411** (2001) 1024, (cit. on p. 1).

[45] T. Bondo, M. Hennrich, T. Legero, G. Rempe and A. Kuhn, *Time-resolved and state-selective detection of single freely falling atoms*, Optics Communications, Quantum Control of Light and Matter **264** (2006) 271, (cit. on p. 1).

[46] K. D. Nelson, X. Li and D. S. Weiss, *Imaging single atoms in a three-dimensional array*, Nature Physics **3** (2007) 556, (cit. on pp. 1, 26, 32).

[47] W. S. Bakr, J. I. Gillen, A. Peng, S. Fölling and M. Greiner, *A quantum gas microscope for detecting single atoms in a Hubbard-regime optical lattice*, Nature **462** (2009) 74, (cit. on pp. 1, 26, 27, 73).

[48] J. F. Sherson et al., *Single-atom-resolved fluorescence imaging of an atomic Mott insulator*, Nature **467** (2010) 68, (cit. on pp. 1, 26, 27, 73).

[49] M. Wilzbach et al., *Simple integrated single-atom detector*, Optics Letters **34** (2009) 259, (cit. on p. 1).

[50] H. Mabuchi, Q. A. Turchette, M. S. Chapman and H. J. Kimble,
Real-time detection of individual atoms falling through a high-finesse optical cavity,
Optics Letters **21** (1996) 1393, (cit. on p. 1).

[51] C. J. Hood, T. W. Lynn, A. C. Doherty, A. S. Parkins and H. J. Kimble,
The Atom-Cavity Microscope: Single Atoms Bound in Orbit by Single Photons,
Science **287** (2000) 1447, (cit. on p. 1).

[52] P. Horak, S. M. Barnett and H. Ritsch,
Coherent dynamics of Bose-Einstein condensates in high-finesse optical cavities,
Physical Review A **61** (2000) 033609, (cit. on p. 1).

[53] P. Maunz, T. Puppe, T. Fischer, P. W. H. Pinkse and G. Rempe,
Emission pattern of an atomic dipole in a high-finesse optical cavity,
Optics Letters **28** (2003) 46, (cit. on p. 1).

[54] A. Öttl, S. Ritter, M. Köhl and T. Esslinger,
Correlations and Counting Statistics of an Atom Laser,
Physical Review Letters **95** (2005) 090404, (cit. on p. 1).

[55] I. Teper, Y.-J. Lin and V. Vuletić,
Resonator-Aided Single-Atom Detection on a Microfabricated Chip,
Physical Review Letters **97** (2006) 023002, (cit. on p. 1).

[56] F. Brennecke et al.,
Real-time observation of fluctuations at the driven-dissipative Dicke phase transition,
Proceedings of the National Academy of Sciences **110** (2013) 11763, (cit. on p. 1).

[57] H. Ritsch, P. Domokos, F. Brennecke and T. Esslinger,
Cold atoms in cavity-generated dynamical optical potentials,
Reviews of Modern Physics **85** (2013) 553, (cit. on p. 1).

[58] F. Haas, J. Volz, R. Gehr, J. Reichel and J. Estève,
Entangled States of More Than 40 Atoms in an Optical Fiber Cavity, Science **344** (2014) 180,
(cit. on p. 1).

[59] C. Robens et al.,
High numerical aperture (NA = 0.92) objective lens for imaging and addressing of cold atoms,
Optics Letters **42** (2017) 1043, (cit. on pp. 1, 3, 7, 29, 31, 47, 51, 52, 69, 70, 73).

[60] D. Barredo, V. Lienhard, S. de Léséleuc, T. Lahaye and A. Browaeys,
Synthetic three-dimensional atomic structures assembled atom by atom, Nature **561** (2018) 79,
(cit. on pp. 1, 8, 32).

[61] O. El´iasson et al., *Spatial tomography of individual atoms in a quantum gas microscope*,
Physical Review A **102** (2020) 053311, (cit. on pp. 1, 32, 33, 73).

[62] R. Bücker et al., *Single-particle-sensitive imaging of freely propagating ultracold atoms*,
New Journal of Physics **11** (2009) 103039, (cit. on p. 2).

[63] M. Schellekens et al., *Hanbury Brown Twiss Effect for Ultracold Quantum Gases*,
Science **310** (2005) 648, (cit. on p. 2).

[64] T. Jeltes et al., *Comparison of the Hanbury Brown–Twiss effect for bosons and fermions*,
Nature **445** (2007) 402, (cit. on p. 2).

[65] T. Gericke, P. Würtz, D. Reitz, T. Langen and H. Ott, *High-resolution scanning electron microscopy of an ultracold quantum gas*, Nature Physics **4** (2008) 949, (cit. on p. 2).

[66] M. Stecker, H. Schefzyk, J. Fortágh and A. Günther, *A high resolution ion microscope for cold atoms*, New Journal of Physics **19** (2017) 043020, (cit. on p. 2).

[67] C. Veit et al., *Pulsed Ion Microscope to Probe Quantum Gases*, Physical Review X **11** (2021) 011036, (cit. on p. 2).

[68] K. Fehre et al., *Absolute ion detection efficiencies of microchannel plates and funnel microchannel plates for multi-coincidence detection*, Review of Scientific Instruments **89** (2018) 045112, (cit. on p. 2).

[69] G. E. Lott, M. A. Marciniak and J. H. Burke, *Three-dimensional imaging of trapped cold atoms with a light field microscope*, Applied Optics **56** (2017) 8738, (cit. on pp. 2, 33, 74).

[70] N. Vitrant, S. Garcia, K. Müller and A. Ourjoumtsev, *High-Resolution Imaging of Cold Atoms through a Multimode Fiber*, Physical Review Applied **15** (2021) 064047, (cit. on p. 2).

[71] Y. Y. Schechner, R. Piestun and J. Shamir, *Wave propagation with rotating intensity distributions*, Physical Review E **54** (1996) R50, (cit. on pp. 2, 35, 36, 38, 82).

[72] A. Greengard, Y. Y. Schechner and R. Piestun, *Depth from diffracted rotation*, Optics Letters **31** (2006) 181, (cit. on pp. 2, 35).

[73] S. R. P. Pavani and R. Piestun, *High-efficiency rotating point spread functions*, Optics Express **16** (2008) 3484, (cit. on pp. 2, 35, 44, 47, 56).

[74] S. R. P. Pavani et al., *Three-dimensional, single-molecule fluorescence imaging beyond the diffraction limit by using a double-helix point spread function*, Proceedings of the National Academy of Sciences **106** (2009) 2995, (cit. on pp. 2, 27, 30, 32, 35, 44, 47, 59, 71, 73).

[75] S. R. P. Pavani, A. Greengard and R. Piestun, *Three-dimensional localization with nanometer accuracy using a detector-limited double-helix point spread function system*, Applied Physics Letters **95** (2009) 021103, (cit. on pp. 2, 35, 43, 47, 60).

[76] S. Quirin, S. R. P. Pavani and R. Piestun, *Optimal 3D single-molecule localization for superresolution microscopy with aberrations and engineered point spread functions*, Proceedings of the National Academy of Sciences **109** (2012) 675, (cit. on pp. 2, 35, 73).

[77] M. D. Lew, S. F. Lee, M. Badieirostami and W. E. Moerner, *Corkscrew point spread function for far-field three-dimensional nanoscale localization of pointlike objects*, Optics Letters **36** (2011) 202, (cit. on pp. 2, 35).

[78] G. Grover, K. DeLuca, S. Quirin, J. DeLuca and R. Piestun, *Super-resolution photon-efficient imaging by nanometric double-helix point spread function localization of emitters (SPINDLE)*, Optics Express **20** (2012) 26681, (cit. on pp. 2, 30, 32, 44, 47, 73).

[79] A. Barsic, G. Grover and R. Piestun,
Three-dimensional super-resolution and localization of dense clusters of single molecules,
Scientific Reports **4** (2014) 5388, (cit. on pp. 2, 30, 32, 35, 43, 44, 73–75).

[80] Y. Shechtman, S. J. Sahl, A. S. Backer and W. E. Moerner,
Optimal Point Spread Function Design for 3D Imaging,
Physical Review Letters **113** (2014) 133902, (cit. on pp. 2, 35, 44, 47, 73).

[81] A. Jesacher, M. Ritsch-Marte and R. Piestun, *Three-dimensional information from two-dimensional scans: a scanning microscope with postacquisition refocusing capability*,
Optica **2** (2015) 210, (cit. on pp. 2, 35, 45).

[82] J. Mertz, *Strategies for volumetric imaging with a fluorescence microscope*,
Optica **6** (2019) 1261, (cit. on pp. 2, 32).

[83] Y. Zhou, M. Handley, G. Carles and A. R. Harvey,
Advances in 3D single particle localization microscopy, APL Photonics **4** (2019) 060901,
(cit. on pp. 2, 32, 34, 43, 47, 60, 75).

[84] F.-R. G. H. Winkelmann, *Optical plane selection in a dipole trap*,
PhD thesis: University of Bonn, 2021, (cit. on pp. 2, 3, 6, 9, 12–15, 27, 28, 34, 57).

[85] C. Robens et al.,
Low-Entropy States of Neutral Atoms in Polarization-Synthesized Optical Lattices,
Physical Review Letters **118** (2017) 065302, (cit. on pp. 3, 43).

[86] M. R. Lam et al., *Demonstration of quantum brachistochrones between distant states of an atom*,
Physical Review X **11** (2021) 011035, (cit. on p. 3).

[87] S. Brakhane et al., *Note: Ultra-low birefringence dodecagonal vacuum glass cell*,
Review of Scientific Instruments **86** (2015) 126108, (cit. on pp. 3, 4).

[88] S. Chu, L. Hollberg, J. E. Bjorkholm, A. Cable and A. Ashkin,
Three-dimensional viscous confinement and cooling of atoms by resonance radiation pressure,
Physical Review Letters **55** (1985) 48, (cit. on p. 4).

[89] P. D. Lett et al., *Optical molasses*, JOSA B **6** (1989) 2084, (cit. on p. 4).

[90] J. Dalibard and C. Cohen-Tannoudji,
Laser cooling below the Doppler limit by polarization gradients: simple theoretical models,
JOSA B **6** (1989) 2023, (cit. on pp. 4, 5, 27).

[91] M. T. DePue, C. McCormick, S. L. Winoto, S. Oliver and D. S. Weiss,
Unity Occupation of Sites in a 3D Optical Lattice, Physical Review Letters **82** (1999) 2262,
(cit. on p. 5).

[92] X. Baillard et al., *Interference-filter-stabilized external-cavity diode lasers*,
Optics Communications **266** (2006) 609, (cit. on p. 6).

[93] R. Reimann, *Cooling and Cooperative Coupling of Single Atoms in an Optical Cavity*,
PhD thesis: University of Bonn, 2014 (cit. on p. 6).

[94] I. Bloch, *Ultracold quantum gases in optical lattices*, Nature Physics **1** (2005) 23, (cit. on p. 8).

[95] R. Grimm, M. Weidemüller and Y. B. Ovchinnikov, “Optical Dipole Traps for Neutral Atoms”, *Advances In Atomic, Molecular, and Optical Physics*, ed. by B. Bederson and H. Walther, vol. 42, Academic Press, 2000 95, (cit. on pp. 8, 9, 13).

[96] C. Robens et al., *Fast, High-Precision Optical Polarization Synthesizer for Ultracold-Atom Experiments*, Physical Review Applied **9** (2018) 034016, (cit. on p. 9).

[97] D. Döring, *Ein Experiment zum zustandsabhängigen Transport einzelner Atome*, Diploma thesis: University of Bonn, 2007 (cit. on p. 10).

[98] D. A. Steck, *Alkali D Line Data*, 2010, (cit. on p. 13).

[99] D. Meschede, *Optics, Light, and Lasers: The Practical Approach to Modern Aspects of Photonics and Laser Physics*, 3rd ed., John Wiley & Sons, Ltd, 2017, ISBN: 978-3-527-68548-6, (cit. on pp. 14, 15, 77).

[100] P. Du, *Optical Intensity Control Based on Digital and Analog Systems*, Master thesis: University of Bonn, 2018 (cit. on pp. 15, 16).

[101] M. Werninghaus, *Controlling atom transport in a two-dimensional state-dependent optical lattice*, Master thesis: University of Bonn, 2017 (cit. on p. 15).

[102] A. Alberti, W. Alt, R. Werner and D. Meschede, *Decoherence models for discrete-time quantum walks and their application to neutral atom experiments*, New Journal of Physics **16** (2014) 123052, (cit. on p. 15).

[103] E. A. Donley, T. P. Heavner, F. Levi, M. O. Tataw and S. R. Jefferts, *Double-pass acousto-optic modulator system*, Review of Scientific Instruments **76** (2005) 063112, (cit. on p. 15).

[104] J. Kobayashi, Y. Izumi, M. Kumakura and Y. Takahashi, *Stable all-optical formation of Bose–Einstein condensate using pointing-stabilized optical trapping beams*, Applied Physics B **83** (2006) 21, (cit. on p. 15).

[105] E. Ippen and R. Stolen, *Stimulated Brillouin scattering in optical fibers*, Applied Physics Letters **21** (1972) 539, (cit. on p. 17).

[106] K. Chandrashekara, *A High-Power Ti:Sa Laser System For Atomic Quantum Walk Experiments*, Master thesis: University of Bonn, 2020 (cit. on p. 17).

[107] R. E. Wagner and W. J. Tomlinson, *Coupling efficiency of optics in single-mode fiber components*, Applied Optics **21** (1982) 2671, (cit. on p. 19).

[108] D. Marcuse, *Gaussian approximation of the fundamental modes of graded-index fibers*, JOSA **68** (1978) 103, (cit. on p. 19).

[109] H. Kogelnik and T. Li, *Laser beams and resonators*, Proceedings of the IEEE **54** (1966) 1312, (cit. on pp. 19, 22, 35, 82).

[110] M. Hussain, T. Imran and Á. Börzsönyi, *Thermal lensing measurements of Ti: sapphire crystal by an optical wavefront sensor*, Microwave and Optical Technology Letters **61** (2019) 2901, (cit. on p. 19).

[111] T. Tari and P. Richter, *Correction of astigmatism and ellipticity of an astigmatic Gaussian laser beam by symmetrical lenses*, Optical and Quantum Electronics **24** (1992) S865, (cit. on p. 20).

[112] Y. Adachi and I. P. Adachi, "Diode laser having minimal beam diameter and optics", U.S. pat. 5321717A, A. I. P. Yoshifumi Adachi, 1994, (cit. on p. 20).

[113] M. Saruwatari and K. Nawata, *Semiconductor laser to single-mode fiber coupler*, Applied Optics **18** (1979) 1847, (cit. on p. 20).

[114] M. Omar, *Atom cloud compression in a 3D optical lattice and laser intensity stabilisation using an in-house developed photodiode amplifier*, Master thesis: University of Bonn, 2019 (cit. on p. 27).

[115] S. P. Rath et al., *Equilibrium state of a trapped two-dimensional Bose gas*, Physical Review A **82** (2010) 013609, (cit. on p. 27).

[116] G. J. A. Edge et al., *Imaging and addressing of individual fermionic atoms in an optical lattice*, Physical Review A **92** (2015) 063406, (cit. on p. 27).

[117] E. Cocchi et al., *Equation of State of the Two-Dimensional Hubbard Model*, Physical Review Letters **116** (2016) 175301, (cit. on p. 27).

[118] J. L. Ville et al., *Loading and compression of a single two-dimensional Bose gas in an optical accordion*, Physical Review A **95** (2017) 013632, (cit. on p. 27).

[119] J. W. Goodman, *Introduction To Fourier Optics*, 2nd ed., New York: McGraw-Hill, 1996, (cit. on pp. 28, 30, 41, 44, 59, 77, 80, 82).

[120] E. Abbe, *Beiträge zur Theorie des Mikroskops und der mikroskopischen Wahrnehmung*, Archiv für mikroskopische Anatomie **9** (1873) e413, (cit. on p. 30).

[121] Rayleigh, *XXXI. Investigations in optics, with special reference to the spectroscope*, The London, Edinburgh, and Dublin Philosophical Magazine and Journal of Science **8** (1879) 261, (cit. on p. 30).

[122] M. A. Thompson, M. D. Lew and W. Moerner, *Extending Microscopic Resolution with Single-Molecule Imaging and Active Control*, Annual Review of Biophysics **41** (2012) 321, (cit. on pp. 30, 31, 74).

[123] H. Deschout et al., *Precisely and accurately localizing single emitters in fluorescence microscopy*, Nature Methods **11** (2014) 253, (cit. on pp. 30, 32, 74).

[124] I. M. Khater, I. R. Nabi and G. Hamarneh, *A Review of Super-Resolution Single-Molecule Localization Microscopy Cluster Analysis and Quantification Methods*, Patterns **1** (2020) 100038, (cit. on pp. 30, 74).

[125] M. McDonald, J. Trisnadi, K.-X. Yao and C. Chin, *Superresolution Microscopy of Cold Atoms in an Optical Lattice*, Physical Review X **9** (2019) 021001, (cit. on pp. 30, 74).

[126] J. Chao, E. S. Ward and R. J. Ober, *Fisher information theory for parameter estimation in single molecule microscopy: tutorial*, JOSA A **33** (2016) B36, (cit. on p. 30).

[127] S. Ram, E. Sally Ward and R. J. Ober, *A Stochastic Analysis of Performance Limits for Optical Microscopes*, Multidimensional Systems and Signal Processing **17** (2006) 27, (cit. on p. 30).

[128] R. J. Ober, S. Ram and E. S. Ward, *Localization Accuracy in Single-Molecule Microscopy*, Biophysical Journal **86** (2004) 1185, (cit. on p. 30).

[129] v. F. Zernike, *Beugungstheorie des schneidenver-fahrens und seiner verbesserten form, der phasenkontrastmethode*, Physica **1** (1934) 689, (cit. on pp. 31, 87).

[130] D. D. Lowenthal, *Maréchal Intensity Criteria Modified for Gaussian Beams*, Applied Optics **13** (1974) 2126, (cit. on p. 31).

[131] D. Bardell, *The Biologists' Forum: The invention of the microscope*, BIOS **75** (2004) 78, (cit. on p. 31).

[132] L. von Diezmann, Y. Shechtman and W. E. Moerner, *Three-Dimensional Localization of Single Molecules for Super-Resolution Imaging and Single-Particle Tracking*, Chemical Reviews **117** (2017) 7244, (cit. on pp. 32, 34, 35, 73).

[133] S. Ram, P. Prabhat, E. S. Ward and R. J. Ober, *Improved single particle localization accuracy with dual objective multifocal plane microscopy*, Optics Express **17** (2009) 6881, (cit. on p. 33).

[134] M. Mart´inez-Corral and B. Javidi, *Fundamentals of 3D imaging and displays: a tutorial on integral imaging, light-field, and plenoptic systems*, Advances in Optics and Photonics **10** (2018) 512, (cit. on p. 33).

[135] R. R. Sims et al., *Single molecule light field microscopy*, Optica **7** (2020) 1065, (cit. on pp. 34, 74).

[136] R. Piestun, Y. Y. Schechner and J. Shamir, *Propagation-invariant wave fields with finite energy*, JOSA A **17** (2000) 294, (cit. on pp. 35, 39, 41).

[137] S. R. P. Pavani and R. Piestun, *Three dimensional tracking of fluorescent microparticles using a photon-limited double-helix response system*, Optics Express **16** (2008) 22048, (cit. on pp. 35, 43, 60).

[138] S. R. P. Pavani, J. G. DeLuca and R. Piestun, *Polarization sensitive, three-dimensional, single-molecule imaging of cells with a double-helix system*, Optics Express **17** (2009) 19644, (cit. on p. 35).

[139] L. Allen, M. W. Beijersbergen, R. J. C. Spreeuw and J. P. Woerdman, *Orbital angular momentum of light and the transformation of Laguerre-Gaussian laser modes*, Physical Review A **45** (1992) 8185, (cit. on p. 36).

[140] H. He, M. E. J. Friese, N. R. Heckenberg and H. Rubinsztein-Dunlop, *Direct Observation of Transfer of Angular Momentum to Absorptive Particles from a Laser Beam with a Phase Singularity*, Physical Review Letters **75** (1995) 826, (cit. on p. 36).

[141] K. Y. Bliokh, M. A. Alonso, E. A. Ostrovskaya and A. Aiello, *Angular momenta and spin-orbit interaction of nonparaxial light in free space*, Physical Review A **82** (2010) 063825, (cit. on p. 36).

[142] A. Cerjan and C. Cerjan,
Orbital angular momentum of Laguerre–Gaussian beams beyond the paraxial approximation, JOSA A **28** (2011) 2253, (cit. on p. 36).

[143] E. Abbe Hon., *VII.—On the Estimation of Aperture in the Microscope.*,
Journal of the Royal Microscopical Society **1** (1881) 388, (cit. on p. 40).

[144] C. W. McCutchen, *Generalized Aperture and the Three-Dimensional Diffraction Image*,
JOSA **54** (1964) 240, (cit. on pp. 40, 86).

[145] B. M. Hanser, M. G. L. Gustafsson, D. A. Agard and J. W. Sedat,
Phase retrieval for high-numerical-aperture optical systems, Optics Letters **28** (2003) 801, (cit. on pp. 40, 86).

[146] M. W. Beijersbergen, R. P. C. Coerwinkel, M. Kristensen and J. P. Woerdman,
Helical-wavefront laser beams produced with a spiral phaseplate,
Optics Communications **112** (1994) 321, (cit. on p. 41).

[147] N. R. Heckenberg, R. McDuff, C. P. Smith and A. G. White,
Generation of optical phase singularities by computer-generated holograms,
Optics Letters **17** (1992) 221, (cit. on p. 41).

[148] A. S. Ostrovsky, C. Rickenstorff-Parrao and V. Arrizón,
Generation of the "perfect" optical vortex using a liquid-crystal spatial light modulator,
Optics Letters **38** (2013) 534, (cit. on p. 41).

[149] N. Matsumoto et al., *Generation of high-quality higher-order Laguerre-Gaussian beams using liquid-crystal-on-silicon spatial light modulators*, JOSA A **25** (2008) 1642, (cit. on pp. 41, 53).

[150] L. Yu et al.,
The Laguerre-Gaussian series representation of two-dimensional fractional Fourier transform,
Journal of Physics A: Mathematical and General **31** (1998) 9353, (cit. on p. 41).

[151] A. C. Livanos and N. George, *Diffraction of Laguerre Gaussian Beams by an Aperture**,
JOSA **62** (1972) 1119, (cit. on p. 41).

[152] X. Zhong, Y. Zhao, G. Ren, S. He and Z. Wu,
Influence of Finite Apertures on Orthogonality and Completeness of Laguerre-Gaussian Beams,
IEEE Access **6** (2018) 8742, (cit. on p. 41).

[153] S. M. Kay, *Fundamentals of Statistical Processing, Volume I: Estimation Theory*, 1st edition,
Englewood Cliffs, N.J: Prentice Hall, 1993, 608 pp., ISBN: 978-0-13-345711-7 (cit. on p. 42).

[154] G. Tricoles, *Computer generated holograms: an historical review*,
Applied Optics **26** (1987) 4351, (cit. on p. 44).

[155] C. A. Weidner, H. Yu, R. Kosloff and D. Z. Anderson,
Atom interferometry using a shaken optical lattice, Physical Review A **95** (2017) 043624, (cit. on p. 44).

[156] S. Prasad, *Rotating point spread function via pupil-phase engineering*,
Optics Letters **38** (2013) 585, (cit. on p. 45).

[157] C. Roider, A. Jesacher, S. Bernet and M. Ritsch-Marte, *Axial super-localisation using rotating point spread functions shaped by polarisation-dependent phase modulation*,
Optics Express **22** (2014) 4029, (cit. on pp. 45, 47, 75).

[158] A. S. Backer, M. P. Backlund, A. R. von Diezmann, S. J. Sahl and W. E. Moerner, *A bisected pupil for studying single-molecule orientational dynamics and its application to three-dimensional super-resolution microscopy*, Applied Physics Letters **104** (2014) 193701, (cit. on pp. 45, 47, 75).

[159] M. P. MacDonald et al., *Creation and Manipulation of Three-Dimensional Optically Trapped Structures*, Science **296** (2002) 1101, (cit. on p. 45).

[160] H. Sun et al., *Imaging three-dimensional single-atom arrays all at once*, Optics Express **29** (2021) 4082, (cit. on p. 45).

[161] M. Persson, *Advances in Holographic Optical Trapping*, PhD thesis: University of Gothenburg, 2013 (cit. on pp. 45, 46).

[162] Z. Zhang, Z. You and D. Chu, *Fundamentals of phase-only liquid crystal on silicon (LCOS) devices*, Light: Science & Applications **3** (2014) e213, (cit. on pp. 45, 46).

[163] Z. Zhang et al., *Diffraction based phase compensation method for phase-only liquid crystal on silicon devices in operation*, Applied Optics **51** (2012) 3837, (cit. on p. 46).

[164] Santec Corporation, *SLM-100 Datasheet*, 2017, (cit. on pp. 46, 47).

[165] A. Jesacher, *Applications of spatial light modulators for optical trapping and image processing*, PhD thesis: University of Innsbruck, 2007 (cit. on p. 47).

[166] M. Persson, D. Engström and M. Goksör, *Reducing the effect of pixel crosstalk in phase only spatial light modulators*, Optics Express **20** (2012) 22334, (cit. on p. 47).

[167] W. Zhou-Hanf, *Robust Holographic Generation of Arbitrary Light Patterns: Method and Implementation*, Master thesis: University of Bonn, 2018 (cit. on pp. 47, 50, 75).

[168] A. Knieps, *A Spatial Light Modulator for Steering Quantum Walks with Single-Site Precision*, Master thesis: University of Bonn, 2017 (cit. on p. 47).

[169] T. Legrand, *Vergleich der Holografie und der direkten Abbildung mit dem räumlichen Lichtmodulator*, Bachelor thesis: University of Bonn, 2019 (cit. on pp. 47, 75).

[170] Z. Wang et al., *Aberration correction method based on double-helix point spread function*, Journal of Biomedical Optics **24** (2019) 031005, (cit. on pp. 68, 74).

[171] G. Heinzel, A. Rüdiger and R. Schilling, *Spectrum and spectral density estimation by the Discrete Fourier transform (DFT), including a comprehensive list of window functions and some new at-top windows*, (2002), (cit. on p. 70).

[172] L. v. Diezmann, M. Y. Lee, M. D. Lew and W. E. Moerner, *Correcting field-dependent aberrations with nanoscale accuracy in three-dimensional single-molecule localization microscopy*, Optica **2** (2015) 985, (cit. on pp. 71, 74).

[173] M. F. Parsons et al., *Site-Resolved Imaging of Fermionic $^{6}\mathrm{Li}$ in an Optical Lattice*, Physical Review Letters **114** (2015) 213002, (cit. on p. 73).

[174] R. Yamamoto, J. Kobayashi, T. Kuno, K. Kato and Y. Takahashi, *An ytterbium quantum gas microscope with narrow-line laser cooling*, New Journal of Physics **18** (2016) 023016, (cit. on p. 73).

[175] R. Grella, *Fresnel propagation and diffraction and paraxial wave equation*, Journal of Optics **13** (1982) 367, (cit. on p. 79).

[176] V. N. Mahajan, *Optical Imaging and Aberrations, Part III: Wavefront Analysis*, vol. PM221, Spie, 2013, 448 pp., ISBN: 978-0-8194-9111-4, (cit. on pp. 87, 88).

[177] Y. H. Hsieh, Y. T. Yu, Y. H. Lai, M. X. Hsieh and Y. F. Chen, *Integral-based parallel algorithm for the fast generation of the Zernike polynomials*, Optics Express **28** (2020) 936, (cit. on p. 88).

List of Abbreviations

AOM Acusto-Optic Modulator. 6, 9, 11, 12, 14, 15, 25

AR Anti-Reflective. 15, 17, 18, 25, 47, 60, 75

CCD Charge-Coupled Device. 56

CMOS Complementary Metal-Oxide-Semiconductor. 21, 46

CRLB Cramér-Rao Lower Bound. 30, 42, 44, 73, 74

DFT Discrete Fourier Transform. 54, 61, 62, 70

DH-PSF Double-Helix Point Spread Function. 26, 27, 42, 43, 44, 53, 54, 55, 56, 57, 58, 59, 60, 61, 62, 63, 64, 66, 67, 68, 69, 70, 71, 72, 73, 74, 75

DOF Depth of Field. 2, 7, 8, 26, 30, 32, 34, 35, 43, 56, 60, 70, 71, 72, 73, 74

DQSIM Two-Dimensional Discrete Quantum Simulator. 1, 2, 3, 7, 8, 13, 26, 75

EMCCD Electron-Multiplying Charge-Coupled Device. 7, 49, 59, 60

EOM Electro-Optic Modulator. 14, 15, 16, 25

FFL Front Focal Length. 89

FOV Field of View. 7, 14, 25, 34, 45, 64, 65, 67, 69, 70, 71, 74, 75

FPGA Field Programmable Gate Array. 11

HDT Horizontal Dipole Trap. 9, 11, 12, 13, 14, 15, 16, 17, 25, 51, 75

LC Liquid Crystal. 45, 46, 47

LCoS Liquid Crystal on Silicon. 45, 46

LDT Laser Damage Threshold. 14, 15

LG Laguerre-Gauss. 2, 20, 35, 36, 37, 38, 39, 41, 42, 44, 45, 51, 53, 54, 56, 57, 58, 64, 71, 73, 82, 83, 84, 85

LUT Lookup Table. 47, 56

MOT Magneto-Optical Trap. 4, 5, 6, 7, 27, 33, 48, 50, 57

MSE Mean Squared Error. 56, 68

MTF Modulation Transfer Function. 29

NA Numerical Aperture. 7, 8, 26, 30, 31, 32, 35, 47, 48, 49, 50, 52, 53, 54, 55, 56, 58, 64, 73, 86

OTF Optical Transfer Function. 29, 86, 87

PAN Parallel-Aligned Nematic. 45, 46

PCF Photonic Crystal Fiber. 12, 13, 16, 17, 18, 25, 75

PGC Polarization Gradient Cooling. 5, 6, 7, 13, 14, 27, 48, 50, 57, 75

PSF Point Spread Function. 2, 26, 27, 28, 29, 30, 31, 32, 34, 35, 38, 39, 40, 41, 42, 43, 44, 45, 47, 48, 51, 53, 54, 55, 56, 57, 59, 60, 61, 62, 63, 64, 66, 67, 69, 70, 71, 72, 73, 74, 75, 82, 86, 87

PV Peak-To-Valley. 47

RMS Root Mean Square. 31, 47, 51, 68, 69

RMSE Root Mean Squared Error. 65, 66

ROI Region of Interest. 62, 63, 64, 65

SLM Spatial Light Modulator. 2, 6, 26, 34, 45, 46, 47, 48, 49, 50, 51, 52, 53, 54, 55, 56, 57, 58, 59, 62, 64, 71, 72, 73, 75, 89

SNR Signal-To-Noise Ratio. 33, 43, 53, 57, 60, 61, 64, 75

VDT Vertical Dipole Trap. 9, 14, 50, 51, 69, 75

Acknowledgements

At this point I would like to thank all those who supported and inspired me during the work on this master's thesis.

First of all, I would like to thank my supervisor Prof. Dieter Meschede for enabling and supervising my master thesis and for integrating me into the working group. He always provided a pleasant and motivating working atmosphere.

For the helpful suggestions and constructive criticism during the experimental work as well as its preparation and analysis I would like to thank Dr. Andrea Alberti. His enthusiasm for experimental accuracy and technological simplicity is contagious. I was also happy not to be the only vegan in the working group, so lunch choices became easier, and also enjoyed the conversations about society and politics.

The PSF engineering project was only made possible by the original idea of Dr. Carrie Weidner and Dr. Andrea Alberti. With Carrie, I have consistently had helpful discussions and irreplaceable support. She has contributed significantly to the fact that this master thesis could be created in this form. Despite the adverse circumstances due to the pandemic, she came from Bristol to Bonn to help in the lab for more than two weeks.

Special thanks go to Dr. Gautam Ramola and Dr. Richard Winkelmann, with whom I had the pleasure of working. Despite the fact that they were working one after the other on writing their thesis, they always gave me a helping hand and advice in the lab. Thanks to them, bit by bit, I became capable of operating and maintaining such a complex laboratory on my own. This is also due to their previous careful experimental work, which made the laboratory very stable.

I also had a fruitful exchange with Brian Bernard at the beginning, who was always fun to work with. I will remember him for his love for cats and his impressive DIY skills (he built a SLM himself). The later visit to our lab by Alessandro Marcomini and Tommaso Faorlin was also absolutely amazing. Not a second was boring, not only because there was always a lot to do, but also because of their enthusiasm and good humor. I have just two words for you: dio cane.

Especially in the last phase of my work, Eduardo Uruñuela helped me with tips and tricks for writing and analysis. I would like to thank him for that. I always enjoyed sharing the office with him.

I would also like to thank Prof. Hofferberth, who was happy to assess the work as a second examiner, and for his patience during the last weeks of the lab. To the members of his group, among others Lukas A., Lukas T., Nina, Hannes P., Hannes B., Thilina, Cedric, Peggy, Julia and Jan, I would like to express appreciation for their company and helpfulness.

I would also like to thank Mr. Brähler from the electronics workshop and Mr. Graf from the precision mechanics workshop, as well as their teams. The SLM and the knife-edge mirror could be mounted and adjusted excellently thanks to the professionally manufactured mounts. I also want to thank the cleaning staff, who were the only people you would find in the institute in the middle of the night (of measurements).

Furthermore, I would like to thank my fellow student and friend Sebastian, who supported me with much interest and valuable criticism given during rehearsal talks.

I would also like to thank Sebastian, my sister Maïwenn, Dr. Hannes Busche, Dr. Carrie Weidner, Dr. Richard Winkelmann and Eduardo Uruñuela for proofreading parts of this thesis.

Not least because of having met Saima, this has been a wonderful time. I would like to thank you very much for your constant motivation and support. Especially during the phases when I was in the lab until late at night, your thoughtful support, food supplies, and sports and meditation sessions were vital.

Finally, I would like to thank my parents for encouraging my scientific and technical interest at an early age.